UCLouvain

École polytechnique de Louvain

# Defect Analysis of Additively Manufactured Scaffolds by 3D X-Ray Tomography

Author : Maria Andrea Alvarez Guerrero
Supervisors : Aude Simar, Grzegorz Pyka
Readers : Giovanni Garcea, Maciej Sobótka
Academic year 2023–2024
Master [120] in Mechanical Engineering

**ABSTRACT**

Metallic alloys with healing properties have garnered interest due to their potential to shift the paradigm of damage prevention to damage management. Concurrently, lattice structures due to their lightweight properties have become popular in various applications. This study aims to explore and characterize the behavior of lattice structures produced with these advanced materials.

Body-Centered Cubic (BCC) lattice structures were manufactured using Laser Powder Bed Fusion (LPBF) and characterized through images obtained via 3D X-ray tomography. Additionally, compression tests were conducted to evaluate the mechanical properties of the manufactured lattices.

The investigation focused on identifying the critical processing parameters necessary for producing lattice structures with high geometric accuracy and part density. Digital Volume Correlation (DVC) analysis was employed to detect critical defects within the structures that lead to failure. Furthermore, the healing properties of the material used in the lattice structures were examined.

The study revealed that lattice structures are highly sensitivity to processing parameters, requiring a careful balance. Optimal results for lattice structures with a 300µm beam diameter were achieved using a linear energy density (LED) of 0.409 J/mm, combined with pre-sintering and a contour-only scan path. Compressions tests highlighted the limitations of the Gibson-Ashby model in predicting the behavior of additively manufactured lattice structures; however, modifying the scaling pre-factors improved predictions for both elastic modulus and yield strength. Moreover, DVC analysis revealed that defects near nodes caused stress concentrations and localized strain, leading to buckling and structural failure. Finally, the diffusion healing mechanism was proved successful for a lattice structure with a final magnesium composition of 12.1% wt., using a healing heat treatment (HHT) at 400°C for 30 min followed by air cooling. However, further investigation is required to validate the liquid-assisted healing mechanism of the material.

**ACKNOWLEDGEMENTS**

Firstly, I would like to thank Aude Simar for her supervision, feedback, help throughout the project, and for trusting me with it. I am also grateful to my supervisor, Grzegorz Pyka, for his daily support and guidance, without which this work would not have been possible. Thank you for all the training, endless advice, and feedback that greatly helped me throughout the research; I have learned a lot from you.

Special thanks to Sophie De Raedemacker, without whom none of the heat treatments would have been possible. Thank you for all the training, your help with 3D printing, polishing, and for your constant availability and feedback, which helped build the presented work.

I also extend my gratitude to the entire IMAP team, who were available for any needed help or question. Thank you to Bruno Dell'Aquila and Jonathan Lorfevre for their help with argon encapsulations, to Ronny Santoro for his assistance with the ICP analysis, to Armand Béché for his constant advice and help with the X-ray machine and SEM, and to Mohammed Farag for his help with the CAD and printing files.

Thank you to Giovanni Garcea and Maciej Sobótka for agreeing to be readers of my thesis.

Finally, a big thank you to all the amazing people I am proud to call my friends, who have become my emotional support, but most important my home away from home. Thank you for the constant feedback and words of encouragement. Thank you to my family, whose support and trust have been felt even from all the way across the world. Special thanks to my mom for continuously listening to me talk about things she may not understand but tries to, and for always believing in me.

The use of Artificial intelligence (AI) tools to improve and correct grammar and sentence structure throughout the document is acknowledged.

## TABLE OF CONTENTS

i. LIST OF FIGURES ..... 8
ii. LIST OF TABLES ..... 14
1. INTRODUCTION. ..... 16
2. STATE OF THE ART ..... 17
*2.1. HEALABLE ALLOYS* ..... 17
*2.1.1. Macroscopic Healing Mechanisms* ..... 19
*2.1.2. Nano/Microscopic Healing Mechanisms* ..... 22
*2.2. ADDITIVE MANUFACTURING* ..... 26
*2.2.1. Additive Manufacturing Process* ..... 26
*2.2.2. Laser Powder Bed Fusion – LPBF* ..... 27
*2.2.3. Metal Powder* ..... 28
*2.2.4. LPBF – Defects* ..... 29
*2.2.5. Mechanical Properties - LPBF* ..... 33
*2.2.6. Process Parameters – LPBF* ..... 35
*2.3. LATTICE STRUCTURES* ..... 38
*2.4. X- RAY COMPUTED TOMOGRAPHY* ..... 43
*2.4.1. X- Ray Tomography Principle* ..... 43
*2.4.2. X- Ray Source* ..... 46
*2.4.3. X- Ray Detector* ..... 48
*2.4.4. Data Processing* ..... 49
*2.4.5. Visualization* ..... 49
*2.4.6. Errors* ..... 50
2.5. *DIGITAL VOLUME CORRELATION - DVC* ..... 52
*2.5.1. Main Principle* ..... 53
*2.5.2. Application* ..... 55
3. PROBLEM STATEMENT. ..... 56
4. MATERIALS AND METHODS. ..... 57
*4.1. RAW MATERIAL – AlMg14Zr1* ..... 57
*4.1.1. MORPHOLOGY – AlMg14Zr1* ..... 57
*4.2. LATTICE STRUCTURE* ..... 58
*4.2.1. Lattice Structure Stress and Deformations* ..... 60

*4.3. LPBF PARAMETERS* ..... 63
*4.4. MICRO CT (XCT) MORPHOLOGY CHARACTERIZATION* ..... 66
*4.5. COMPRESSIVE TESTING* ..... 68
*4.6. HEALING HEAT TREATMENT (HHT)* ..... 69
5. RESULTS ..... 70
*5.1. PRELIMINARY LPBF PROCESS* ..... 70
*5.2. MORPHOLOGY CHARACTERIZATION* ..... 79
*5.3. COMPRESSION TESTS* ..... 92
*5.4. DVC ANALYSIS* ..... 96
*5.5. HEALING HEAT TREATMENT (HHT)* ..... 105
6. DISCUSSION ..... 114
*6.1. IMPACT OF PROCESSING PARAMETERS IN LATTICE STRUCTURES* ..... 114
*6.2. LATTICE STRUCTURE THEORETICAL MODEL* ..... 117
*6.3. COMPRESSION TEST PERFORMANCE* ..... 121
*6.4. HEALING PROPERTIES WITH LATTICE STRUCTURES* ..... 122
7. CONCLUSIONS. ..... 124
8. REFERENCES. ..... 126

## i. LIST OF FIGURES

Figure 2-1. Illustration of the macroscopic healing mechanisms for metals, discussed in this document. The three different systems and the specific mechanisms within them are shown above. Eutectic healing is one of the possible healing mechanisms for the aluminum alloy used in this research [2]. ..... 18
Figure 2-2. Illustration of the nano/micro healing mechanisms for metals, discussed in this the document. Self-diffusion is one of the possible healing mechanisms for the aluminum alloy used in this research [2]. ..... 23
Figure 2-3. Self-diffusion typical healing stages [2]. ..... 24
Figure 2-4. Schematic of LPBF process [22]. ..... 28
Figure 2-5. Common morphology of keyhole porosity (left) and lack of fusion porosity (right). The images are taken from [30] research and they are from AM IN713C samples. ..... 31
Figure 2-6. Images of 316L stainless steel LPBF parts that suffered cracking [31]. ..... 33
Figure 2-7. Illustration of laser powder bed fusion (LPBF) processing parameters [29]. ..... 36
Figure 2-8. Expected microstructure in relation to the temperature gradient (G) and the solidification rate (R). LPBF is expected to have cellular dendritic or columnar dendritic microstructures due to its cooling and growth rate [29]. ..... 37
Figure 2-9. Cellular structures, (a) foam, (b) honeycomb and (c) lattice structure [36]. ..... 39
Figure 2-10. Lattice structures classified based on their topology [48]. ..... 42
Figure 2-11. (a) Basic principle of x-ray tomography, (b) Magnification adjustment achieved by movement of the measured object relative to the sensor and to the radiation source, (c) Type of tomography where images from various positions are stitched [50]. ..... 44
Figure 2-12. Illustration of x-ray tomography crucial parameters for voxel size and magnification calculation [51]. ..... 45
Figure 2-13. Illustration of x-ray spectrum and the superimposition of characteristic radiation and bremsstrahlung x-rays [52]. ..... 47
Figure 2-14. Ring artefacts (left) viewed in a CT image and the corrected version (right) [52]. ..... 50
Figure 2-15. Beam hardening defect (left) viewed in a CT image and the corrected version (right) [52]. . 51
Figure 2-16. DVC process and its steps: (a) defining a region of interest containing measurement locations; (b) measuring displacement at each location through correlation of reference and target digital volumes; and (c) calculating strain at each point by estimating the surrounding deformation gradients [58]. ..... 54
Figure 2-17. Comparison of displacement (top) and the strain (bottom) distributions from: (i) DVC calculation with 64 voxels sub-volume size; (ii) average FE results from continuum mapping; (iii) micro FE results [62]. ..... 55
Figure 4-1. Different types of unit cells with some characteristics, number of struts (s), number of joints (n), Maxwell number (M) and if the strut is aligned to the load direction [64]. ..... 58
Figure 4-2. Nomenclature and definition of parameters for controlling the BCC lattice structure in this research. ..... 59
Figure 4-3. Overall dimensions of the lattice structure specimens. The repetition of the unit cell in three dimensions forms a parallelepiped rectangle with dimensions: 5mm x 5mm x 10 mm. ..... 59
Figure 4-4. Typical stress (σ) – strain (ε) curve for cellular structures, illustrating the three distinct regions and corresponding parameters [64]. ..... 61

Figure 4-5. Laser scan patterns for: (a) Specimen A and (b) Specimen B, lattice structures designs. ..... 64
Figure 5-1. CT images of the lattice structure design for Specimen A, illustrating: (a) LPBF parameter 1,60%,400mm/s,PS, (b) LPBF parameter 2,60%,400mm/s,NS, (c) LPBF parameter 3, 70%,300mm/s,PS, and (d) LPBF parameter 4, 70%,300mm/s,NS. Specimen A is designed with an intended beam diameter of 100 $\mu$m. ..... 70
Figure 5-2. CT images of the lattice structure design for Specimen B, illustrating: (a) LPBF parameter 1,60%,400mm/s,PS, (b) LPBF parameter 2,60%,400mm/s,NS, (c) LPBF parameter 3, 70%,300mm/s,PS, and (d) LPBF parameter 4, 70%,300mm/s,NS.. Specimen B is designed with and intended beam diameter of 500 $\mu$m. ..... 71
Figure 5-3. CT image processing using Avizo software. The displayed images demonstrate the segmentation procedure within the software, enabling differentiation of the lattice structure from surrounding air and internal porosities within the structure. Lattice structures are depicted in light blue, internal porosities in dark blue, and surrounding air in red. Specimen A is shown on the left, and Specimen B is shown on the right. ..... 73
Figure 5-4. The graph illustrates the internal porosity percentage for each set of LPBF processing parameters. Both specimens are considered for each parameter set. Mean values for each set are indicated with a circle. “PS” refers to Pre-sintering, and “NS” refers to No Pre-sintering. For further details on Specimen A and B, refer to Table 4-2. ..... 73
Figure 5-5. The graph depicts the relative density percentage for each set of LPBF processing parameters, considering both specimens A and B. Theoretical values for relative density, calculated using the CAD model, are indicated with a circle. For further details on Specimen A and B, refer to Table 4-2. ..... 74
Figure 5-6. The image demonstrates the methodology employed by the software to fit spheres within the structure, thereby estimating its actual beam diameter. Specimen A is depicted on the left, and Specimen B is shown on the right. ..... 75
Figure 5-7. The graph illustrates the achieved beam diameter against the intended value for the four different LPBF parameter sets. Both specimens are shown on the graph. The theoretical beam diameter values are represented with a circle. ..... 76
Figure 5-8. The above distributions, derived from the CTAn software, represent the measured beam diameters the lattice structure design of Specimen A. For further details on Specimen A refer to Table 4-2. ..... 77
Figure 5-9. The above distributions, derived from the CTAn software, represent the measured beam diameters the lattice structure design of Specimen B. For further details on Specimen B refer to Table 4-2. ..... 78
Figure 5-10. CT images of the lattice structure design for Specimen 1: (a) xy plane, (b) xz plane, (c) yz plane. Specimen 1 has an intended beam diameter of 150 µm and was manufactured with 60% laser power, 400 mm/s and PS. For additional details on Specimen 1, refer to Table 4-2 ,and for LPBF parameters, refer to Table 4-4. ..... 79
Figure 5-11. CT images of the lattice structure design for Specimen 2: (a) xy plane, (b) xz plane, (c) yz plane. Specimen 2 has an intended beam diameter of 100 µm and was manufactured with 60% laser power, 400 mm/s and NS. For additional details on Specimen 2, refer to Table 4-2 ,and for LPBF parameters, refer to Table 4-4. ..... 80

Figure 5-12. CT images of the lattice structure design for Specimen 2 in the zone of the observed damage: (a) xy plane, (b) xz plane, (c) yz plane, (d) damaged sub volume. Specimen 2 has an intended beam diameter of 100 µm. For additional details on Specimen 2, refer to Table 4-2 ,and for LPBF parameters, refer to Table 4-4. ..... 81
Figure 5-13. Volume rendering of the damaged sub volume of Specimen 2, sample 2. The visible view is from the yz plane. For additional details on Specimen 2, refer to Table 4-2 ,and for LPBF parameters, refer to Table 4-4. ..... 82
Figure 5-14. Box plot illustrating the measured internal porosities for the two different lattice structure designs (Specimen 1 and 2) with their respective processing parameters. For additional details on the lattice structure designs, refer to Table 4-2, and for LPBF processing parameters, refer to Table 4-4. .... 83
Figure 5-15. Histograms depicting the measured equivalent diameter of internal porosities for two distinct lattice structure designs: Specimen 1 (top) and Specimen 2 (bottom). Additional details on lattice structure designs can be found in Table 4-2. ..... 85
Figure 5-16. Histograms depicting the measured sphericity of internal porosities for two distinct lattice structure designs: Specimen 1 (left) and Specimen 2 (right). Additional details on lattice structure designs can be found in Table 4-2. ..... 87
Figure 5-17. Visual estimation of sphericity in the vertical axis (Y) and roundness on the horizontal axis (X). Image taken from Kamel et. al. research paper [68]. ..... 88
Figure 5-18. Box plot illustrating the measured relative density for the two different lattice structure designs (Specimen 1 and 2) with their respective processing parameters. For additional details on the lattice structure designs, refer to Table 4-2, and for LPBF processing parameters, refer to Table 4-4. .... 88
Figure 5-19. Box plot illustrating the measured real beam diameter for the two different lattice structure designs (Specimen 1 and 2) with their respective processing parameters. For additional details on the lattice structure designs, refer to Table 4-2, and for LPBF processing parameters, refer to Table 4-4. .... 89
Figure 5-21. Structure separation of Specimen 1 (left) and Specimen 2 (right). ..... 90
Figure 5-22. Box plot illustrating the measured structure separation for the two different lattice structure designs (Specimen 1 and 2) with their respective processing parameters. ..... 91
Figure 5-23. Specimen 1(left) and Specimen 2(right) positioned inside the in-situ testing chamber. The samples were placed contrary to the building direction (BD) of the additive manufacturing process to utilize the more stable surface. ..... 93
Figure 5-24. Stress-strain curve for Specimen 1 compression test results. Specimen 1 has a designed beam diameter of 150 µm but a real value of approximately 450 µm. The parts were manufactured using 60% laser power, with 400mm/s laser scan speed and a pre-sintering step. For compression test parameters, consult Section 4.5. ..... 93
Figure 5-25. Stress-strain curve depicting the compression test results for Specimen 2. Specimen 2 has a designed beam diameter of 100µm but a real value of approximately 295µm. The part was manufactured using 60% laser power, with 400mm/s laser scan speed and no pre-sintering step. For compression test parameters, consult Section 4.5. ..... 94
Figure 5-26. Stress-strain curve depicting the compression test results for Specimen 1, intended for DVC analysis. Stress is calculated using the cross-sectional area of the solid parallelepiped rectangle. Specimen 1 has a designed beam diameter of 150 µm but a real value of approximately 450 µm. The parts were

manufactured using 60% laser power, with 400mm/s laser scan speed and a pre-sintering step. For compression test parameters consult Section 4.5. ..... 96
Figure 5-27. Radial autocorrelation used to determine the optimal mesh size for the DVC analysis of the CT images. ..... 98
Figure 5-28. Coarse mesh (red grid) employed for the local approach in DVC analysis of the CT images for Specimen 1. ..... 99
Figure 5-29. Displacement vector field for Specimen 1, illustrating compression steps from 0.3 to 0.4mm (left), 0.4mm to 0.5mm (middle), and 0.5mm to 0.6mm (right). All views are from the yz plane. ..... 99
Figure 5-30. Von mises strain map for compression step: 0.0-0.1 (Top left), 0.1-0.2 (Top right), 0.2-0.3 (Bottom left), and 0.3-0.4 (Bottom right). All views are from the yz plane. ..... 100
Figure 5-31. Von mises strain map for compression step: 0.4-0.5 (Top left), 0.5-0.6 (Top right), 0.6-0.7 (Bottom left), and 0.7-0.8 (Bottom right). All views are from the yz plane. ..... 101
Figure 5-32. Von mises strain map for compression step: 0.8-0.9 (Left), and 0.9-1.0 (Right). Both views are from the yz plane. ..... 102
Figure 5-33. Von mises strain map for compression step 0.4-0.5mm. The left displays the sectional view of the structure from the xz plane, while the right presents the cut structure from the yz plane. ..... 103
Figure 5-34. Von mises strain map for compression step 0.5-0.4mm. The left displays the sectional view of the structure from the xz plane, while the right presents the cut structure from the yz plane. ..... 104
Figure 5-35. Von mises strain map for compression step 0.6-0.7mm. The left displays the sectional view of the structure from the xz plane, while the right presents the cut structure from the yz plane. ..... 104
Figure 5-36. CT images of a lattice structure design with processing parameters set 1. This particular lattice structure design is not included within the designs described in Section 4.2, but it was useful for evaluating the HHT of the material with this type of geometry. The intended beam diameter of the shown part is 200 µm, featuring a reinforced BBC structure. The image on the left shows the structure before HHT, and the image on the right shows it after HHT at 540°C for 30 minutes with water quenching. For details on the LPBF parameters, refer to Table 4-3. ..... 105
Figure 5-37. CT images of a lattice structure design with processing parameters set 1. This particular lattice structure design is not included within the designs described in Section 4.2, but it was useful for evaluating the HHT of the material with this type of geometry. The intended beam diameter of the shown part is 300 µm, featuring a reinforced BBC structure. The image on the left shows the structure before HHT, and the image on the right shows it after HHT at 540°C for 30 minutes with air cooling. For details on the LPBF parameters, refer to Table 4-3. ..... 106
Figure 5-38. CT images of a lattice structure design Specimen A with processing parameters set 1. The image on the left shows the structure before HHT, and the image on the right shows it after HHT at 400°C for 30 minutes with air cooling. Specimen A has an intended beam thickness diameter of $100\ \mu m$. For more details on Specimen A design, refer to Table 4-2, and for details on the LPBF parameters, refer to Table 4-3. ..... 107
Figure 5-39. Histogram of the equivalent porosity diameters for Specimen A lattice structure, processed with parameters 1, before HHT and after an HHT at 400°C for 30 minutes with air cooling (AC). For further details on Specimen A, refer to Table 4-2, and for LPBF parameters, refer to Table 4-3. ..... 108
Figure 5-40. Al-Mg phase diagram. The eutectic phase melting temperature is 450°C. [69]. ..... 111

Figure 5-41. Histograms of the porosities equivalent diameter for lattice structure design Specimen 1 samples, before and after HHT at 450°C for 30 min with air cooling (AC). Refer to Table 4-2 for more specimen 1 details and to Table 4-3 for LPBF parameters details. The measurements were performed with CT images acquired with a 4 µm voxel size. ..... 111
Figure 5-42. Histogram of the porosities equivalent diameter for lattice structure design Specimen 2, before and after HHT at 450°C for 30 min with air cooling (AC). Refer to Table 4-2 for more Specimen 2 details and to Table 4-3 for LPBF parameters details. The measurements were performed with CT images acquired with a 4 µm voxel size. ..... 112
Figure 5-43. Box plot of the measured internal porosities for the two different lattice structure designs, Specimen 1 – PS-60%-400mm/s, and Specimen 2-NS-60%-400mm/s. Before HHT on the left (Figure 5-14) and after HHT at 450°C for 30 min with air cooling (AC), on the right. Refer to Table 4-2 for more lattice structure designs details. The measurements were performed with CT images acquired with a 4 µm voxel size. ..... 112
Figure 5-44. CT images of lattice structure design Specimen 1, sample 3. On the left the structure before HHT and on the right after an HHT at 450°C for 30 min with air cooling. Specimen 1 has an intended beam thickness diameter of $150\ \mu m$. Refer to Table 4-2 for more specimen A details and to Table 4-3 for LPBF parameters details. ..... 113
Figure 5-45. CT images of lattice structure design Specimen 2, sample 1. On the left the structure before HHT and on the right after an HHT at 450°C for 30 min with air cooling. Specimen 2 has an intended beam thickness diameter of $100\mu m$. Refer to Table 4-2 for more specimen A details and to Table 4-3 for LPBF parameters details. ..... 113
Figure 6-1. Laser scan patterns for: Specimen 1 (left) and Specimen 2 (right), lattice structures designs. ..... 116
Figure 6-2. Analytical predictions of the elastic modulus of the lattice structure with the Gibson-Ashby model and the experimental results from the compression test performed. The adjusted Gibson-Ashby model has a $C1$ value of 0.3. ..... 119
Figure 6-3. Analytical predictions of the yield strength of the lattice structure with the Gibson-Ashby model and the experimental results from the compression test performed. The adjusted Gibson-Ashby uses Equation (11). ..... 120

## ii. LIST OF TABLES

Table 2-1. Mechanical properties of aluminum alloys with regards to their processing parameters. Comparison between PBF and traditionally processed parts [22]. ..... 34
Table 4-1. Inductively Coupled Plasma (ICP) spectroscopy and three-acid attack were employed to characterize the pre-mixed powder used throughout this research. The mean between the two methods will be used as the true value of the composition. Note that the value for each technique is the mean of two separate samples of the powder. ..... 57
Table 4-2. The table details the dimensions of the manufactured lattice structures. Specimens labeled with letters correspond to preliminary specimens produced to assess the capabilities of the machine and powder. Specimens labeled with numbers correspond to the final dimensions of the manufactured specimens intended for further testing. ..... 60
Table 4-3. The table outlines the LPBF process parameters related to the specified lattice structure design detailed in Table 4-2. The parameters listed here are specific to the preliminary LPBF process conducted to evaluate the machine's performance. For definitions of the parameters described in this table, refer to Figure 2-7. ..... 64
Table 4-4. This table details the LPBF process parameters for the lattice structure designs detailed in Table 4-2. These parameters are specifically for the Specimens 1 and 2. For definitions of the parameters described in this table, refer to Figure 2-7. ..... 65
Table 5-1. Three-acid attack (HF, HCL, HNO3) and fusion characterization of the composition of selected manufactured lattice structures. Since the parts used for this analysis are destroyed during testing, the structures differ from those described in Section 4.2. Lattice structures with beam diameters of 100 and 400µm were used, featuring BBC and double BBC structures configurations respectively, were analyzed. Some structures were tested post-HHT, with specific processing parameters detailed below the table. ..... 109
Table 6-1. Summary of the processing parameters used for the preliminary printing of the lattice structures. The VED parameter is calculated with equation (9). ..... 115
Table 6-2. Summary of the mean values of the structure's geometry (Section 5.2) and calculated relative densities. The analytical relative density is calculated based on equation (10) and the adjusted values consider the internal porosity of the beam. ..... 118

# 1. INTRODUCTION.

Engineers play a vital role in designing the mechanisms and components that constitute our daily lives, from the coffee machine in our kitchens, to the automobiles that transports us to work. Traditionally, the focus for engineered materials has been on enhancing material strength to prevent any damage and degradation from its intended lifespan, adopting a damage prevention paradigm. However, a new approach, known as damage management, has been gaining traction. This approach focuses on developing materials with self-healing capabilities, based on the premise that damage, if correctable, may not necessarily be detrimental [1].

This paradigm shift offers an intriguing opportunity to optimize materials properties. Despite efforts to maximize material strength, issues such as crack initiation, micro-cracks and micro defects persist, often beyond the control of current manufacturing methods. These imperfections not only degrade the material lifespan but also need conservative design approaches to ensure safety [2].

By embracing the new approach, these variables can be mitigated or minimized through techniques like healing heat treatment (HHT), which will be discussed further in Section 2.1. This new approach holds significant promise across all engineering sectors, particularly in safety-critical applications such as aerospace and automotive industries. Although healable alloy technology is still in development, the ongoing research is promising.

This document provides an in-depth exploration of the research conducted to characterize a specific healable alloy, currently under development, and its application in additive manufactured lattice structures. It covers theoretical foundations of the alloy, the additive manufacturing process, lattice structures, testing methodologies, and analytical approaches employed throughout the research.

# 2. STATE OF THE ART.

## *2.1. HEALABLE ALLOYS*

Healable engineered materials have been studied in recent years. Healing mechanisms have been researched and proven inside polymer composites with the capacity to autonomously heal cracks from microcapsules of healing agent [1]. The design of healable materials is based on nature and on the concept that damage is not inherently bad as long as it can be corrected by a healing process that removes the damage [2]. Healable materials allow a shift in the development of materials that will change the current material developing strategy, from having to strengthen and tailor the material to its application in order to prevent the damage, to a strategy of developing materials that can not only withstand the loads inherent to the application but also heal the damage caused by them. In other words, the intent is to switch from the damage prevention paradigm to the damage management paradigm [2], [3].

Creating self-healing metallic systems presents greater challenges compared to the already studied polymers, primarily due to the limited mobility of metallic atoms at ambient temperatures. Additionally, the diminutive size of these atoms, coupled with their tendency to move in opposition to vacancies, further complicates the development of healable metals [1], [2], [4]. Nevertheless, the principle guiding all healing methodologies remains consistent; the creation of a mobile phase to seal fractures, prompted either by the damage or external stimuli [2], [5]. In engineered materials, particularly metals, self-healing typically relies on such external triggers. Consequently, two distinct categories of healing mechanisms emerge [6]:

- Autonomous: Healing occurs independently, without external interference.
- Non-autonomous: Healing needs external intervention, such as thermal, electrical, magnetic, or other stimuli.

The different healing mechanisms of both categories are commonly divided into two different strategies depending on the size of the damage to heal: macro scale and nano/micro scale [2]. The focus throughout this section will be aimed toward the description of the different healing strategies within these divisions, emphasizing on the healing strategies pertinent for the material that will be used for this research.

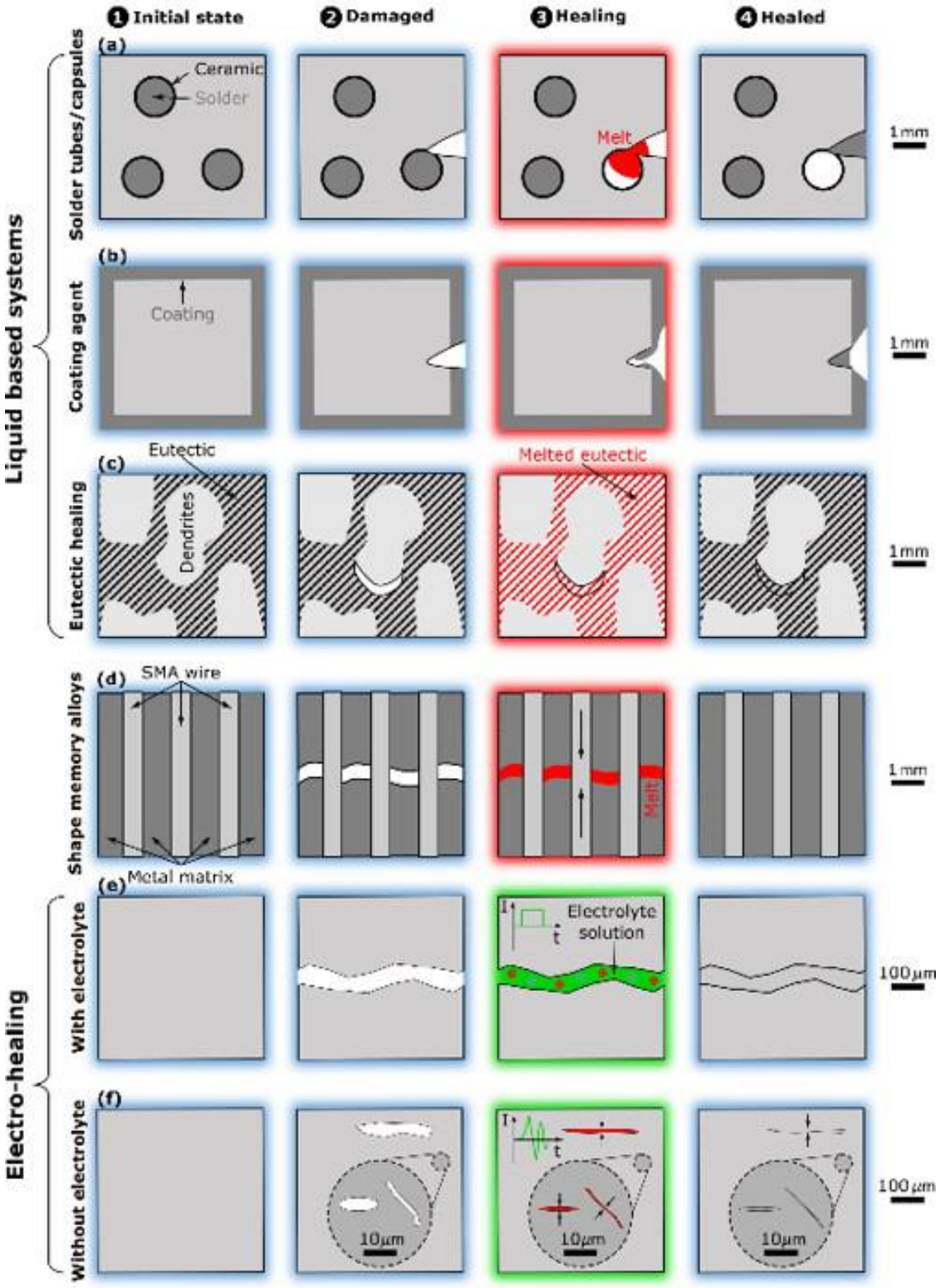


*Figure 2-1. Illustration of the macroscopic healing mechanisms for metals, discussed in this document. The three different systems and the specific mechanisms within them are shown above. Eutectic healing is one of the possible healing mechanisms for the aluminum alloy used in this research [2].*

### 2.1.1. ***Macroscopic Healing Mechanisms***

An overview of the mechanisms to be discussed within this section can be found in Figure 2-1.There are two primary systems in existence within the macroscopic healing mechanisms. One relies on the generation of a liquid metal flow directed towards macroscopic damages (Liquid-Based Systems), while the other, known as electro-healing, employs electricity rather than heat to induce atomic motion [2]. In addition to those two mechanisms, there is a third system, which consist of composite materials integrated with shape memory alloy (SMA) wires within a metallic matrix. The efficacy of this system hinges on the capacity of the SMA to revert to its original, undeformed state through a healing heat treatment (HHT) conducted above the phase transformation temperature subsequent to deformation [2] [4]. The SMA healing approach represents a variation of the eutectic-based strategy and is outside the scope of this investigation. The advantage of the macroscopic healing mechanisms is their ability of healing larger voids than the nano/micro mechanisms.

#### *2.1.1.1. Liquid Based Systems*

Typically, the liquid-based systems refer to three liquid-assisted healing systems (Figure 2-1). Although they are distinct they share a foundation among them, the utilization of a liquid healing agent (HA) to seal cracks. Upon damage, a HHT is necessary to liquefy the HA without melting the entire metallic system. Subsequently, the liquefied HA can penetrate the crack and fill it. Upon cooling, the HA solidifies within the crack, concluding its repair. The distinguishing factor among these three liquid-assisted strategies is the type of HA employed and the method by which it reaches the site of damage [2], [4].

- Solder Tubes/Capsules

The method entails encasing a low-temperature melting alloy within ceramic tubes or capsules, depending on the specific design. These containers are dispersed within a matrix with a higher melting temperature. When a crack forms within the material, the ceramic container will ideally fracture. Subsequently, a HHT is conducted at a temperature conducive to melting the low-temperature solder alloy while maintaining the matrix in a solid state. The molten solder then flows into the crack driven by capillary pressure and surface tension, ultimately sealing it upon solidification [2], [7], [8].

This healing approach faces two primary challenges. First, ensuring sufficient bonding between the solder and the matrix post-healing is essential for complete crack closure [2], [7]. Inadequate bonding or excessive porosity may result in partial healing, allowing the crack to persist. Second, the strategy relies entirely on the fracture of the HA containers. If the crack fails to rupture the tube or microcapsule, the HA cannot be released for flow [2], [4]. Should the crack propagate along the tube/matrix interface, the solder remains trapped within the tube, hindering crack filling during HHT and impeding healing.

- Coating Healing Agent

This healing strategy involves the application of a coating agent but the operational principle mirrors that of the preceding strategy, with the exception that the HA is instead applied as a coating onto the material. Upon damage, a HHT initiates the melting of the coating while maintaining the material's solid state, facilitating its flow into and filling of the crack. An advantage of this approach is that it preserves the composition and microstructure of the base material [2], [9]. However, it has some limitations like: the need for the HHT to be conducted in a protective atmosphere to prevent oxidation and the fact that only non-oxidized damaged surfaces are prone to healing with this mechanism, which is not a common occurrence. Consequently, this strategy has received limited investigation.

- Eutectic Based Healing

In this mechanism, the alloy's microstructure comprises two phases: a dendritic phase with a high melting point and a eutectic phase with a low melting point [2], [10]. It is the eutectic phase that serves as the HA. Following damage, a HHT within the liquid-solid region initiates the melting of the eutectic phase, while the dendritic phase maintains the structural integrity of the component. This enables the eutectic phase to flow to the damaged sites and seal them upon solidification [2]. Eutectic based healing is one of the two strategies that can be applied to the material to be used within this research.

To create a eutectic-based healing system, a hypo or hyper eutectic alloy composition is needed. Hence during solidification, dendrites of a saturated phase initially form, while the composition of the remaining liquid adjusts towards the eutectic composition. Subsequently,

at lower temperatures, the remaining liquid solidifies into a eutectic phase between the dendrites [2], [10]. The primary advantage of this approach is that many different systems can potentially exhibit this healing mechanism, provided they are hyper- or hypo-eutectic alloys [2], [10]. Furthermore, the microstructure is relatively straightforward making its production possible via conventional manufacturing techniques (i.e. casting) [2].

Achieving an optimal ratio between dendritic and eutectic phases is crucial. Sufficient dendrites are necessary to maintain the part's structural integrity, yet enough eutectic phase must be present for the liquid to reach the healing site and fully fill the crack [2], [10].

Gheysen et al. investigated various aluminum alloys containing magnesium, focusing on their potential for liquid-assisted eutectic healing due to their low eutectic point. Their research demonstrated that additively manufactured using an AlMg14 alloy exhibit liquid-assisted healing properties. Conversely, parts manufactured with an AlMg28 alloy contain an excess of eutectic phase, that hinders liquid-assisted healing by causing structural loss [2].

#### *2.1.1.2. Electro-Healing Systems*

The electro-healing process represents a versatile strategy capable of addressing defects of various sizes. Its distinguishing feature is the use of an electrical field, rather than heat, as the driving force for the mobility of the HA [2], [4], [11]. Consequently, it does not modify the initial sample's microstructure. This strategy can be categorized into two approaches: one employing an electrolyte solution as the HA and the other utilizing electro-pulsing.

Electro-healing using an electrolyte solution was explored by Zheng et al. [12]. The experimental setup involved subjecting samples to a current within an electrolyte aqueous solution containing Ni ions for a duration ranging from 2 to 20 hours, depending on the sample thickness. During the electrical treatment, ions were reduced at the crack surface and bonded with the Ni sheet. However, the efficiency of the process diminishes with thicker samples [2], [12].

Electro-pulsing treatment is characterized by high-energy electric pulses typically lasting less than 1 ms [2]. It involves two steps:

1. Crack closure: The crack, acting as a barrier to electron flow, experiences a localized increase in resistance under electro-pulsing. This results in an uneven thermal gradient near the crack due to the Joule effect, inducing local compressive stress that brings the two crack surfaces into contact [2].
2. Crack healing: The local heating and stress near the crack tip cause material softening, leading to micro-welding of the crack, effectively sealing it [13].

The advantages of this healing strategy lie in its ability to operate without significant alteration of the material (no addition of SMA wires, coating, or low-melting-point phases) and its localized impact on the material at the damage site without the need for pre-detection [2], [13], [14].

### *2.1.2. Nano/Microscopic Healing Mechanisms*

The non-directionality of chemical bonds in metals and the minute size of its atoms result in healing of defects occurring only at the nano or micro scale, primarily through solid-state mechanisms involving the activation of metallic atom diffusion [5]. These strategies aim to halt the progression of nano/micro-scale defects to macro-scale damage by addressing them prior to their enlargement [2], [5].

Solid-state healing strategies rely on the presence and adequate mobility of HA to migrate towards damaged areas [4]. Thus, there is a need for an external driving force to facilitate this mass transfer [1], [11]. Depending on the external stimuli used to promote diffusion and consequently the diffusion mechanism, three categories of solid-state healing strategies can be defined: High Temperature Precipitation, Low Temperature Precipitation, and matrix self-diffusion healing [2] (Figure 2-2).

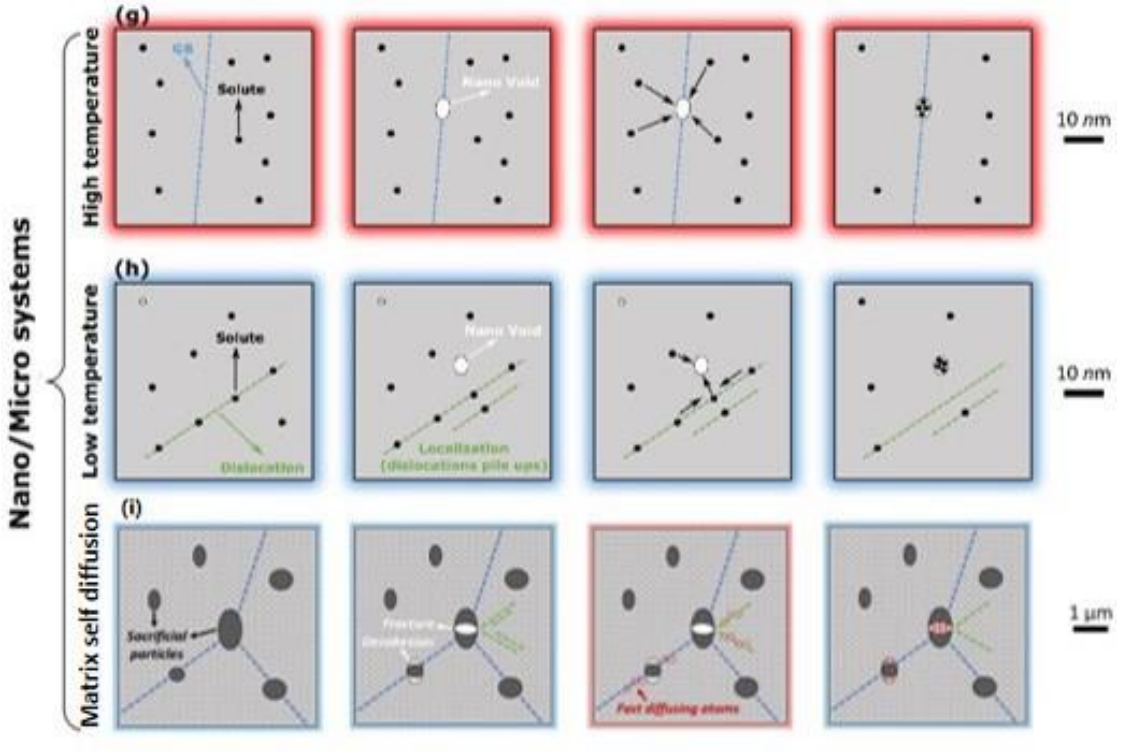


*Figure 2-2. Illustration of the nano/micro healing mechanisms for metals, discussed in this the document. Self-diffusion is one of the possible healing mechanisms for the aluminum alloy used in this research [2].*

#### *2.1.2.1. High Temperature Precipitation*

High temperature precipitation relies on precipitating the HA at damage sites under high temperatures [4]. Thermal activation is employed to facilitate the diffusion of the HA towards nanovoids. Given the need of sustained high temperatures throughout the material's service life, this healing strategy is primarily tailored for creep-resistant applications of steel [2].

#### *2.1.2.2. Low Temperature Precipitation*

Low temperature precipitation operational principle mirrors that of high temperature precipitation, wherein solute atoms diffuse towards nanovoids and precipitate on their surfaces, filling the damaged areas. This healing method also needs a supersaturated alloy. However, unlike high temperature precipitation, solute atoms primarily diffuse via pipe diffusion rather than grain boundaries, resulting in a lower healing temperature requirement. Notably, solute atoms segregate on dislocation cores and when the dislocations accumulate the created stress concentration initiates nanovoid formation. Subsequently, solute atoms diffuse towards these

nanovoids, precipitate, and fill them. Low temperature precipitation healing is employed to enhance fatigue life performance [2].

#### *2.1.2.3. Self-Diffusion*

Self-diffusion of the matrix unfolds in three stages. Initially, a rapid healing stage leads to blunting of the crack tips. Subsequently, the healing process deaccelerates, and the crack morphs into a channel of cylindrical voids that gradually diminish in size. Finally, rapid healing of the remaining small voids occurs (see Figure 2-3). The kinetics of healing are significantly influenced by several factors, including crack location and geometry, type of diffusion, and concentration of solute atoms in the matrix [2], [15], [16], [17], [18].

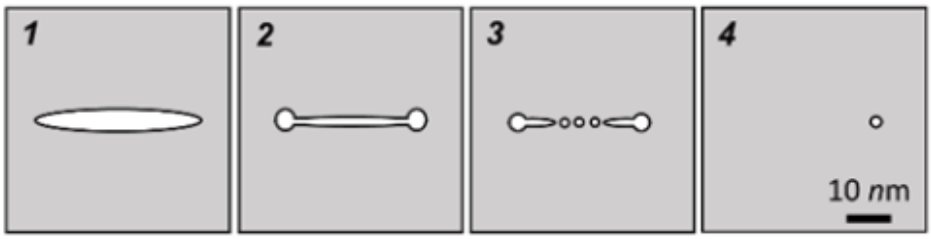


*Figure 2-3. Self-diffusion typical healing stages [2].*

Song et al. demonstrated the healing potential of an Al-Mg-Er alloy. Following cold rolling, the brittle AlMn6 precipitates fracture, generating numerous voids. After 50 minutes at 180°C, transmission electron microscopy (TEM) observations coupled with energy dispersive spectroscopy (EDS) analysis revealed successful void healing [2], [15].

However, healing by self-diffusion presents several critical limitations. A primary limitation is the requirement for relatively high temperatures for healing activation, which may induce phase transformations and render it impossible to fully heal micro-cracks within a reasonable timeframe [2], [19]. Another limitation of this strategy is the constraint on damage size, which needs to be below the micrometer scale, this is not always feasible. Consequently, an enhancement of this healing strategy involves incorporating sacrificial and healable reinforcement particles within the alloy matrix. The objective is for damage to primarily initiate on these sacrificial particles, thereby controlling the damage nucleation process and size. Subsequently, an HHT triggers the self-diffusion of the matrix towards these cavities. This particular strategy is also referred to as Programmed Damage and Repair [2], [20].

Given that self-diffusion is another healing mechanism possible for the material to be used throughout this research, it is important to enlist some key considerations for the development of solid-state healable aluminum alloys [2].

- Thermal activation to facilitate the diffusion of the mobile healing agent towards damage sites is necessary. The temperature should be sufficiently high to promote diffusion yet low enough to limit microstructural changes and reduction of mechanical properties [2].
- The microstructure should contain supersaturated solute atoms [2].
- Precipitation should occur only on damage sites to prevent trapping of healing solutes in stable secondary phases throughout the matrix [2].
- Damage should preferably occur near diffusion shortcuts rather than on the material surface to avoid oxidation and water vapor contamination, which could impede the healing process.

As previously mentioned, the alloy used in this research is an aluminum-magnesium alloy with the addition of zirconium (AlMg14Zr1). The inclusion of zirconium induces the precipitation of $Al_3Zr$ during the laser powder bed fusion (LPBF) process. These precipitates act as heterogeneous nucleation sites for the α-Al phase, leading to grain refinement and, consequently, improved mechanical properties of the material [2]. Additionally, the precipitates limit grain coarsening effect during heat treatments, which is beneficial for healing treatments [2]. Thus, the addition of zirconium addresses several key considerations discussed above.

### *2.2. ADDITIVE MANUFACTURING*

Previously referred to as 3D printing, additive manufacturing (AM) is a process that creates three dimensional objects by progressively adding material in thin layers following a digital model [21]. Given the nature of the process, AM offers flexibility with regards to materials to be used and to the geometry to be manufactured. This allows the building of parts with complex geometries that would not have been able to be built with conventional manufacturing methods. Among the other benefits of additive manufacturing lay the possibility of reducing or eliminating assembly steps to achieve the same component as well as the on-demand production of parts that consequently reduce the inventory and lead time for the manufactured components [22].

On its earlier stages, AM was mainly used for prototyping because the technology at the time only permitted the use of polymers as raw material. Currently, certain AM processes provide the possibility of utilizing metal alloys thanks to the rapid evolution of the technology. Nevertheless, AM parts present challenges of their own like the metallurgical differences with regards to conventionally manufactured ones i.e. anisotropy, residual stresses or defects uniquely present on AM processes. These challenges are serious specially in critical applications making it important to counteract with post-processing or avoid with product and process design [22].

#### *2.2.1. Additive Manufacturing Process*

The AM process transforms the raw material, as powder, wire or sheets into a dense metallic part by melting and solidifying it with the help of an energy source. Said energy source could be a laser, an electron beam or an electric arc, or ultrasonic vibration. The manufacturing of a structurally sound, defect free, reliable part requires the understanding of the available processes, from the material to be used to the process parameters to control and the defects to avoid [22].

As stated on the ASTM standard F2792 [23], the AM process can be classified in two categories: Direct Energy Deposition (DED) and Powder Bed Fusion (PBF). Further classification can be provided in function of the primary heat source used: Laser (L), electron beam (EB), plasma arc (PA) or gas metal arc (GMA) [22].

It is common that AM metal parts require some post-processing, nevertheless PBF, and in some instances DED processes, are considered direct-to-metal. Direct-to-metal refers to the ability to start with a computer model and directly produce a net shaped part [22].

Specifically, for the application of healable alloys Laser Powder Bed Fusion (previously known as Selective Laser Melting – SLM) is preferred given that due to the high cooling rates throughout the process a specific microstructure is achieved that helps create an interconnected network of material that will serve as healing agent during a healing heat treatment [2]. This phenomenon will be explained in greater detailed below.

### *2.2.2. Laser Powder Bed Fusion – LPBF*

Among the classification of AM processes PBF is one of the most commonly applied mainly due to its low-cost quality. In PBF heat is directly applied to the powder bed through the heat source. The powder bed continuously moves down to accommodate the next powder layer once the previous one has been completed. The fusion and melting of the powder in a PBF process can be made by two different heat sources: Laser or Electron Beam. Some advantages of this particular process are the minimum to none support required, the range of suitable materials, plastic, glass, and metal alloys and the recyclability of them [24].

Laser powder bed fusion is a category of metal additive manufacturing that uses a laser as a focalized heat source while a continuous flow of inert gas (typically argon) is applied to help with powder spatter and avoid oxygen interaction with powder particles [24], [25]. Powder bed additive manufacturing process consist of the following steps (refer to Figure 2-4):

1. The 3D model of the workpiece gets converted into an STL (stereo lithographic) file that cuts the model into layers (cross-section). Each cross section translates into each layer of the LPBF manufacturing process [24].
2. The STL file is uploaded to the printer software. This is when the printing parameters are selected. Note that multiple workpieces can be added to the bed of the printer, same or different, improving the productivity of the process [24].
3. The powder chamber gets filled with the desired alloy in powder form [24]. Powder properties are crucial to the LPBF process, they will determine how the powder flows and

packs throughout the process and consequently impact the development of melt pools and microscopic homogeneity [26].

4. A powder layer is spread above the bed of the printer and by means of the heat source and the STL file, the powder gets melted according to the desired shape [24].
5. Another layer of powder gets spread above the previous one. This step and the previous one repeat until the complete piece is finished [24].

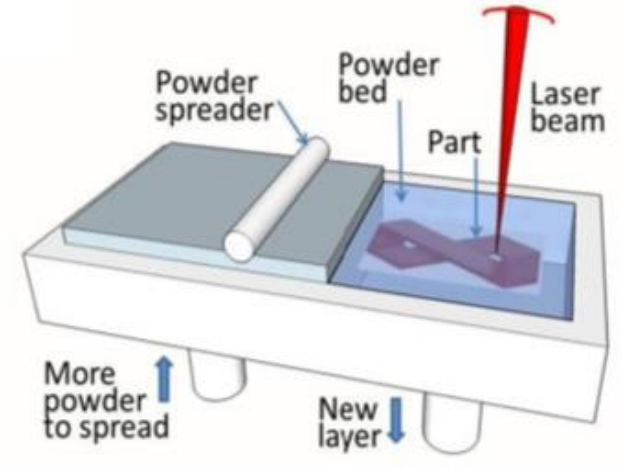


*Figure 2-4. Schematic of LPBF process [22].*

### 2.2.3. ***Metal Powder***

The impact that powder properties have on AM parts has been observed in various studies. Therefore, it is of particular interest to study and control these properties to assure the manufacturing of quality, reliable and repeatable parts [27].

The powder properties can be classified in three main categories: Morphology, Chemistry and Microstructure. Subsequently, morphology is divided into particle size, shape and surface roughness, chemistry is divided into bulk chemistry and surface chemistry, and Microstructure is divided into internal porosity and crystal structure. Even though powder chemistry and microstructure influence part quality, powder morphology is the property most studied for AM applications due to its strong correlation to manufactured component properties like mechanical strength, porosity and surface finish [27].

The selection of desired powder properties stems from the sought-after properties of the manufactured part. The particle size determines the minimum size of the part features and the

minimum layer thickness. It has been proven that increasing the layer thickness decreases the density and the surface quality of the manufactured part [28]. Therefore, it is recommended to utilize powders with particle sizes between 15µm to 150µm. The minimum particle size is constrained because of the tendency to agglomerate of fine powders which can lead to powder flow complications and consequently to balling and undesired porosity [27].

Other morphological factors to consider are particle shape and surface roughness of the powder. The effect of the shape has been studied previously and it was determined that the closer it resembles a sphere the less internal friction and consequently higher layer densities achieved, which produces a higher density manufactured part [27].

Powder chemistry is known to be important in regards to final mechanical properties of manufactured parts. The selection of the powder chemistry will be determined by the application itself and in some cases by the defects that can appear due to the AM process. Microstructure powder properties are also studied for the AM process specially the internal particle porosity due to its effect on the final density achieved [27].

As previously mentioned, one of the advantages of LPBF is the fact that the un-sintered raw material (i.e. powder) can be recycled to improve costs. But given the influence that particle size and shape have on the properties of the manufactured part, it is recommended to quantify these properties of the material prior the recycling.

### *2.2.4. LPBF – Defects*

AM is a complex manufacturing process and due to its differences with regards to conventional manufacturing processes it is important to analyze the defects specifically present in AM parts. Below the most common observed defects:

#### *2.2.4.1. Loss of alloying elements*

Due to the high temperature of the melt pool during AM, alloys present vaporization of alloying elements. Given that elements have different volatility, selective vaporizing may appear creating a difference in the composition of the alloy with regards to its initial value. Changes in the composition are not desired because they can influence the microstructure, the corrosion resistance and the mechanical properties of the manufactured part [22]. It was shown that the

surface area-to-volume ratio is a controlling factor into determining the magnitude of composition change. The variables influencing this defect are those affecting the geometry of the melt pool and the temperature distributions.

#### *2.2.4.2. Porosity and lack of fusion defects*

Given the consequences that they bring to the mechanical properties, porosity and lack of fusion voids need to be prevented as much as possible. Research has shown that these voids are produced by three main conditions. Firstly, at high energy density the melting can be performed in what is called keyhole mode [22]. Given the high energy density, keyholes can become unstable and continuously form and collapse trapping vapor inside that form the voids. The main factors related to keyhole porosity are laser power, laser scan velocity, laser beam and its interaction with the power bed [29]. This type of voids can be recognized by their spherical shape (refer to Figure 2-5) [22].

Secondly, the vapor trapped inside the voids can come from the powder particles themselves. During the powder manufacturing process called gas atomization, the entrapment of gas within the powder particles is a possibility. This gas gets trapped later on during the AM process and forms microscopic spherical pores. Entrapped gas can also come from the vaporization of the alloying elements of the powder [22].

Thirdly, at lower energy density lack of fusion defects appear. These are cause by the improper melting of the powder by an incomplete overlap of the melt pools. The melt pool has to be sufficiently big to penetrate and fuse the previous layer as well as the neighboring material [22], [29]. LPBF uses inert gas shielding, typically argon, to avoid contamination of the melt pool. Given the insolubility of inert gases in liquid metals, the shielding gas can potentially create pores within the workpiece. Lack of fusion voids are characterized by their elongated geometry and sharp edges that cause stress concentrations under applied loads (refer to Figure 2-5). These are macro-pores, typically larger than 10 µm [22].

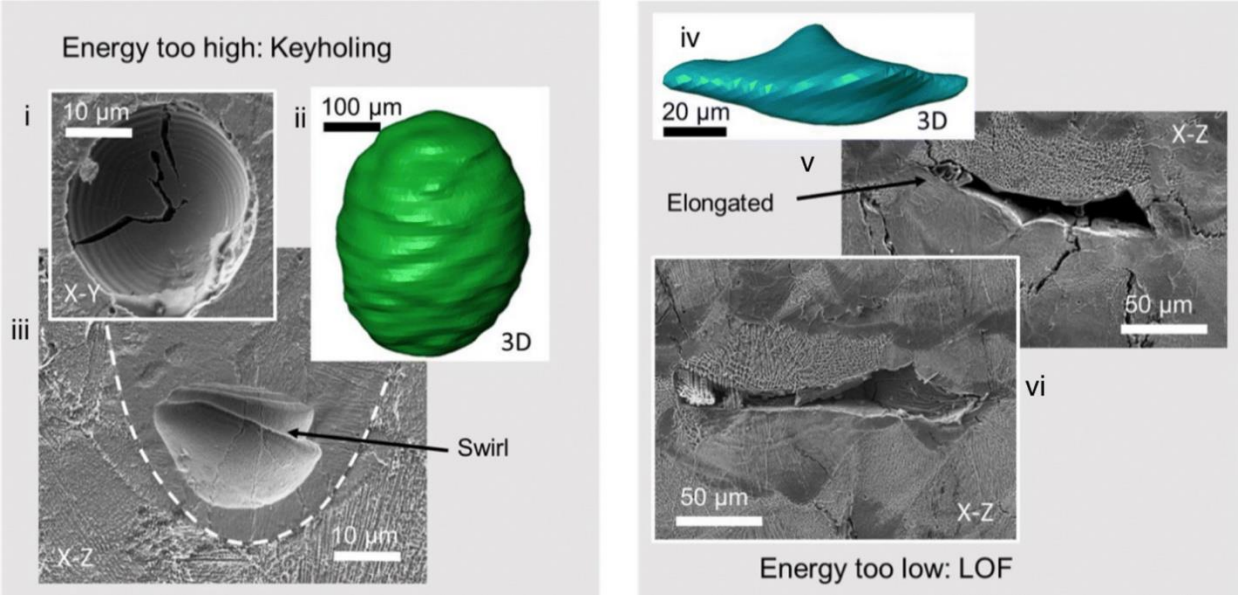


*Figure 2-5. Common morphology of keyhole porosity (left) and lack of fusion porosity (right). The images are taken from [30] research and they are from AM IN713C samples.*

#### *2.2.4.3. Surface Roughness*

Surface roughness of the final AM part is related to several independent variables and its importance makes it crucial to understand how to control it. Some parameters that influence surface roughness are heat source power, scanning speed, layer thickness, overhanging angles, scanning strategies, post-processing and finishing. It is said that AM parts for critical applications require at the most 1 µm of surface quality, therefore it is typical that some post-processes are performed to achieved the required finish. Machining, grinding, chemical polishing, hot isostatic pressure (HIP) and shot peening, are some of the typical post processes applied on the AM parts to improve the surface finish [22].

Even though surface roughness can be improved with post-processing it is still of interest to achieve a surface roughness as close as possible to the desired in order to save time on the post-processing step. Consequently, two different causes of the surface quality of an AM part are noted. Firstly, the so-called stair-step effect refers to the approximation of curved or inclined surfaces due to the layers of the AM process. This makes the average surface roughness $(R_a)$ dependent on the layer thickness and the building angle. It is important to keep in mind that the trade off with building a part with a smaller layer thickness is the time it takes to finish it and all

the other parameters that are associated with the reduction of layer thickness like powder particle size [22].

Secondly, improper melting of powder particles and balling effect reduce the surface quality of an AM part. When manufacturing with low energy density, the powder particles could potentially not melt completely and end up sticking on the surface of the part. The $R_a$ when this mechanism is present is approximately the size of the powder particle. When manufacturing with high scanning speeds, balling effect could be produced. This effect is the elongation of the melt pool that can break into small islands due to the Raleigh instability. The surface tension gradient inside the melt pool drags these small islands to the outer edges of the melt pool [22].

#### *2.2.4.4. Cracking*

Cracking occurs in AM parts in three different types. Firstly, solidification cracking which can be observed on the grain boundaries. This happens due to the solidification contraction and thermal shrinkage and the difference of it between the newly created layer and the previous layers of the part being built. The solidifying layer experiences a tensile stress as a consequence of the difference and if the magnitude of this stress exceeds the strength of the material cracking happens (see Figure 2-6). This is also known as hot cracking [22].

Secondly, a phenomenon known as liquation cracking could appear. This effect occurs when the Partially Melted Zone (PMZ) suffers heating below the liquidus line but certain lower melting point precipitates of the alloy are melted around the grain boundaries. This causes the PMZ to experience a tensile force due to the solidification shrinkage and thermal contraction of the new layer. Consequently, the liquid phases of the PMZ may act as cracking sites specially for aluminum alloys due to its high coefficient of thermal expansion causing larger contraction. Thirdly, delamination occurs when two consecutive layers separate due to the residual stresses at the interfaces that exceed the yield strength of the alloy used for building [22].

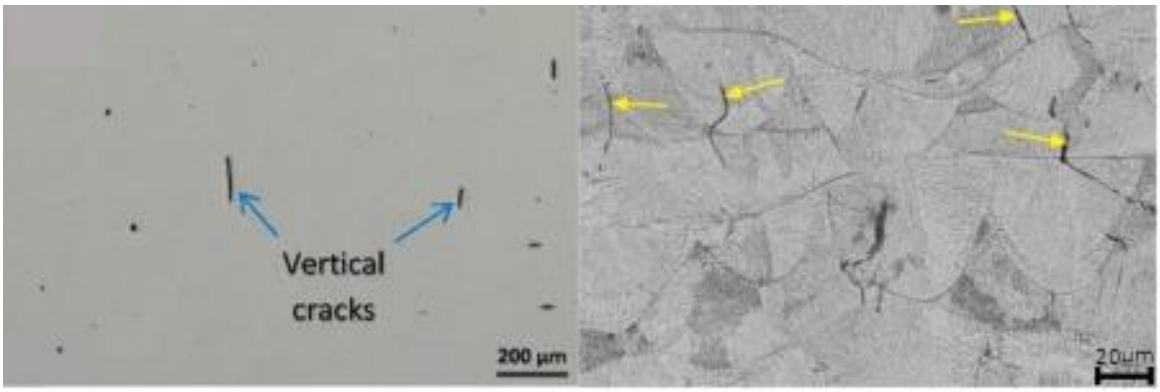


*Figure 2-6. Images of 316L stainless steel LPBF parts that suffered cracking [31].*

### 2.2.5. ***Mechanical Properties - LPBF***

AlSi12 is a commonly used aluminum alloy for AM. Due to the addition of silicon to the alloy it presents good parameters that make it suitable for AM, like castability, fluidity and low thermal expansion coefficient. The addition of Mg to the Al-Si alloys was performed as an attempt to create $Mg_2Si$ precipitates that will harden the alloy and improve the mechanical properties of it [2]. These alloys have been previously studied and therefore the achievable mechanical properties of this alloy are already known and documented (Table 2-1). Table 2-1 shows that the ductility and ultimate tensile strength values are similarly to the obtained via traditional processes like casting. Nevertheless, anisotropy is still important to verify prior because even if it is not showing and effect on AlSi10Mg tensile strength elongation, differences between longitudinally and transversally manufactured parts have been observed previously [22].

The focus has been guided toward aluminum alloys because the material to be used during the research for this thesis is an aluminum alloy under development. Consequently, the mechanical properties shown on this section may not reflect entirely the properties of the material in use but they will serve as a benchmark.

*Table 2-1.* Mechanical properties of aluminum alloys with regards to their processing parameters. Comparison between PBF and traditionally processed parts [22].

| Alloy | $P$ (W) | $v$ (mm/s) | $H$ (J/mm) | Post Treat. | Orien. | $E$ (GPa) | $\sigma_Y$ (MPa) | $\sigma_{UTS}$ (MPa) | Ductility (%) | $HV$ |
|---|---|---|---|---|---|---|---|---|---|---|
| AlSi10Mg | 250 | 500 | 0.5 | As-built | Long. | | 250 | 350 | 2.5 | 145 |
| | | | | | Transv. | | 240 | 280 | 1.2 | |
| | | | | T6[1] | Long. | | 285 | 340 | 4.5 | 116 |
| | | | | | Transv. | | 290 | 330 | 2.2 | |
| AlSi10Mg | 250 | 500 | 0.5 | As-built | Long. | | 125 | 250 | 6.6 | 75 |
| | | | | | Transv. | | 140 | 270 | 4.6 | |
| | | | | T6[1] | Long. | | 295 | 350 | 6.5 | 118 |
| | | | | | Transv. | | 285 | 340 | 4.9 | |
| AlSi10Mg | | | | As-built | Long. | 75 ± 10 | 270 ± 10 | 460 ± 20 | 9 ± 2 | 119 ± 5 |
| | | | | | Transv. | 70 ± 10 | 240 ± 10 | 460 ± 20 | 6 ± 2 | |
| | | | | 2h/300 °C | Long. | 70 ± 10 | 230 ± 15 | 345 ± 10 | 12 ± 2 | |
| | | | | | Transv. | 60 ± 10 | 230 ± 15 | 350 ± 10 | 11 ± 2 | |
| AlSi10Mg | 400 | 1000 | 0.4 | 2h/300 °C | Long. | | 182 ± 5 | 282 ± 5 | 25.2 ± 1 | |
| | | | | | Transv. | | 184 ± 5 | 288 ± 5 | 18.3 ± 1 | |
| AlSi12 | 350 | 930 | 0.38 | As-built | Transv. | | 369.3 ± 3.4 | 202.2 ± 4.3 | 4.38 ± 0.16 | |
| | | | | 240°C | Transv. | | 361.1 ± 4.5 | 201.5 ± 3.7 | 4.05 ± 0.15 | |
| AlSi10Mg | | | | HPDC | | 71 | 160–185 | 300–350 | 3–5 | 95–105 |
| | | | | HPDC-T6 | | 71 | 285–330 | 330–365 | 3.5 | 130–133 |
| AlSi12 | | | | Die Cast | | 71 | 131 | 290 | 3.5 | |

$P$= Laser Power, $v$= Scanning Speed, $H$= Linear Heat Input, $E$= Elastic Modulus, $\sigma_Y$= Yield Strength, $\sigma_{UTS}$=Ultimate Tensile Strength, $HV$= Vickers Hardness, HPDC=High Pressure Die Cast.

[1] Refers to solution treatment at 525°C for 6h, water quenching and subsequent aging at 165°C for 7h.

### 2.2.6. ***Process Parameters – LPBF***

Process parameters are meant to be modified from build to build if the situation requires it. Currently, there exist several modifiable parameters which include the most studied: laser power, layer thickness, laser scan velocity, hatch distance (or hatching space) and scanning strategies (laser scanning pattern), see Figure 2-7 [29].

Typically, the values of these parameters are obtained through experiments and research aimed at achieving denser manufactured parts, with less defects, while minimizing surface roughness and increasing building rate [29]. The values of the parameters may need to be adjusted depending on the machine and raw material that is being used.

LPBF process parameters can be tailored to prevent building defects or microstructure and materials issues. To reduce the porosity within the manufactured part one must look at the source of the porosity itself first. To control the porosity appearance due to keyhole mode, linear energy density must be modified [29]. Linear energy density is the ratio that appears from the following equation:

$$Linear\ energy\ density = \frac{Laser\ Power\ [W]}{Laser\ Scan\ Velocity\ \left[\frac{mm}{s}\right]} \quad (1)$$

In broad terms, the strategy is to decrease the linear energy density to avoid the keyhole mode and consequently the appearance of keyholes. This can be achieved by decreasing the laser power or increasing the laser scan velocity. But research suggests that decreasing the laser power has a bigger effect in reducing keyhole porosities [29], [32]. Also, preferential evaporation may occur due to the high energies experienced within the printing chamber. To control this defect, it is recommended to reduce the laser power and increase the laser scan velocity.

In regard to lack of fusion porosities, due to their relationship to the melt pool size and the scanning pattern, the parameters to control are the hatching space and the layer thickness. The goal is to have a minimum depth overlap between the two melt pools, preventing this type of porosities. It is highly recommended to select the laser power – laser scan velocity combination

first and then select the optimum hatching space and layer thickness for the application [29], keeping in mind that layer thickness is also restricted by the particle size of the powder.

Residual stresses are present in AM and specially in LPBF due to its high cooling rates. It has been observed that the length of the scan lines has an impact on the magnitude of residual stresses. Therefore, scan strategies become important to control the residual stresses, favoring those that reduce the length of the uninterrupted line of scanning [29].

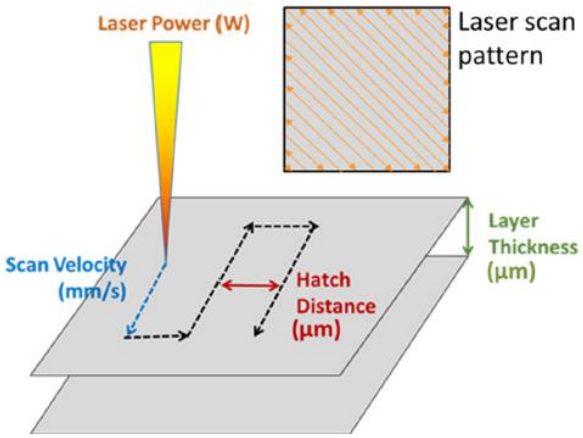


*Figure 2-7. Illustration of laser powder bed fusion (LPBF) processing parameters [29].*

The high cooling rates determine various properties of the final product. Solidification microstructure in melt pool techniques can be described by temperature gradient (G), solidification growth rate (R), undercooling (ΔT) and material parameters such as composition and liquid diffusivity. LPBF can be compared to laser welding because both of these processes experience large temperature gradients(G) and high growth rates (R). But LPBF experiences more moderate temperature gradients in comparison with welding processes. Consequently, the most commonly observed microstructures during LPBF are cellular dendritic, columnar dendritic, and equiaxed dendritic (see Figure 2-8). Note that the high growth rates in LPBF result in a refined microstructure, which in turn increases the strength of the AM parts compared to other conventionally process parts with the same material [29].

To control the material and microstructure related issues the recommended approach is the following: if micro segregation, increase laser scan velocity, if undesired texture or coarse columnar grains, reduce laser scan velocity, and if meta-stable phases, re-melt or reheat [29].

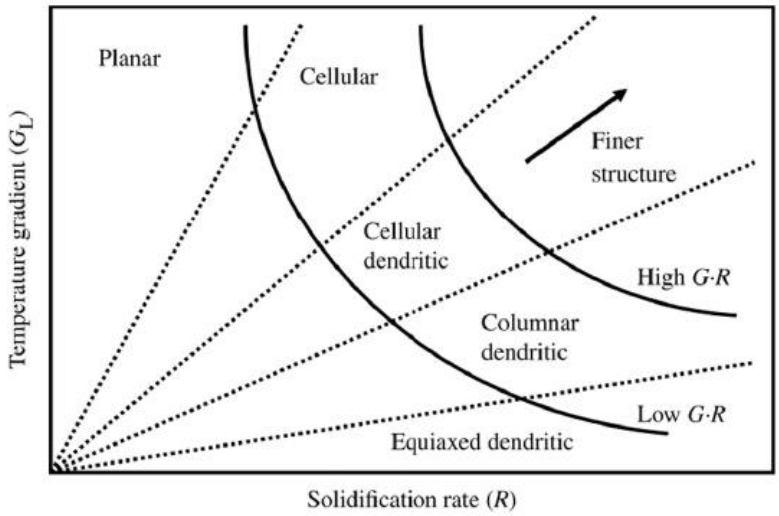


*Figure 2-8. Expected microstructure in relation to the temperature gradient (G) and the solidification rate (R). LPBF is expected to have cellular dendritic or columnar dendritic microstructures due to its cooling and growth rate [29].*

### *2.3. LATTICE STRUCTURES*

Cellular structure is a term employed to refer to foams, honeycombs, and lattices (Figure 2-9). This categorization was introduced by researchers Dhruv Bhate [33] and Tao and Leu [34] within their research. Foams represent the most prevalent type of cellular structure, characterized by randomly generated unit cell shapes and cell walls with arbitrary orientations in space. In contrast, honeycomb structures exhibit regular shapes, with uniform unit cells that can take various forms such as tetrahedrons, triangular prisms, square prisms, hexagonal prisms, among others [35]. Lattice structures, on the other hand, are arrangements formed by spatial arrays of unit cells with defined edges and faces. They can be defined as a porous three dimensional spatial structure formed by unit cells with different topological geometries [34], [36].

Lattice structures possess distinct advantages over foams and honeycombs due to their inherent flexibility in customization. Each unit cell, and even individual struts within the lattice, can be optimized as design variables to meet specific functional requirements. Consequently, the mechanical properties of lattice structures are more easily controlled compared to foams and honeycombs [36], [37]. Thus, lattice structures demonstrate superior mechanical characteristics in comparison to foams and honeycombs [36].

Leveraging the reduced weight of cellular structures enables the implementation of designs characterized by lightweight construction and enhanced strength. Given the current structural design tendency within the industrial sector that prioritizes both lightweight construction and high performance, lattice structures become an attractive solution for the industry. Ergo, due to their outstanding properties, lattice structures have found extensive application across aviation, bio-engineering, automation, and various other industrial sectors [36].

Based on the uniformity of cell distribution, lattice structures are categorized into two main types: uniform lattice structures and non-uniform lattice structures. Uniform lattice structures consist of porous structures characterized by a consistent distribution of unit cells. These unit cells exhibit identical topological shapes and geometric dimensions, arranged in a repetitive pattern throughout space. Conversely, non-uniform lattice structures comprise porous structures

where unit cells vary in their topological shapes or geometric dimensions, and their arrangement lacks repetition, resulting in an uneven distribution of materials [36].

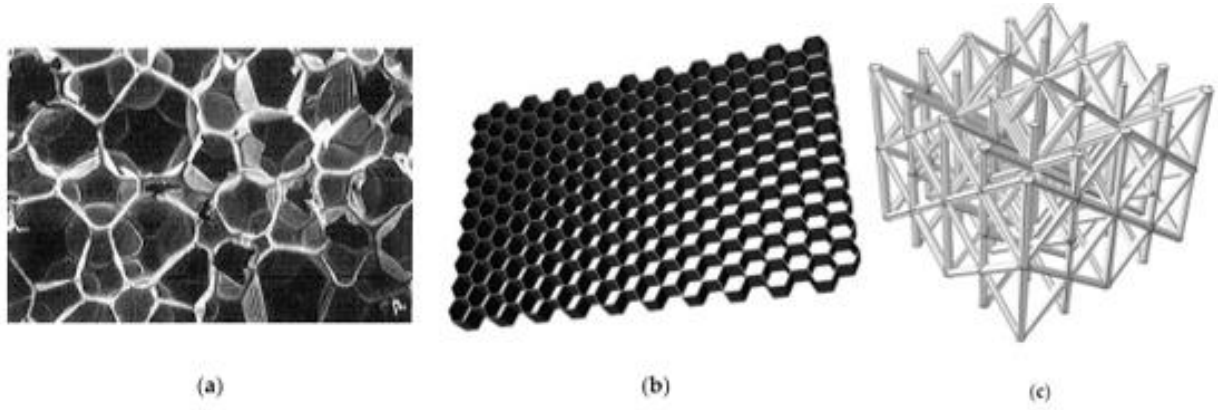


*Figure 2-9. Cellular structures, (a) foam, (b) honeycomb and (c) lattice structure [36].*

It is well-established that lattice structures exhibit favorable mechanical properties, which have undergone thorough research, resulting in the following findings:

- High stiffness and strength

Compression tests have been performed to assess the strength of samples containing various structural configurations, including solid, hollow, and lattice structures [38]. The findings revealed that while the strength of lattice structures was inferior to that of solid structures, it remained sufficient to meet application requirements, resulting in material reduction [36].

- High energy absorption

The energy absorption capacity of graded and uniform lattice structures was studied by Al-Saedi et al.[39]. Their findings revealed that the total cumulative energy absorbed by the graded lattice structure was 3.2 ± 0.1 MJ/m3, whereas the uniform lattice structure absorbed 2.6 ± 0.2 MJ/m3. The results show that graded lattice structures present slightly higher cumulative energy absorption per unit of volume than the uniform lattice structures [36], [39]. Nevertheless, the capacity of energy absorption of lattice structures is considerable.

❖ High damping

Lattice structures are great at reducing vibrations. Yin et al. [40] investigated the damping characteristics of Hollow Composite Pyramidal Lattice (CPL) via vibration testing. The experimental findings demonstrated that the CPL structure enhanced the material's damping properties, resulting in a significant damping effect [36], [40]. Therefore, the results provide enough data to support the use of lattice structures for damping applications.

❖ Heat dissipation

Experimental research has been carried out to prove that lattice structures have heat dissipation capabilities. Wadley and Queheillalt [41] conducted a comparison between copper textile-based lattice structures and various heat dissipation mediums. They observed that while the copper textile-based lattice structures performed comparably to stochastic open-cell metal foams (both aluminum and copper-based), they required significantly less pumping power. Consequently, their overall thermal efficiency was approximately three times higher than that of equivalent-weight open-cell copper foams [36], [41].

Currently, two main methods are employed to manufacture lattice structures: traditional machining processes and AM. The traditional processing and manufacturing methods used to produce lattice structures include water jet cutting, investment casting, electroless plating, electrodeposition. The additive manufacturing techniques employed for lattice structure fabrication are: fused deposition modeling (FDM), laser powder bed fusion (LPBF), selective laser sintering (SLS), electron beam melting (EBM), and binder jetting (BJ).

Traditional processing methods on one hand, enable the production of large-scale lattice structures, and on the other, they can be time-consuming, requiring cumbersome post-processing procedures, leading to increased energy consumption and material waste. In contrast, AM technologies present promising opportunities for the automatic and flexible fabrication of complex-shaped structures that are unattainable through conventional means [36].

The integration of lattice structures with additive manufacturing represents a significant advancement in industrial design. The fabrication of lattice structures using AM technology offers

several advantages, including design flexibility, the ability to produce structures across a wide range of sizes, compatibility with various materials, programmable automatic processing, energy efficiency, and cost reduction. However, AM also has its drawbacks; for instance, when designing lattice structures with suspended geometry, support materials are necessary, leading to material waste and increased post-processing time [36].

In terms of structure, lattice structures are formed by repeating a unit cell following a specific spatial arrangement. The unit cell represents the smallest component defining the entire lattice structure. Various methods can be employed to design the unit cell: a primitive-based approach, where the unit cell comprises geometric primitives; an implicit surface-based technique, defining the unit cell's surface through mathematical equations; and a topology optimization method, obtaining cell geometry via optimization calculations. An essential unit cell parameter is porosity, denoting the volume fraction of pores within it, significantly impacting overall mechanical properties [34].

Pattern design involves how unit cells are replicated in three-dimensional space. A lattice can be constructed from a unit cell array using direct patterning, involving translational repetition of unit cells; conformal patterning, where units are repeated to conform to a specified surface geometry; and topology optimization, which optimizes material distribution within a single unit cell and orchestrates spatial replication of the unit cell throughout the entire design space [34].

Chen et al. [42] classified lattice structures according to their topologies, giving a result the following: strut-based lattice structures, triply periodic minimal surface (TPMS) lattice structures, and shell lattice structures (refer to Figure 2-10) [42], [43]. The strut-based lattice structure exhibits a periodic arrangement of unit cells comprised of struts and nodes [44], also known as beam-based lattice structure. These unit cells can be characterized by the numbers of struts (*s*) and nodes (*n*), which collectively determine the Maxwell number (*M*) of the unit cell. The value of M can imply if the number of struts within the design causes, or not, a balance of external forces. The relationship among *s*, *n*, and *M* is expressed as follows [42], [45]:

$$M = s - 3n + 6 \quad (2)$$

Triply periodic minimal surface (TPMS)-based unit cells are defined by a periodic structure across three coordinates with zero average surface curvature. TPMS relies on implicit equations to determine an array of points on the unit cell surface where the function $F(x, y, z) = 0$, equals zero [42], [46].

Additionally, unit cells composed of plates, rather than struts or continuous surfaces, are referred to as shell unit cells or shellular, first introduced in 2015. Although these structures may not always maintain zero mean curvature, they are commonly known as TPMS-like lattice structures [42], [47]. This is the type of unit cell that Tao et al. [34] do not consider within their methods to design lattice structures, but the strut-based or TPMS-based lattice structures have a parallel in their classification.

It can be concluded that the unit cell significantly influences the mechanical properties of produced lattice structures, even when structures exhibit similar relative densities and are fabricated using the same technology [42]. In addition, the pattern design will determine the uniformity, or lack off, of the structure itself, and as previously mentioned this is a determinative factor for some of the main properties of lattice structures.

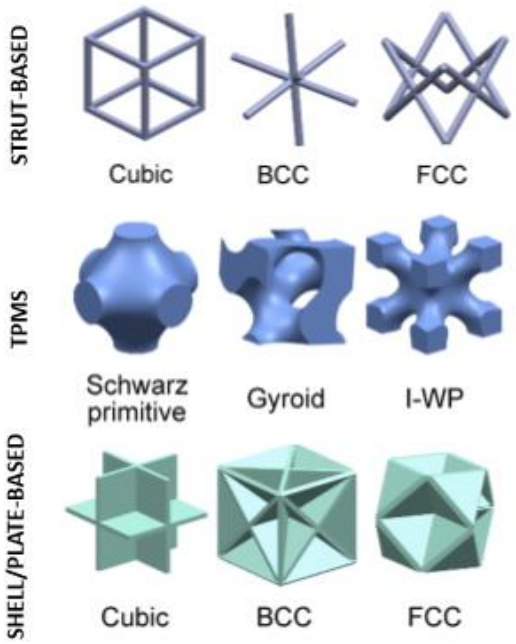


*Figure 2-10. Lattice structures classified based on their topology [48].*

### *2.4. X- RAY COMPUTED TOMOGRAPHY*

Industrial X-ray computed tomography, commonly known as CT scanning or XCT, is a non-destructive scanning technique that allows the visualization of both the outside and inner surfaces of a workpiece. Depending on the sought-after resolution the scanning method can be relatively fast making it a good scanning technique to utilize during research activities. Particularly, XCT scanning is of interest for its versatility, it allows measurements but also the visualization of material flaws such as porosities or voids. As showed by Jacobs et al. [49], CT images can provide enough information to determine porosity and even composition of the workpiece, allowing its user to identify the different proportions of alloying elements within the workpiece. Industrial XCT is particularly enticing because of its non-destructive nature, previously to make the type of measurements and analysis that this technique allows it was necessary to cut the workpiece.

#### *2.4.1. X- Ray Tomography Principle*

X-Ray computed tomography uses the ability of x-rays to penetrate objects and the fact that part of them is absorbed when penetrating the object. The longer the length of the object the less radiation that escapes on the opposite site of it but the level of absorption also depends on the material itself [50]. Therefore, an X-Ray detector (Flat panel) captures the radiation that escaped through the object as a 2-D radiographic image, also known as projection. The workpiece must be positioned between the source (X-ray source) and the detector for the process to work. On Figure 2-11 (a) we can see the described principle, notice how the x-ray source emits a cone-beam of x-rays and how they are captured by the detector behind the workpiece [50].

To obtain the tomography of the workpiece, a large number of projections are taken while the workpiece rotates (Figure 2-11). The rotation of the workpiece can be made continuously or step-by-step, the latter is preferred but it brings as a consequence a longer scanning time. Based on the projections acquired from the rotation, cross-sectional images of the workpiece are calculated (CT images), process known as reconstruction [51]. These images describe the distribution of the material density of the workpiece within the considered plane and they can be stacked to form what is known as CT volume or voxel. Voxel size is of particular importance

when talking about CT scans because it determines the resolution level acquired via the tomography.

In order to distinguish between air and the workpiece material, surface determination has to be performed. The global grey value thresholding operation is performed to indicate what value of grey corresponds to the air and consequently what values correspond to the workpiece. This step is of particular importance when trying to distinguish between different alloying materials of the workpiece as well as the porosity of it. Because the attenuation of the X-rays depends on the material, the grey level of the CT images will indicate (if done successfully) the different materials within [51].

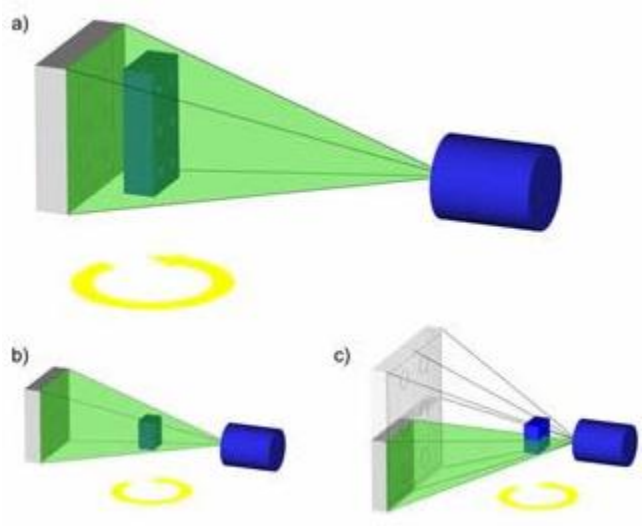


*Figure 2-11. (a) Basic principle of x-ray tomography, (b) Magnification adjustment achieved by movement of the measured object relative to the sensor and to the radiation source, (c) Type of tomography where images from various positions are stitched [50].*

There are several factors that influence the spatial resolution achieved by the XCT system, the size of the X-ray focal spot (Section 2.4.2), the performance and the resolution of the detector (Section 2.4.3), the magnification of the system, the number of projections, the reconstruction algorithms and any applied filtering [52].

Spatial resolution defines the ability to capture fine structural detail in the workpiece through the image. It is commonly quantified in terms of the smallest separation that allows to identify two different points as separate entities. It can be interpreted via the voxel size of the CT image.

Voxel size is a function of: geometric magnification (*m*), number of detector pixels perpendicular to the rotation axis (*n*), the detector pixel size (*d*) and the number of voxels into which the data is reconstructed (*NoV*) [51].

$$Voxel\ size = \frac{(n)(d)}{(m)(NoV)} \tag{3}$$

Geometric magnification is defined as the ratio of source to detector distance (*SDD*) over source to sample distance (*SPD*) [51]. From Equation (4) it is easy to see that different source to sample distances can create the same magnification value by modifying the source to detector distance. Typically, magnification is the parameter most easily modified when setting up a scan to achieved the desired voxel size. Figure 2-12 illustrates all of the parameters that belong to the voxel size calculation (Equation (3)).

$$m = \frac{SDD}{SPD} \tag{4}$$

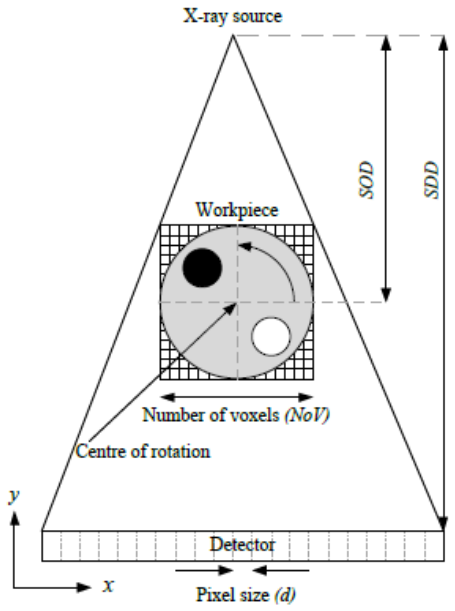


*Figure 2-12. Illustration of x-ray tomography crucial parameters for voxel size and magnification calculation [51].*

Consequently, XCT scanning is broadly used in analyzing the different samples acquired by AM processes because it helps quantify and identify the defects inside the samples after the manufacturing process.

### *2.4.2. X- Ray Source*

As shown on Figure 2-11, an XCT system is composed basically by three components, the X-ray source, the workpiece to be scanned (with its manipulation system) and the detector. A computer where the reconstruction of the radiographs will be performed can be added to the list of components of the system too [52]. Throughout this section the different types of X-rays sources, their advantages and disadvantages as well as their different applications will be discussed.

X-rays are produced via the acceleration of electrons inside a vacuum tube that are made to collide with a metallic target. The X-rays get produced by two different processes, bremsstrahlung and characteristic radiation. Bremsstrahlung, also known as braking radiation, is created when and electron passes extremely close to the nucleus of an atom (of the metallic target) but does not collide with any part of it. By the closeness of the electron to the nucleus, it gets affected by a strong nuclear attraction due to the difference of positive and negative charges of the nucleus and the electron. The loss of energy caused by the interaction creates a photon with the same amount of energy lost. The electron is consequently deaccelerated and the radiation occurred is known as bremsstrahlung radiation. It is important to note that the probability of this occurring depends on the metallic target atomic number and of the energy of the accelerated electrons inside the vacuum container [52].

Characteristic radiation occurs when an electron directly collides with one of the shell electrons of the metallic target atoms, thus creating a vacancy. The vacancy is filled with an electron from an outer shell and a discrete spectrum of X-rays is emitted. The characteristic radiation emitted X-rays get superimposed to the continuous X-rays that is emitted via the bremsstrahlung radiation (see Figure 2-13) [52]. This implies that the X-ray source of a CT scanning machine does not produce rays will a singular energy but with different ranges of

energy. The different energies of the X-rays have consequences on the quality of the acquired CT images, discussed in detail further on.

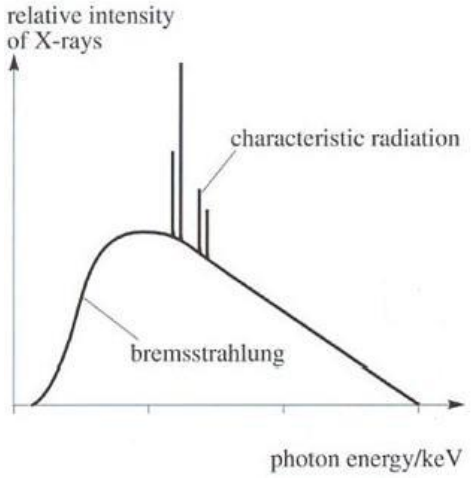


*Figure 2-13. Illustration of x-ray spectrum and the superimposition of characteristic radiation and bremsstrahlung x-rays [52].*

Inside an X-ray source there are two main parts, the filament (cathode) and the metallic target (anode). The source has to be under vacuum to avoid the interaction with molecules of gas and the production of lower energy electrons that this interaction produces. The filament, cathode, is typically made of tungsten and the target (anode) generally contains small amounts of tungsten, molybdenum or copper. When the X-ray source is powered up, the electrical heating produced on the filament creates electrons by thermionic emission. The electrical potential accelerates the electrons towards the metallic target, thus creating the X-rays. Depending on the thickness of the target and the energy of the electrons the x-ray photons get transmitted through the target or reflected by it. Approximately only 1% of the energy generated gets converted into X-rays the remaining gets dissipated has heat [52].

Essentially there exist two different types of X-ray sources, open or closed. Closed tubes are vacuum sealed and the spot size of the source is the actual size of the X-ray hitting the target. Open tubes require vacuuming of the tube due to its openness, but can provide a smaller focal spot under high output (compared to the closed tube) [53]. Open sources provide the possibility of replacement of consumables, thus giving it long lifetime. But if a smaller focal spot is not necessary, then a closed source is preferred due to its lower price and ease of use. [54].

Focal spot is an important parameter that essentially determines the achievable image quality. The size of the focal spot will influence the voxel size. Microfocus systems have spot sizes between 1 µm to 1000 µm, and nanofocus systems have spot sizes lower than 1 µm. Typically focal spot sizes decrease in size when the power is lowered but low power limits the imaging abilities [52].

Because x-rays are produced thanks to a voltage and a current supplied to the X-ray source, they are important parameters to manipulate. Broadly speaking, voltage determines the X-ray spectrum. Increasing the supplied voltage decreases the wavelength of the emitted X-rays, meaning more energy. Increasing the applied current, with constant voltage, increases the X-ray intensity without modifying its spectrum [52].

### *2.4.3. X- Ray Detector*

There exist several types of X-ray detectors but the standard ISO15708 divides them into two groups: direct detectors (ionization) or scintillation detectors (indirect) [52].

- Direct semiconductor detectors

  This type of detectors produces an electrical current when they are exposed to X-rays. Some direct detectors use photoconductors implemented as a coating on a multi-pixel electronic plate. The output current of such devices is collected by an array of thin film transistors (TFTs). Direct detection has the advantage of the increased sensitivity. The detector acts as a single photon counter [52].

- Scintillation detectors

  Scintillation is defined as a flash of light produced in a transparent material thanks to an ionization event. Scintillation detectors have the ability to convert high-energy X-ray photons to lower energy photons on the visible range. These low energy photons are detected via a photomultiplier tube or photodiode. This type of detector is more sensible to lower doses of X-rays.

X-ray detector is a crucial part of the XCT system and it influences greatly the spatial resolution achieved. By modifying the distance of the detector to the source or by changing the

detector's pixel size, a change in voxel size is created and therefore on the spatial resolution [51], [52].

### 2.4.4. *Data Processing*

Without the reconstruction step, the data acquired by the X-ray's scans are common radiographs that are helpful but do not serve the purpose of CT images. Consequently, understanding the principle behind the reconstruction step will help to get better CT images. Following the principle of XCT systems explained in Section 2.4.1, it is known that the X-ray beam penetrates the sample and creates a projection on the detector. The resultant radiographic image is a projection of the workpiece and each pixel has an intensity that is a function of the attenuation coefficient and the thickness of the sample. Meaning, that with a detector of $M\ x\ N$ pixels and with a number of projections $P$, at different angles, the reconstruction process involves solving a cubic matrix of $M\ x\ N\ x\ P$ attenuation coefficients [52].

For performing the reconstruction of the projections acquired from the XCT system, it is necessary to find a function $f(x)$ representing the medium, given the knowledge of the projection. This can be done by using an inverse Radon transform and it is known as back projection. Filtering processes are applied before or after the back projection to avoid the blurring of the images. The most typically used filter is a low pass filter but there exist different types of filters that can be applied to create successful CT image reconstructions [52]. The most efficient reconstruction algorithm for cone-beam and flat panel detector was developed by Feldkamp and was adapted from the fan beam algorithm [55].

### 2.4.5. *Visualization*

There exists several commercial software that allow the volumetric visualization of the reconstructed CT images. One of the available software packages is Avizo. This software created and distributed by Thermo Fisher Scientific allows the analysis and visualization of imaging data. The software has extension modules to satisfy different purposes and needs, allowing customization and automation [56]. Typically this kind of software allows measurement analysis, material characterization, segmentation and visualization of the acquired XCT data [52].

### 2.4.6. ***Errors***

XCT technologies experience systematic errors, some of the most common errors are discussed below.

❖ BEAM DRIFT

The accuracy of an XCT system is influenced by the spatial stability of the X-ray focal spot, known as beam drift. This issue is related to the thermal expansion of the X-ray tube and the variation of the dimensions suffered because of it. The common solution is to integrate a cooling system inside the X-ray tube and maintain the cooling unit inside the measurement chamber. This has shown to improve the thermal control characteristics of the cooling system.

❖ RING ARTEFACTS

Ring artefacts are related to defects in detectors, poor calibration of detectors, non -linear behavior of detector materials, finite sensitivity of the detector, poor uniformity or mechanical misalignment between X-ray source and the detector. Therefore, it is no surprise that this error is a common issue. Having a constant sensitivity across the complete detector plays an important role. The defect presents itself when a pixel of the detector is malfunctioning and consequently the reconstructed images present a ring like artefact (see Figure 2-14) [52].

The occurrence of ring artefacts can be reduced with the calibration of the detector, if there has not been permanent damage to the detector itself. But they can be corrected numerically by switching from cartesian coordinate system to polar coordinate system.

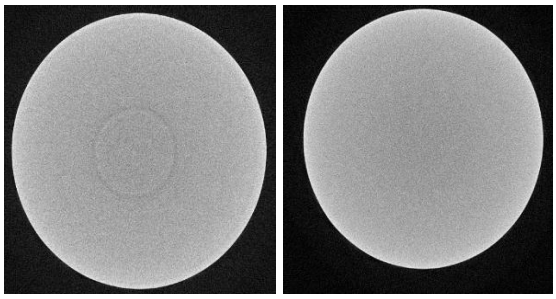

*Figure 2-14. Ring artefacts (left) viewed in a CT image and the corrected version (right) [52].*

❖ BEAM HARDENING

Beam hardening is a consequence of a polychromatic X-ray beam. A polychromatic X-ray beam is a beam that consist of X-rays with different radiation wavelengths, meaning different energies. Consequently, polychromatic X-ray attenuation cannot be described by a simple linear attenuation coefficient [57]. The reconstruction algorithm assumes that the absorption of the X-rays is a property of the material and independent on their energy level. This discrepancy between the algorithms assumption and the reality creates beam hardening causing the edges of the workpiece to look brighter than the interior [52].

There exist three primary methods to correct this effect, pre-processing, post-processing and dual energy methods. A filter in the form of a thin plate of copper or aluminum can be mounted between the source and the workpiece to remove the low energy X-rays. This method, although relatively easy to implement and effective, reduces the signal-to-noise ratio which can be problematic later on. Numerical correction of this error is also available through reconstruction software. The dual energy method produces images with different contrast characteristics than common X-ray images. The method utilizes two X-rays beams in order to calculate the energy dependency needed to correct beam hardening [52].

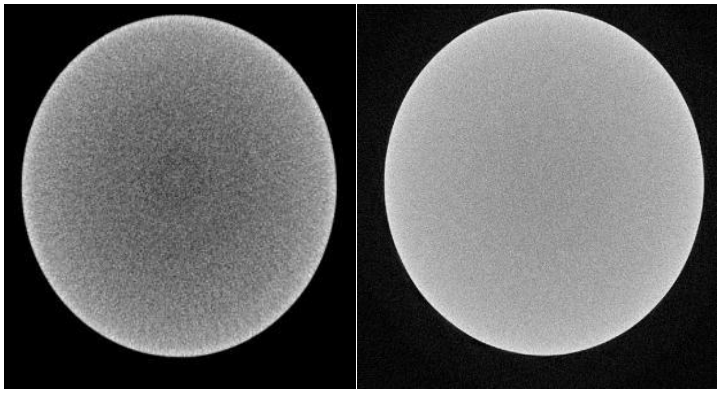

*Figure 2-15. Beam hardening defect (left) viewed in a CT image and the corrected version (right) [52].*

### 2.5. *DIGITAL VOLUME CORRELATION - DVC*

It's widely acknowledged that experimental verification of theoretical predictions is fundamental across scientific disciplines, specially within solid mechanics. Thus, achieving full-field strain measurement has long been a primary objective. The emergence of numerical tools like the finite element method has enabled the availability of full-field quantities, leading to a situation where prediction capabilities often surpass verification capabilities. The challenge arises from the nature of the quantities of interest—stress and strain— which are second-order tensors that vary over geometrically complex domains. While traditional methods like strain gauges offer high accuracy, they are limited to measuring at relatively few discrete points [58].

Early attempts at full-field strain measurement, notably through techniques like photo elasticity, provided valuable insights. However, their utility was hindered by practical constraints and challenges in data analysis. The turning point came with the advancement of digital imaging technology in the 1970s, coupled with the exponential growth in computer capabilities. This ushered in a new era of strain measurement techniques [58].

Particularly, the emergence of 3D imaging techniques sparked significant advancements in instrumentation and accessibility, positioning microtomography as a favored tool in materials science. The ability to register different images, enhanced the qualitative and quantitative understanding of changes. When imaging the same sample under varying loads, the advantages become evident. Consequently, testing set-up started to be developed. The inception of mechanical experiments combined with x-ray tomography traces back to observations of crack openings in aluminum alloy [59], [60]. Subsequent advancements have not only improved testing setups but also deepened the understanding of various degradation mechanisms, brought to light through bulk material observations. With access to ex-situ or in-situ observations across different loading scenarios, the next pivotal step was measuring displacement fields within the imaged samples. The pioneering 3D displacement measurements via Digital Volume Correlation (DVC) were conducted on trabecular bone subjected to in-situ compression in a computed microtomographic (µCT) scanner [59], [61]. This approach, initially local in scope, has since found applications in biomechanics and beyond.

DVC measurements have enabled the investigation of various classes of materials within the realm of solid mechanics. Tomography plays a crucial role in unveiling their in-situ temporal evolution, a facet typically inaccessible through post-mortem investigations. These observations are subsequently juxtaposed with numerical simulations for validation purposes. Localized phenomena, such as strain localization and crack formation, highlight the significance of full-field measurements, especially when kinematic assessments can be conducted nondestructively within the material bulk. Therefore, DVC is increasingly favored for quantifying various deformation and failure mechanisms. Keep in mind that uncertainty quantification in DVC analyses is intricately tied to the acquisition methodology of the 3D images [59].

### *2.5.1. Main Principle*

There exists a consistent general framework for spatial-domain DVC, refer to Figure 2-16. Consider a voxel volume encompassing a global spatial domain. The rendered volume constitutes a three-dimensional array of discrete values representing aspects of material-energy interaction averaged over small regions (voxels) within the sample. It's important to note that each voxel value corresponds to a discrete point at the voxel's center, with values for points between voxel centers estimated through approximation methods [58].

The DVC process begins with the delineation of a region of interest (ROI) containing points where displacement values are sought. This region's geometry is defined within the global voxel domain and meshed using standard tools, with the mesh nodes serving as displacement measurement points [58].

The subsequent phase of DVC is the most demanding and crucial—estimating the displacement vector at each measurement point through correlation of a reference (undeformed) image volume with a target (deformed) image volume [58]. The reference image can be represented as $f(x)$, and the target image as $g(x)$, where $f$ and $g$ denote scalar gray levels at each voxel location $x$. Essentially, DVC operates on the premise that with a mere shift in voxel positions, described by a displacement field $u(x)$, the two images can align perfectly, satisfying the equation [59],

$$g(x + u(x)) = f(x) \tag{5}$$

There exist some errors, related to noise or other issues that may cause deviations from the true solution. Therefore, the subsequent phase involves establishing an objective function that measures the level of agreement between the reference and target volumes. The sum-of-squares correlation coefficient (SSCC) is commonly utilized for this purpose. Finally, strains are calculated at all measurement locations based on the displacement vector field [58].

Several common issues drive the need for enhancements [59]:

- Images are strictly defined only at integer voxel positions. However, the displacement field ($u$) may assume arbitrary values in practice [59].
- Images are inherently discrete, not just due to voxel structures but also because of the gray level encoding. This limitation is less significant in computed tomography where gray levels are computed [59].
- Images often contain noise. Even in cases where no motion is anticipated between two consecutive images of the same scene acquired with the same device, the images ($f$ and $g$) may still differ [59].

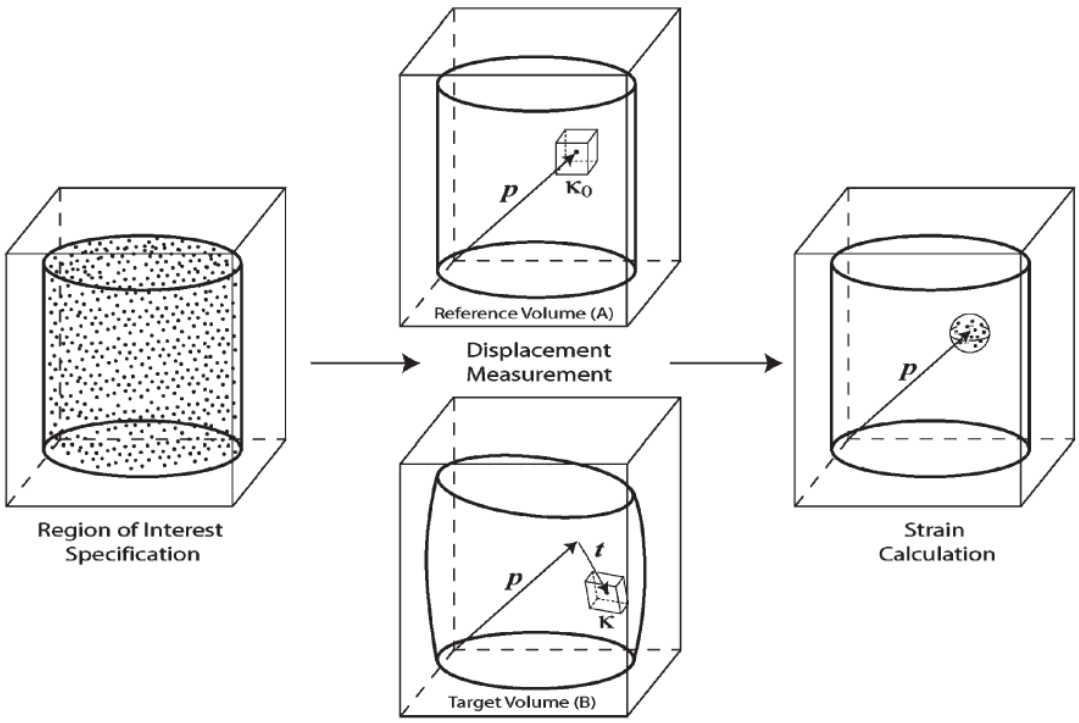


*Figure 2-16. DVC process and its steps: (a) defining a region of interest containing measurement locations; (b) measuring displacement at each location through correlation of reference and target digital volumes; and (c) calculating strain at each point by estimating the surrounding deformation gradients [58].*

### 2.5.2. ***Application***

Specifically, DVC has been used to measure the strain of the samples during testing in bone and in bone-cement interface [62]. From this research it can be concluded that the measurement accuracy (mean) and the precision of the measurement (standard deviation) depend on the micro-texture of the material and the choice of sub-volume size respectively. Therefore, sub volume size has to be chosen wisely and a compromise between the measurement uncertainty and the spatial resolution has to be made. This selection will vary depending on the material and their differences in microstructures and textures. Finally, it can be concluded that DVC is a reliable enough solution for strain field characterization of high-performance materials in pre-yielding regime [62], [63]. However, strain results differ between the DVC and finite element models at tissue level for the researched carried on by Zu et al. [62]. This implies a current limitation of DVC which will have to be considered, refer to Figure 2-17.

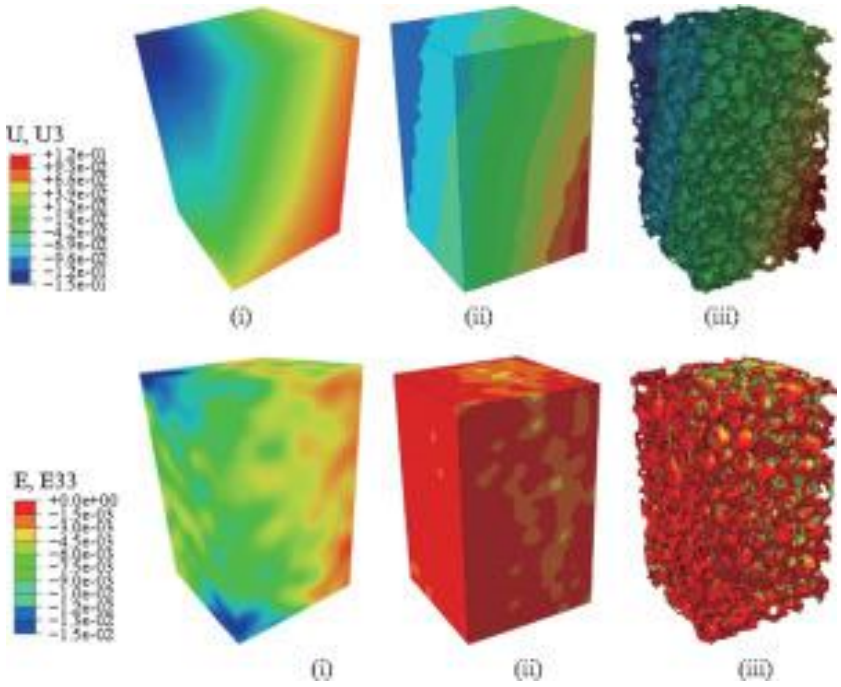


*Figure 2-17. Comparison of displacement (top) and the strain (bottom) distributions from: (i) DVC calculation with 64 voxels sub-volume size; (ii) average FE results from continuum mapping; (iii) micro FE results [62].*

## 3. PROBLEM STATEMENT.

The objective of this research, as outlined in this document, is to evaluate the feasibility of manufacturing lattice structures using a novel aluminum alloy currently being developed at the Research Institute of Mechanics, Materials, and Civil Engineering (iMMC) of the Catholic University of Louvain, under the guidance of Prof. Aude Simar.

This investigation aims to explore the capabilities of the institute's laser powder bed fusion (LPBF) machine in manufacturing lattice structures with this new aluminum alloy, considering achievable dimensions and print quality. Additionally, the study seeks to characterize the morphology and the mechanical properties of the lattice structures. Of particular interest is the examination of the healing properties of the aluminum alloy and their manifestation within the lattice structure.

The research will address the following questions:

- What are the smallest lattice structure dimensions realistically achievable with the current expertise and the LPBF machine at the iMMC research facility?
- Which set of printing parameters yields the best results in terms of print quality, dimensional fidelity, and internal porosity for the selected lattice structures?
- How does the lattice structure morphology appear with the selected printing parameters?
- What is the compression behavior and tendency of the lattice structures made with the new aluminum alloy under development?
- What does the DVC analysis reveal about a lattice structure under compression loads?
- How does the lattice structure behave under the healing heat treatment (HHT) intended for the aluminum alloy under development?
- What is the pathway to achieve healing in lattice structures manufactured from the new aluminum alloy?

# 4. MATERIALS AND METHODS.

## *4.1. RAW MATERIAL – AlMg14Zr1*

The raw material to be used is a pre-alloyed gas atomized powder bought directly from a manufacturer. The expected composition in weight percentage is Al 85 %wt., Mg 14%wt and Zr 1%wt. The specific composition of the powder previous its use on the LPBF machine was analyzed by Inductively Coupled Plasma (ICP) and by a three-acid attack, the results are shown on Table 4-1. It can be concluded that the true composition of the powder is AlMg14.02Zr1.01 with a small impurity of Fe, which is common for commercially pure Al alloys and powders, and a Sn impurity which is not common nor expected. The Sn impurity, given its unexpectedness, was not corrected in time for any of the research carried throughout this document but its presence will be considered.

*Table 4-1.* Inductively Coupled Plasma (ICP) spectroscopy and three-acid attack were employed to characterize the pre-mixed powder used throughout this research. The mean between the two methods will be used as the true value of the composition. Note that the value for each technique is the mean of two separate samples of the powder.

| | **COMPOSITION IN PERCENTAGE OF WEIGHT [%wt.]** | | |
|---|---|---|---|
| | ***ATTACK – HF/HCl/$HNO_3$*** | ***DIRECT FUSION*** | ***MEAN*** |
| **Al** | 84.40 | 84.45 | **84.42** |
| **Cr** | 0.01 | 0.01 | **0.01** |
| **Cu** | <0,01 | <0,01 | **<0,01** |
| **Fe** | 0.06 | 0.06 | **0.06** |
| **Ga** | <0,01 | <0,01 | **<0,01** |
| **Mg** | 14.00 | 14.05 | **14.02** |
| **Mn** | 0.01 | 0.01 | **0.01** |
| **Ni** | 0.01 | 0.01 | **0.01** |
| **Si** | _ | _ | **_** |
| **Sn** | 0.07 | 0.08 | **0.07** |
| **Ti** | 0.01 | 0.01 | **0.01** |
| **Zr** | 1.01 | 1.01 | **1.01** |

### *4.1.1. MORPHOLOGY – AlMg14Zr1*

The morphology of the powder was assessed prior to its use in the LPBF process through a sieving method. A 63 µm sieve was employed to ensure the powder particles did not exceed this maximum powder particle size.

### *4.2. LATTICE STRUCTURE*

As discussed in Section 2.3, the Maxwell number (*M*) provides insights into the lattice structure to be used. Specifically, it indicates whether the number of struts within the design balances external forces. Depending on the value of *M*, different types of structures emerge [64]:

- $M < 0$ – Bending dominated behavior
- $M > 0$ – Stretch dominated behavior

In Figure 4-1, various unit cells are displayed. Almost all the unit cells shown exhibit bending-dominated behavior, which, compared to stretch-dominated structures, result in higher compliance and lower strength. For lattice structures with bending-dominated behavior, the struts inclined to the loading direction will exhibit elastic bending, while the deformation in the other struts can be considered negligible.

| Cell type | BCC | FCCZ | FBCCZ | FBCCXYZ | BCCZ | FCC |
|---|---|---|---|---|---|---|
| |  |  |  |  |  |  |
| Struts, *s* | 8 | 20 | 28 | 44 | 12 | 16 |
| Joints, *n* | 9 | 12 | 13 | 15 | 9 | 12 |
| Maxwell number, *M* | −13 | −10 | −5 | 5 | −9 | −14 |
| Strut aligned to load direction | No | Yes | Yes | Yes | Yes | No |

*Figure 4-1. Different types of unit cells with some characteristics, number of struts (s), number of joints (n), Maxwell number (M) and if the strut is aligned to the load direction [64].*

For this research, the body-centered cubic (BCC) unit cell will be utilized. This unit cell is relatively straightforward to modify, with strut diameter and strut length being its primary parameters. Here, “strut” refers to the cylindrical beams that make up the structure, and henceforth, “strut” and “beam” will be used interchangeably. The bending-dominated behavior of the structure will provide insights during the planned in-situ compression tests. Additionally, due to its simplicity, the BCC unit cell serves as an ideal starting point for further research. Previous studies have explored similar structures using a titanium alloy [64], offering a useful comparison for evaluating the behavior of the aluminum alloy under investigation and understanding how it compares to other materials.

The lattice structure design and CAD model for this research was created using Solidworks software, with its parameters detailed in Figure 4-2 and Table 4-2. The structure was created to employ the smallest beam diameter achievable. The overall dimensions of the lattice structure were adjusted to fit inside the in-situ tester, ensuring its suitability for subsequent research steps (Figure 4-3). Additionally, a preliminary LPBF process was conducted to evaluate the machine's capability and the powder's suitability for manufacturing the intended lattice structure. The parameters used for this process are outline in Table 4-2, with further details provided in section 4.3.

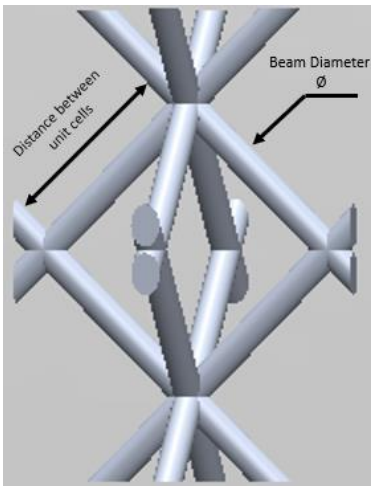


*Figure 4-2. Nomenclature and definition of parameters for controlling the BCC lattice structure in this research.*

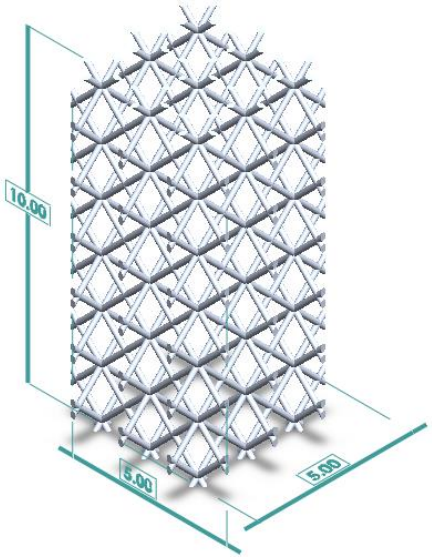


*Figure 4-3. Overall dimensions of the lattice structure specimens. The repetition of the unit cell in three dimensions forms a parallelepiped rectangle with dimensions: 5mm x 5mm x 10 mm.*

*Table 4-2.* The table details the dimensions of the manufactured lattice structures. Specimens labeled with letters correspond to preliminary specimens produced to assess the capabilities of the machine and powder. Specimens labeled with numbers correspond to the final dimensions of the manufactured specimens intended for further testing.

| | BEAM DIAMETER Ø [mm] | DISTANCE BETWEEN CELLS [mm] | $\rho_{rel}$ [%] |
|---|---|---|---|
| **SPECIMEN A** | 0.100 | 1 | 1.6 |
| **SPECIMEN B** | 0.500 | 1 | 24.3 |
| **SPECIMEN 1** | 0.150 | 1 | 3.3 |
| **SPECIMEN 2** | 0.100 | 1 | 1.6 |

The determination of the relative density of the lattice structure is significant for this study due to its impact on various properties. The calculation uses the following formula,

$$\rho_{rel} = \frac{\rho_{latt}}{\rho_s} = \frac{V_{latt}}{V_s} \quad (6)$$

Here $\rho_{latt}\ \left[\frac{kg}{m^3}\right]$ represents the density of the lattice structure, while $\rho_s\ \left[\frac{kg}{m^3}\right]$ denotes the solid density. $V_{latt}\ [m^3]$ and $V_s\ [m^3]$ denote the volumes of the lattice structure and the solid, respectively. The relative density was computed using the lattice and the solid volumes, as determined from the CAD model.

### 4.2.1. ***Lattice Structure Stress and Deformations***

Since lattice structures are categorized as cellular structures, their stress- strain engineering curve looks somewhat different. Typically, the curve is divided into three regions: linear elastic, permanent plastic (due to yielding, buckling or fracture), and densification (Figure 4-4). Three main parameters can be taken from this curve: the elastic modulus (*E*, also known as young's modulus), the plateau stress $\sigma_{pl}$, and the densification strain $\varepsilon_d$ [64].

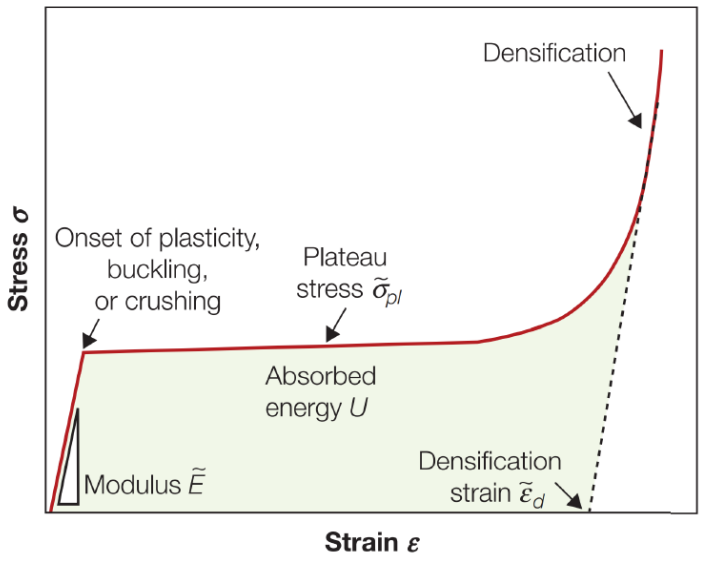


*Figure 4-4. Typical stress (σ) – strain (ε) curve for cellular structures, illustrating the three distinct regions and corresponding parameters [64].*

In the following tests, the emphasis will be on calculating the elastic modulus ($E_{latt}$) and the yield strength ($\sigma_{y,latt}$) of the BCC unit cell structure. These properties will be theoretically calculated using Gibson and Ashby's model for bending-dominated lattices, as detailed in equation (7) and (8). It is important to note that this model becomes invalid for high relative densities, specifically when $\rho_{rel}$ exceeds 0.3.

The parameters $C_1$, $C_2$, $n$, $m$, are specific to Gibson-Ashby's model and vary depending on whether the lattice structures are bending or stretching dominated [65], [66]. These parameters are known as the scaling pre-factors ($C_1$, $C_2$) and exponents ($n$, $m$) [48]. For our application, based on the literature, these parameters will be set to the following values: $n = 2$, $m = 1.5$, $C_1 = 1$, $C_2 = 0.3$ [48], [67].

$$\frac{E_{latt}}{E_s} = C_1(\rho_{rel})^n \quad (7)$$

$$\frac{\sigma_{y,latt}}{\sigma_{y,s}} = C_2(\rho_{rel})^m \quad (8)$$

To apply this model, it is essential to know the elastic modulus ($E_s$) and yield strength ($\sigma_{y,s}$) of the material beforehand. Since the specific aluminum alloy in question is still under development, standardized data for its properties are not yet available. However, preliminary tests conducted internally at the iMMC institute have provided approximate values based on experimental data: $E_s = 70GPa$ and $\sigma_{y,s} = 276\ MPa$.

### *4.3. LPBF PARAMETERS*

The LPBF machine available at the iMMC research institute is a ProX 200 DMP from 3D systems. It features a laser with a wavelength of 1070 nm and a maximum power of 273 W. The building chamber is maintained under an argon atmosphere with a controlled oxygen content (maximum 500 ppm) and has a maximal build volume of 140 mm x 140 mm x 100 mm.

The LPBF process is detailed in Section 2.2.2. After generating of the STL file from the CAD software, the file is converted into a .FAB3 file and uploaded to the machine. Before manufacturing, the building chamber is purged of oxygen via an argon flux. Upon manufacturing completion, the parts are separated from the build plate using electronic discharge machining (EDM).

As previously mentioned, a preliminary LPBF process was conducted to determine the optimal parameters for producing the best possible lattice structures. The dimensions of the lattice structures are provided in Table 4-2 (Specimens A and B), while the LPBF parameters used for the preliminary process run are shown on Table 4-3. The objective was to select various sets of parameters known to produce high quality parts, combined with a specific laser scan pattern tailored to the dimension of the lattice structure. The weld pool size was expected to be around 200 µm, which informed the selection of hatching space and offset parameters (refer to Figure 2-7). The offset parameter adjusts the laser's position to counteract the weld pool size.

The chosen laser scan pattern, referred to as "contour", traces the outline of the geometry. This is followed by concentric paths to completely fill the geometry (Figure 4-5). Given the small size of the structure itself and the melt pool, some deviation from the intended lattice structure dimensions is anticipated. This deviation was evaluated and taken into account for the manufacturing of specimens for further testing.

*Table 4-3.* The table outlines the LPBF process parameters related to the specified lattice structure design detailed in Table 4-2. The parameters listed here are specific to the preliminary LPBF process conducted to evaluate the machine's performance. For definitions of the parameters described in this table, refer to Figure 2-7.

| | SPECIMEN A | | | | SPECIMEN B | | | |
|---|---|---|---|---|---|---|---|---|
| **PARAMETERS ID** | 1 | 2 | 3 | 4 | 1 | 2 | 3 | 4 |
| **LASER POWER [%]** | 60 | 60 | 70 | 70 | 60 | 60 | 70 | 70 |
| **LASER SPEED [MM/S]** | 400 | 400 | 300 | 300 | 400 | 400 | 300 | 300 |
| **PRE-SINTERING** | Yes | No | Yes | No | Yes | No | Yes | No |
| **SCAN PATTERN** | Contour | Contour | Contour | Contour | Contour Concentric Circles | Contour/ Concentric Circles | Contour/ Concentric Circles | Contour/ Concentric Circles |
| **HATCHING SPACE [MM]** | - | - | - | - | 100 | 100 | 100 | 100 |
| **OFFSET [MM]** | 30 | 30 | 30 | 30 | 100 | 100 | 100 | 100 |
| **QUANTITY [PC]** | 1 | 1 | 1 | 1 | 1 | 1 | 1 | 1 |

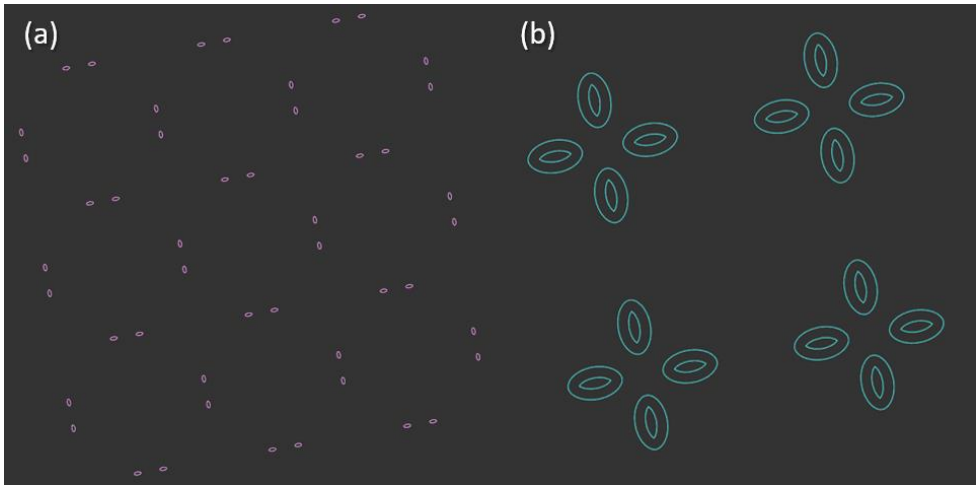


*Figure 4-5. Laser scan patterns for: (a) Specimen A and (b) Specimen B, lattice structures designs.*

Pre-sintering is a key parameter in the manufacturing process. This step involves sintering the powder at half of the intended power before the final laser scan at full power (powder melting). Pre-sintering has been shown to improve the quality of parts in terms of both dimension and surface finish.

The objective was to produce two sets of lattice structures with varying levels of beam porosity (internal porosity) while maintaining consistent lattice structure design (i.e., beam diameter and distance between unit cells) for subsequent testing. Based on the preliminary results detailed in Section 5.1, the lattice structure design was adjusted to match the selected LPBF parameters. Table 4-4 presents the final lattice structure design, the corresponding LPBF parameters, and the quantities of specimens produced.

*Table 4-4.* This table details the LPBF process parameters for the lattice structure designs detailed in Table 4-2. These parameters are specifically for the Specimens 1 and 2. For definitions of the parameters described in this table, refer to Figure 2-7.

| | **SPECIMEN 1** | **SPECIMEN 2** |
|---|---|---|
| **LASER POWER [%]** | 60 | 60 |
| **LASER SPEED [MM/S]** | 400 | 400 |
| **PRE-SINTERING** | Yes | No |
| **SCAN PATTERN** | Contour | Contour |
| **HATCHING SPACE [MM]** | - | - |
| **OFFSET [MM]** | 30 | 30 |
| **QUANTITY [PC]** | 25 | 25 |

### *4.4. MICRO CT (XCT) MORPHOLOGY CHARACTERIZATION*

CT imaging will be employed to characterize the manufactured specimens, with the aim of identifying and quantifying manufacturing defects such as porosity and dimensional deviations, and analyzing their impact on the structure's performance and quality. The test samples will be scanned at high resolution with a voxel size of 4 µm, to capture the complete width of the sample. For in-situ testing, parameters are selected to ensure high-quality images with minimal scan time, achieving a minimum voxel size of 8.5 µm. Section 2.4 discusses the rule of thumb regarding voxel size, which indicates that visible defects are three times the voxel size.

The X-ray CT parameters for imaging with a 4 µm voxel size are as follows:

- Source: 100kV, 40µA
- Detector: frame rate – 2, averaging frames – 5
- Filter: Aluminum disk, 1.2 mm thick
- Projections: 1440 images

The X-ray CT parameters for imaging with a 8.5 µm voxel size are as follows:

- Source: 120kV, 83µA
- Detector: frame rate – 12, averaging frames – 1
- Filter: none
- Projections:704 images

An aluminum filter was employed in the acquisition of 4 µm images to mitigate the beam hardening effect inherent in this set-up. Additionally, ring artifacts observed in CT imaging were mitigated by applying a ring filter during image reconstruction.

The in-situ testing set-up facilitates compression of lattice structures without the need for disassembly, enabling image acquisition for DVC analysis. Furthermore, the in-situ testing stage was utilized for sample compression and calculation of the global mechanical properties of the lattice structures (Section 4.5)

CT images are analyzed using Avizo software. The segmentation tool within the software was utilized to delineate the lattice structure from the surrounding air and internal porosity. This segmentation, coupled with analysis tools, enables calculation of internal porosity (beam porosity) and relative density (volume fraction) of the lattice structures.

Beam thickness of the structures was determined using CTAn software, that employs a sphere fitting algorithm to yield the thickness distribution within the provided structure. Further details will be provided in Section 5.

### *4.5. COMPRESSIVE TESTING*

The mechanical properties of the manufactured lattice structures were evaluated under compressive loading to determine their elastic modulus, compressive yield strength, and ultimate compressive strength. As previously mentioned, these compression tests were conducted in-situ to facilitate the acquisition of CT images during testing.

Three samples of Specimen 1 and one sample of Specimen 2 (see Table 4-2 and Table 4-4) were subjected to uniaxial compression to assess the aforementioned mechanical properties, as well as their deformation and failure modes. Due to the sample height, an aluminum plate was used to ensure proper compression. The procedure for performing the compression test to evaluate global mechanical properties is as follows:

- The structure is mounted inside the testing chamber with the jaws initially open.
- The bottom jaw is then closed at a speed of 1.3 $\frac{mm}{s}$ until the force reaches 10 N.
- Next, the bottom jaw continues to move at a speed of 0.5 $\frac{mm}{s}$ until the force reaches 20 N, ensuring the structure is securely positioned between the jaws.
- Subsequently, the bottom jaw is moved at a speed of 0.2 $\frac{mm}{s}$ until failure, defined as a significant drop in force. The compression data is acquired at 500 ms.

This procedure was also applied to data acquired for DVC analysis. After securing the structure, a scan was performed. The bottom jaw was then moved in 0.1 mm increments with a strain rate of 0.1 $\frac{mm}{s}$,with a scan taken after each movement. This is process was repeated until the structure failed.

Strain was calculated using the displacement of the bottom jaw and the height of the samples. Engineering stress for each sample was determined based on the applied compression load and the initial cross-sectional area, $A_{cs} = 25mm^2$. The experimental Young's modulus (Elastic Modulus) was derived from the elastic (linear) region of the engineering stress – strain curves. The experimental yield compressive strength was calculated by drawing a line parallel to the linear portion of the stress – strain curve, offset by a strain of 0.002.

### *4.6. HEALING HEAT TREATMENT (HHT)*

To evaluate the healing properties of the material used in manufacturing lattice structures, a HHT will be performed. All HHT procedures applied to the lattice structures are based on those defined by Gheysen et. al. [2]. Since the same magnesium content is used and same manufacturing process, similar behavior is anticipated.

Gheysen et al. identified two different HHT protocols depending on the healing mechanism. For diffusion-based healing, optimal conditions were found to be 400°C for 30 – 120 minutes. For liquid-assisted healing, a temperature of 540°C for 30 minutes was optimal [2]. Based on these findings, the following HHT protocols were used in this research:

- Diffusion Based Healing: 400°C for 30 minutes in an argon atmosphere with air cooling.
- Liquid Assisted Healing: 540°C for 30 minutes in an argon atmosphere with either air cooling or water quenching.

In Section 2.1, it was described that Gheysen et al. used a material composition of AlMg14 which is a different to the composition being used in this research. Nevertheless, because the magnesium content defines the quantity of eutectic phase and it is the same as for the material in use, similar behavior under HHT is expected.

# 5. RESULTS

## *5.1. PRELIMINARY LPBF PROCESS*

As previously mentioned, a preliminary LPBF manufacturing process was conducted to evaluate the machine's capability to achieve the desired lattice structure dimensions. The results from this preliminary process are presented below. Firstly, the CT images are displayed to illustrate the impact of four different sets of LPBF processing parameters on the same lattice structure design (specimen A and B).

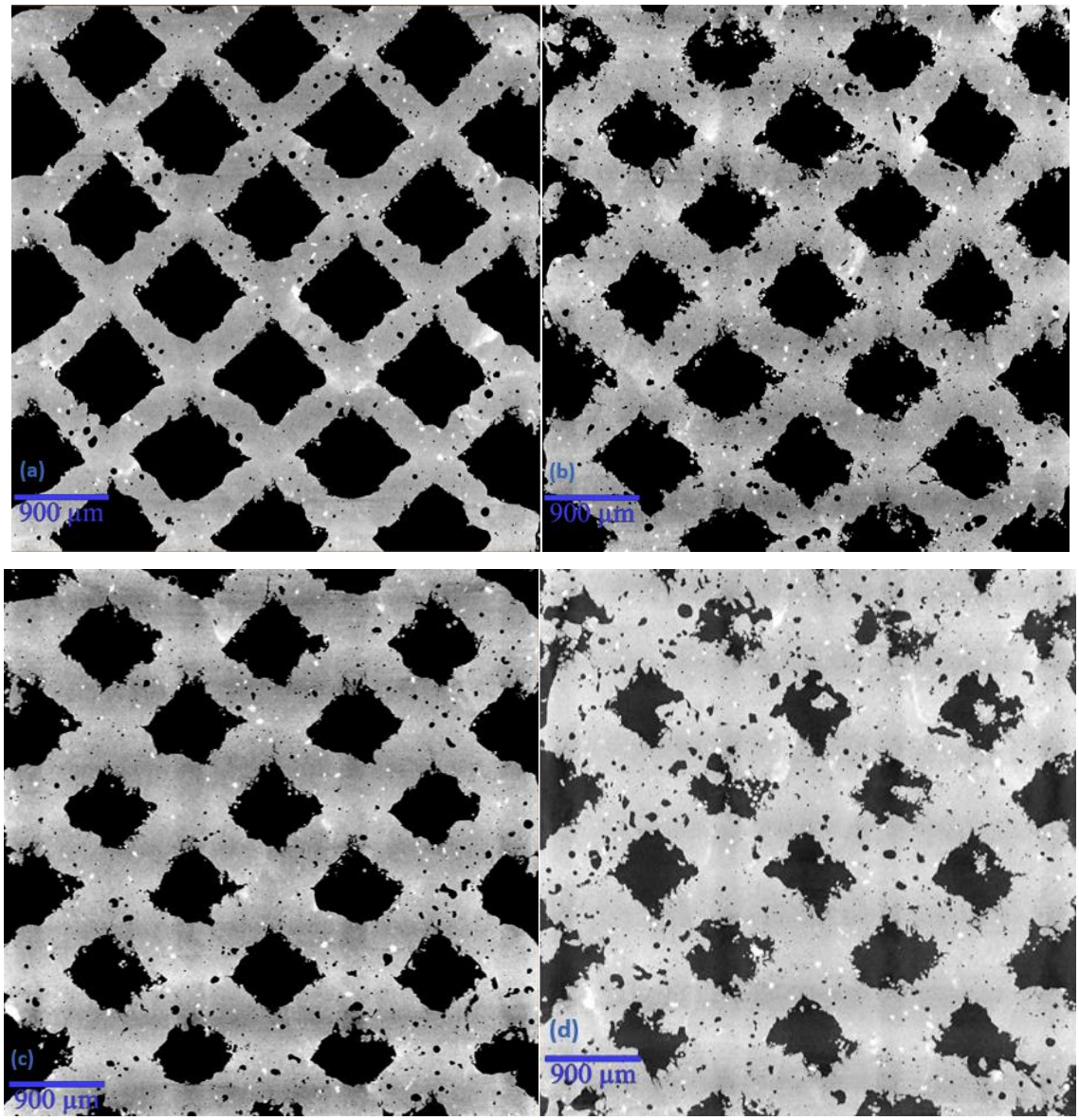


*Figure 5-1. CT images of the lattice structure design for Specimen A, illustrating: (a) LPBF parameter 1,60%,400mm/s,PS, (b) LPBF parameter 2,60%,400mm/s,NS, (c) LPBF parameter 3, 70%,300mm/s,PS, and (d) LPBF parameter 4, 70%,300mm/s,NS. Specimen A is designed with an intended beam diameter of 100 µm.*

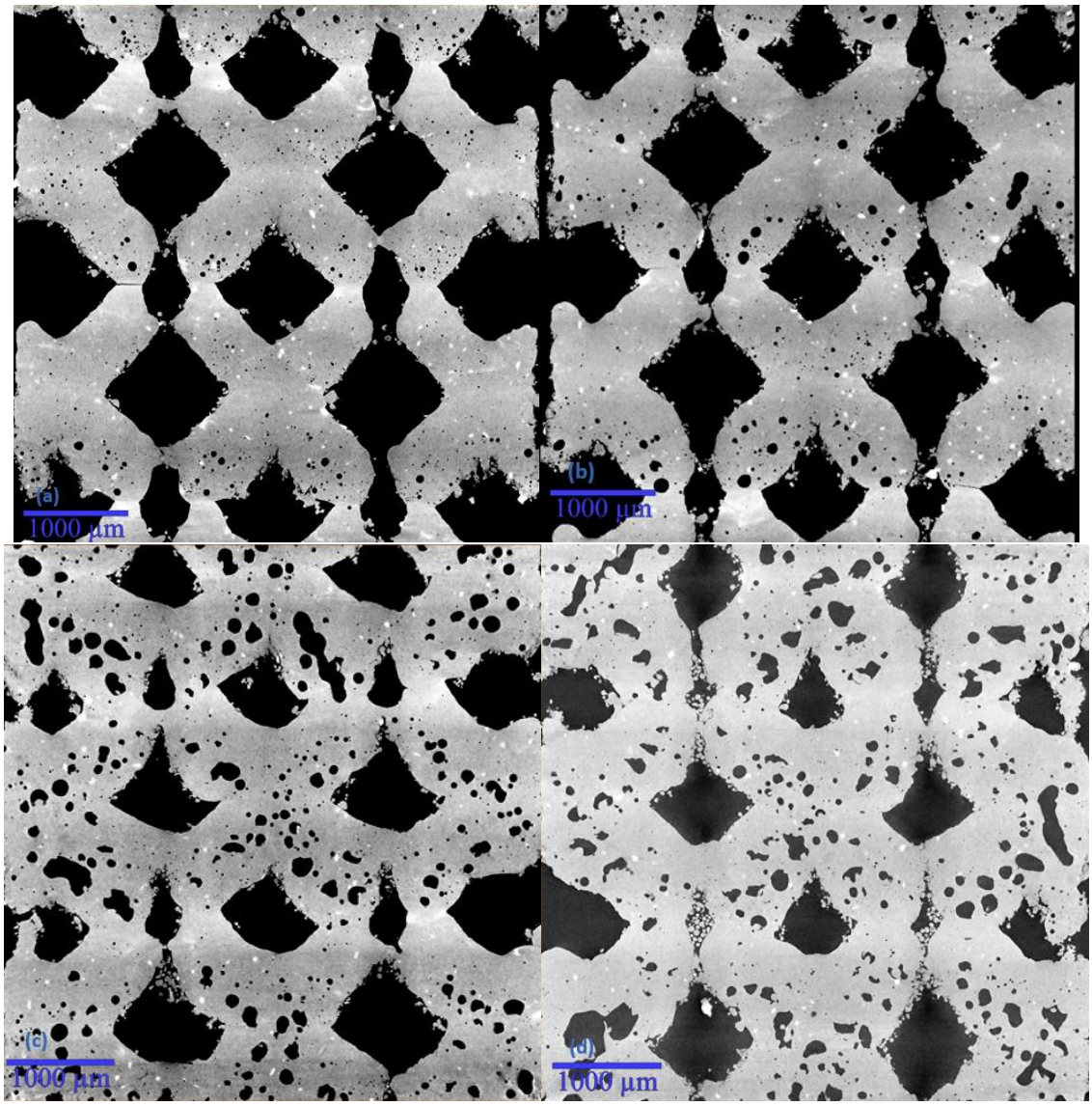


*Figure 5-2. CT images of the lattice structure design for Specimen B, illustrating: (a) LPBF parameter 1,60%,400mm/s,PS, (b) LPBF parameter 2,60%,400mm/s,NS, (c) LPBF parameter 3, 70%,300mm/s,PS, and (d) LPBF parameter 4, 70%,300mm/s,NS.. Specimen B is designed with and intended beam diameter of 500 µm.*

Figure 5-1 depicts the parts manufactured with Specimen A design, which features an intended beam diameter of 100 µm, a distance between unit cells of 1mm and an expected relative density of 1.6%. Figure 5-2 shows parts manufactured with Specimen B design, characterized by an intended beam diameter of 500 µm, a distance between unit cells of 1 mm and an expected relative density of 24.3%. Markers (a), (b), (c) and (d) correspond to CT images of the parts produced with parameters set 1, 2, 3, and 4, respectively. Further details on each parameter set can be found in Table 4-3.

The images in Figure 5-1 and Figure 5-2 reveal a tendency for internal beam porosity and beam diameter to vary with the processing parameters used. Processing parameters set 1 (60% laser power, 400 mm/s scan speed, Pre-sintering (PS)) result in the minimum internal porosity percentage and smaller beam diameter compared to the other sets. Additionally, defects such as voids within the structure and a small crack, observable in Figure 5-2 (a).

Based on the CT images, processing parameters sets 3 and 4, which combine a laser power of $70\%$ $(191.1W)$ and a laser scan velocity of $300\,\frac{mm}{s}$, do not yield good manufacturability for the material in question. Structures produced with these parameters exhibit a significant number of pores, which are larger in size and less spherical in shape (see Figure 5-2). Although their shape is non- spherical, these defects are suspected to be due to the keyhole mode induced by the high linear energy density resulting from the specified laser power and scan velocity, as will be discussed further in Section 6**Error! Reference source not found.**. In contrast, the combination o f laser power of $60\%$ $(163.8W)$ and a laser scan velocity of $400\,\frac{mm}{s}$ of parameter sets 1 and 2, exhibit better manufacturability. While these samples also contain porosities, they are fewer in number, smaller in size, and more spherical in shape.

In Figure 5-1, the difference in surface quality is evident between the processing parameters sets that include pre-sintering and those that do not. Furthermore, among the parts that incorporate pre-sintering, there is a slight decrease in porosity and, more importantly, a more accurate beam diameter. This behavior is further illustrated in subsequent graphs.

Measurements of the internal porosity and relative density of the specimens were conducted using Avizo software. This software enables filtering and segmentation of the CT images to distinguish the lattice structure from the air and internal porosities, as shown in Figure 5-3. The figure presents CT images from Figure 5-1 (a) and Figure 5-2 (a), clearly separating the internal porosities (in dark blue) from the structure (light blue) and the structure from the air (red).

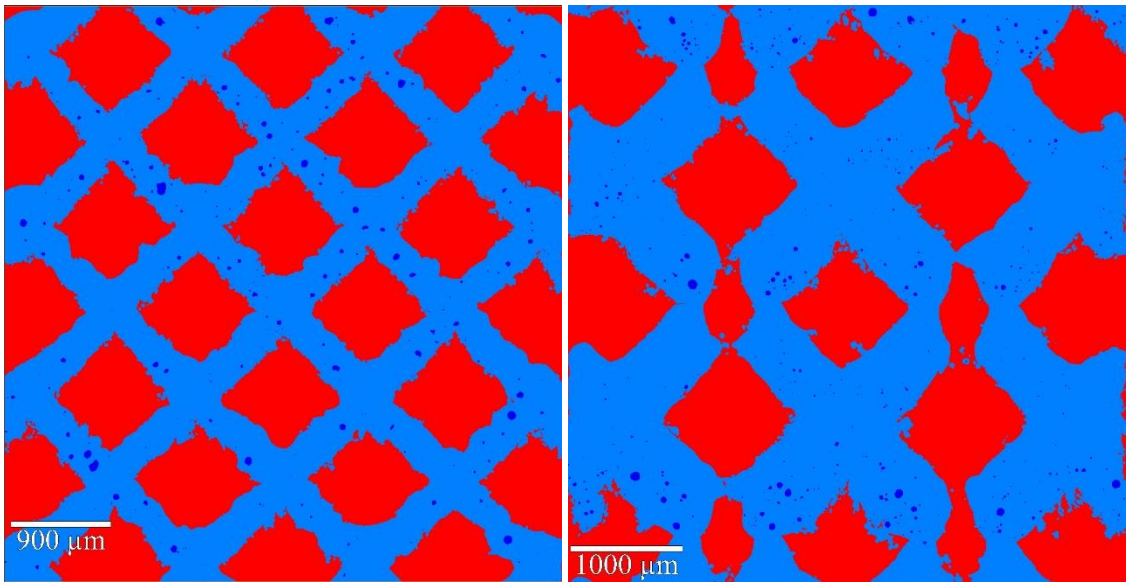


*Figure 5-3. CT image processing using Avizo software. The displayed images demonstrate the segmentation procedure within the software, enabling differentiation of the lattice structure from surrounding air and internal porosities within the structure. Lattice structures are depicted in light blue, internal porosities in dark blue, and surrounding air in red. Specimen A is shown on the left, and Specimen B is shown on the right.*

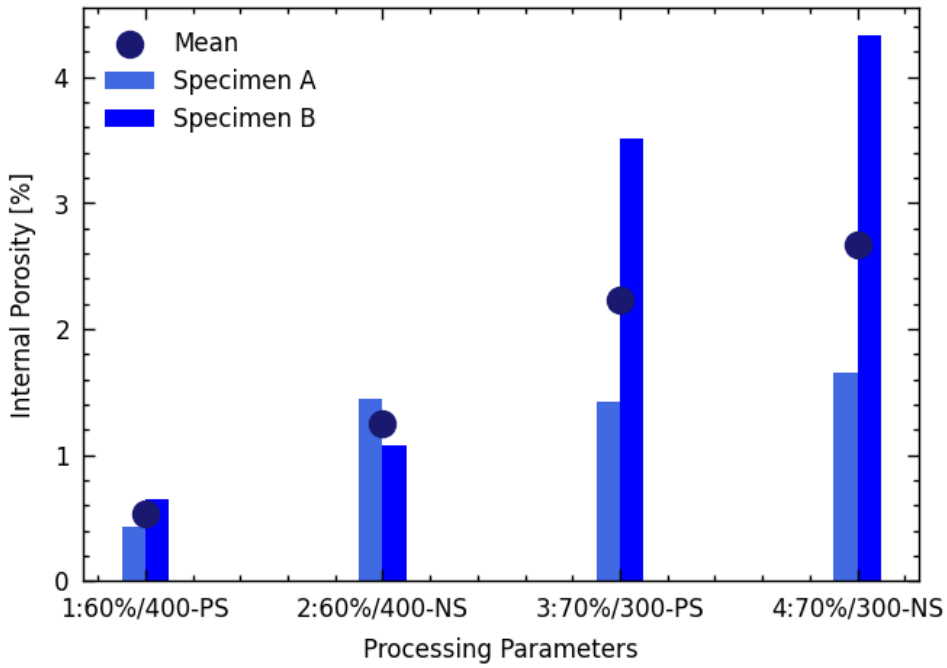


*Figure 5-4. The graph illustrates the internal porosity percentage for each set of LPBF processing parameters. Both specimens are considered for each parameter set. Mean values for each set are indicated with a circle. "PS" refers to Pre-sintering, and "NS" refers to No Pre-sintering. For further details on Specimen A and B, refer to Table 4-2.*

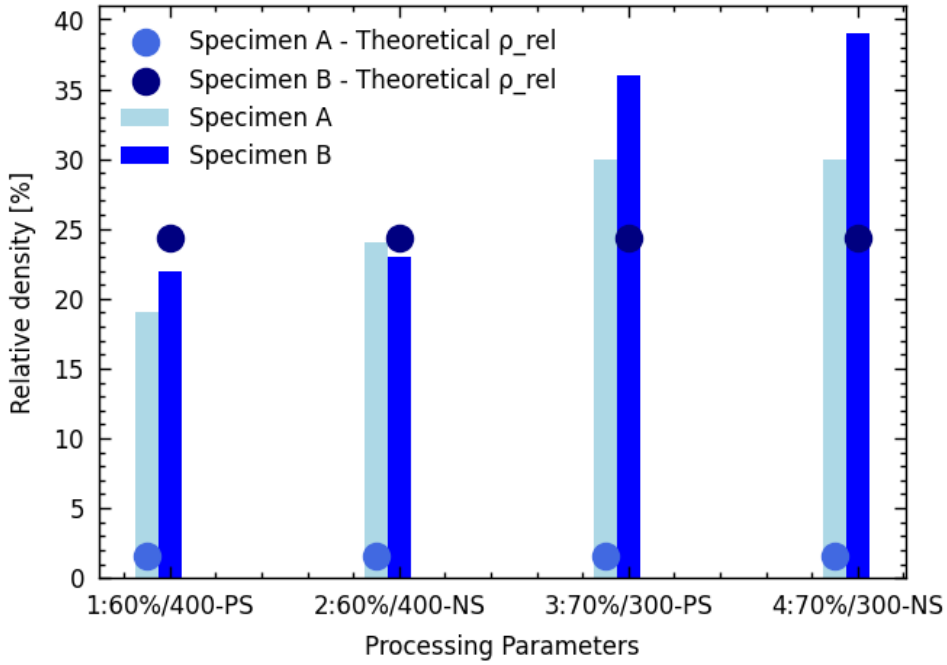


*Figure 5-5. The graph depicts the relative density percentage for each set of LPBF processing parameters, considering both specimens A and B. Theoretical values for relative density, calculated using the CAD model, are indicated with a circle. For further details on Specimen A and B, refer to Table 4-2.*

Figure 5-4 illustrates the relationship between processing parameters and the internal porosity percentage of the beam. Measurements from both Specimen A and Specimen B are included in the graph, along with the mean internal porosity achievable for each parameter set. The figure corroborates observations from the CT images of Specimens A and B shown in Figure 5-1 and Figure 5-2. There is a clear trend indicating that the minimum achievable internal porosity percentage corresponds to processing parameters set 1.

Moreover, Figure 5-5 presents the measured relative density (actual) of Specimens A and B in relation to the processing parameter set used. The theoretical relative densities (as shown in Table 4-2) are also depicted for comparison. The trend observed in internal porosity is reflected in Figure 5-5, albeit with less pronounced impact. Nevertheless, parameter set 1 appears to produce a relative density closest to the desired lattice structure, although a noticeable shift exists between the expected and achieved relative densities.

Another critical parameter for assessing process performance is the actual beam diameter compared to the intended diameter. CTAn software was employed to measure this, utilizing a

sphere fitting algorithm to provide a thickness distribution of the structures, as discussed in Section 4.4. Figure 5-6 illustrates the application of this algorithm to Specimen A (left) and Specimen B (right). The different colors represent variations in beam thickness (diameter). Note the change in color when approaching the intersection of the beams, indicating a larger area.

The attained beam diameters for each parameter set are depicted in Figure 5-7, demonstrating their efficacy in realizing the intended specimen design. Figure 5-7 plots the actual beam diameter of Specimens A and B against the corresponding parameter set used, alongside the intended values. Remarkably, parameter sets 1 and 2 approximate the closest the intended design value for both specimens. Furthermore, it is discernible that the deviation between Specimen A and the intended design value is more pronounced compared to that of Specimen B.

Figure 5-8 and Figure 5-9 display the beam diameter distributions for Specimens A and B, respectively, in relation to the parameters sets utilized. The curve depicted in each plot represents the calculated distribution of the data. Across all distributions, two peaks are observed, as anticipated due to the increased area at the intersection of the beams. Hence, the first peak within this distribution signifies the actual beam diameter. Each distribution closely approximates the real beam diameter of the manufactured part, with values extracted from them utilized in the construction of Figure 5-7.

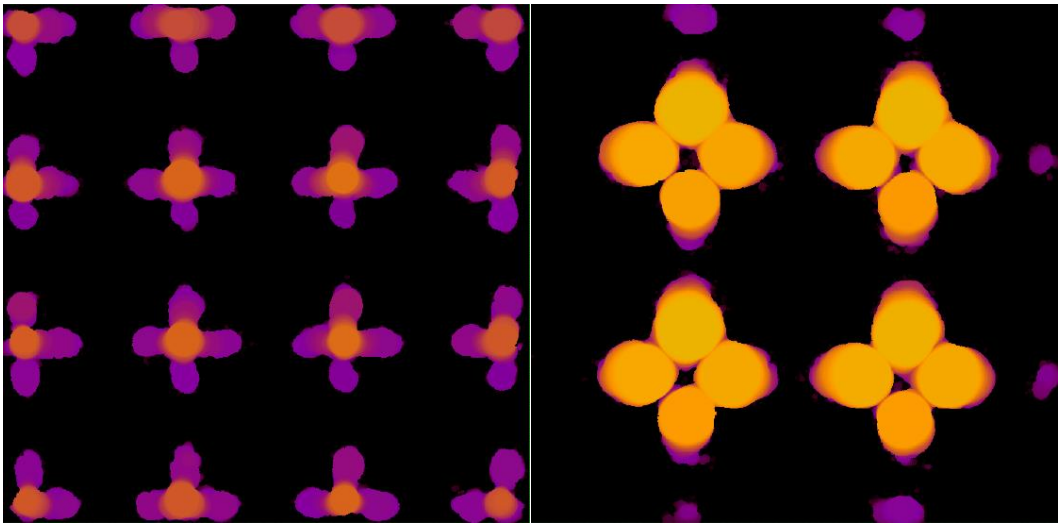

*Figure 5-6. The image demonstrates the methodology employed by the software to fit spheres within the structure, thereby estimating its actual beam diameter. Specimen A is depicted on the left, and Specimen B is shown on the right.*

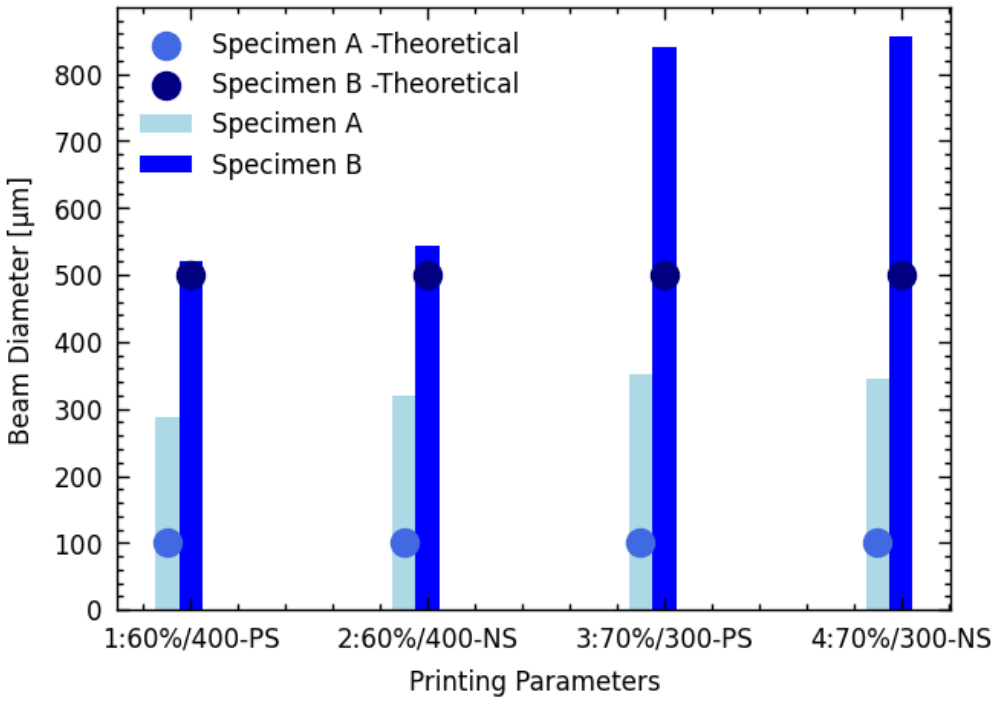


*Figure 5-7. The graph illustrates the achieved beam diameter against the intended value for the four different LPBF parameter sets. Both specimens are shown on the graph. The theoretical beam diameter values are represented with a circle.*

The goal is to have two different sets of processing parameter that yield beam diameters as similar as possible, with a preference for the smallest possible beam diameter. Based on the results from Figure 5-7, Figure 5-8, and Figure 5-9, it was decided to use only the processing parameters sets 1 and 2 for the manufacturing of the final samples. This means using 60% laser power (163.8 W) and a laser scan velocity of 400 $\frac{\text{mm}}{\text{s}}$, with pre-sintering (set 1) or without (set 2).

A decision was made to retain the design of Specimen A using set 2 of processing parameters (no pre-sintering). This choice was influenced by the observation that, compared to set 1, set 2 resulted in a larger deviation from the intended beam diameter. Referring to Figure 5-8 and considering the performance of Specimen A with parameter set 2, the desired beam diameter is determined to be 300 µm.

Furthermore, the design of Specimen A will undergo adaptation to create a secondary design. The objective is to achieve a real beam diameter similar to the target value of 300 µm using set 1 of processing parameters, which includes pre-sintering.

The adjusted final design of Specimen A is detailed in Table 4-2. The new designs are named Specimen 1 and Specimen 2, with the specified processing parameters for each shown in Table 4-4. The adjustment between designs was approximated to be around $50\mu m$ based on the real beam diameter distributions (Figure 5-8 and Figure 5-9).

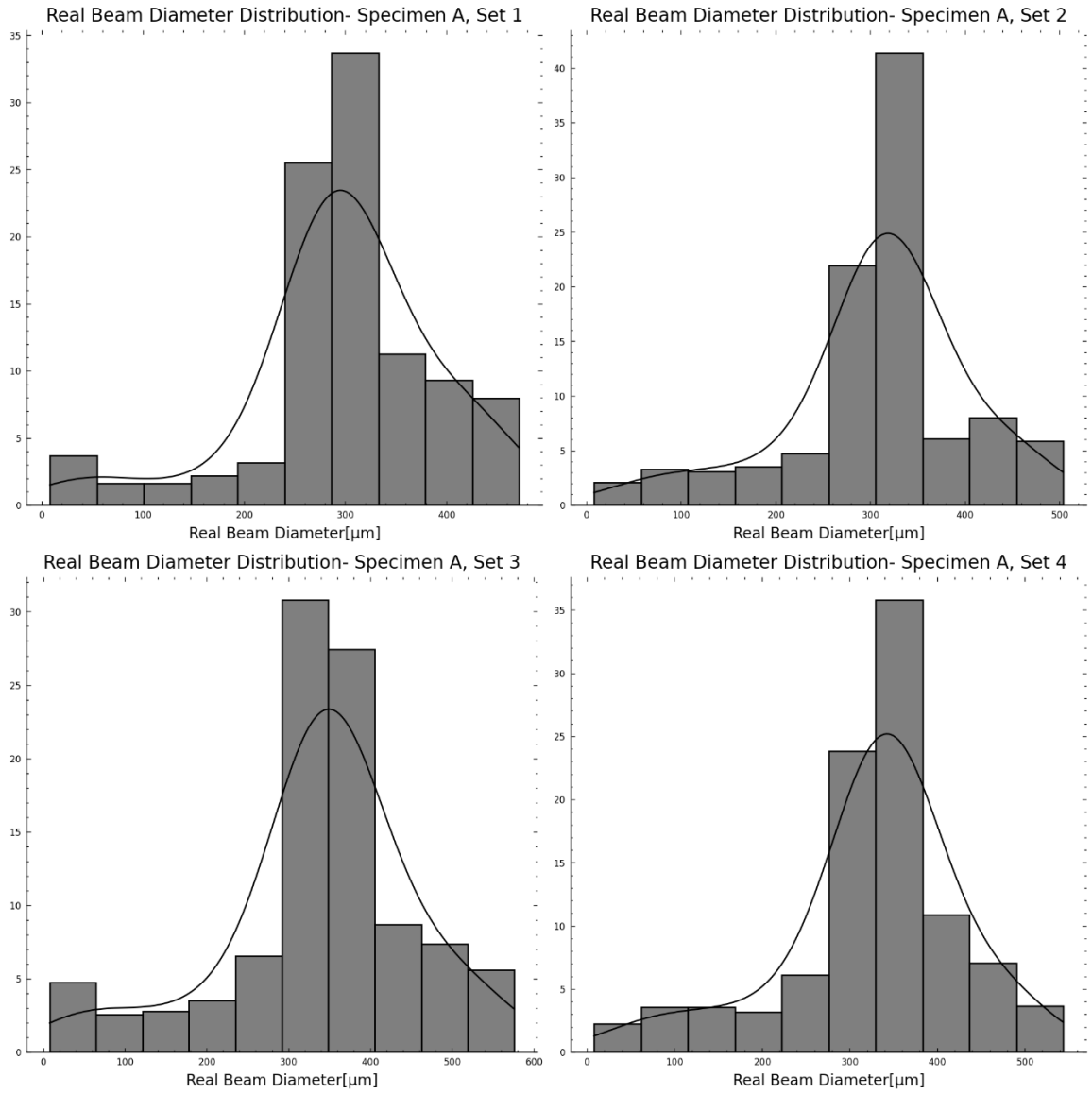


*Figure 5-8. The above distributions, derived from the CTAn software, represent the measured beam diameters the lattice structure design of Specimen A. For further details on Specimen A refer to Table 4-2.*

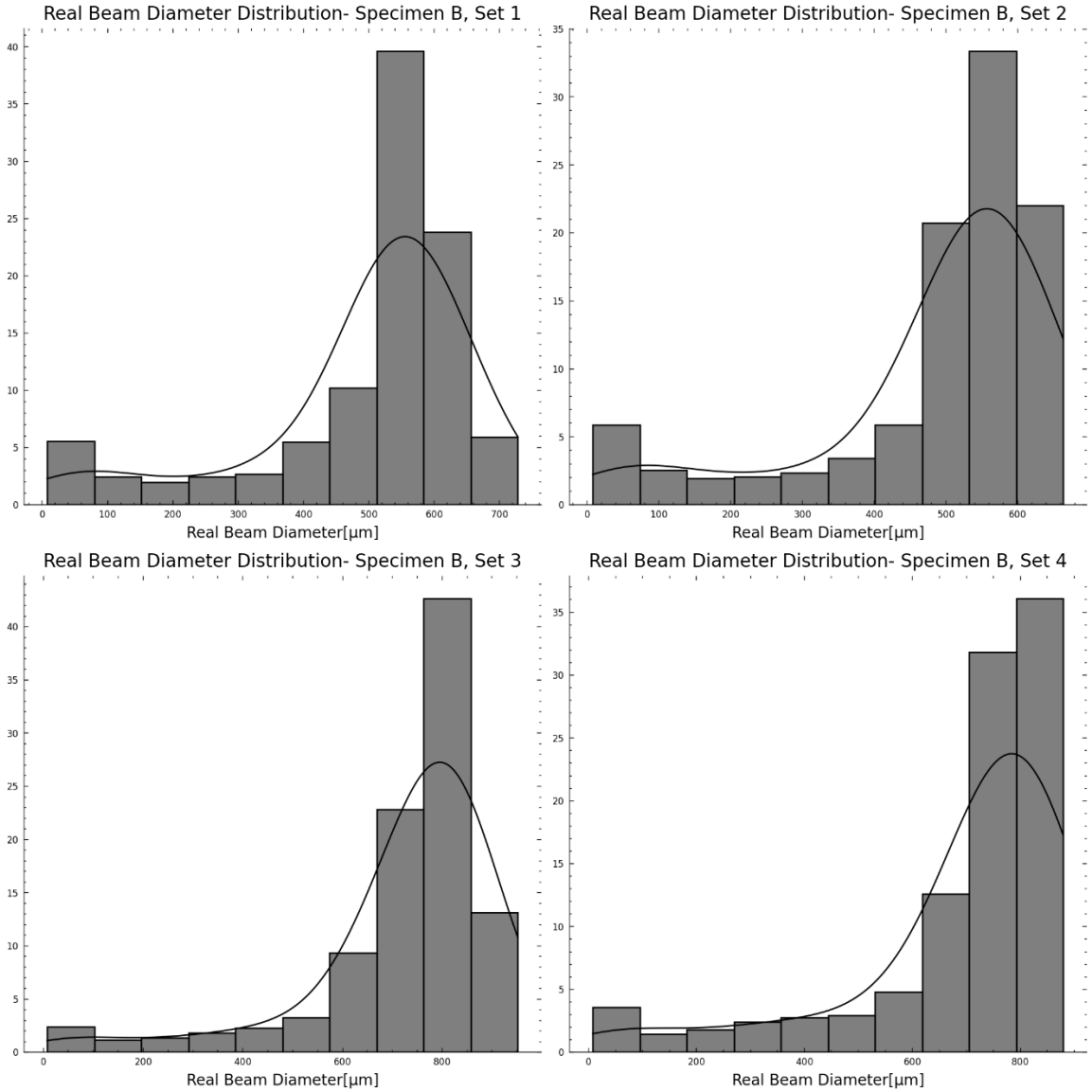


*Figure 5-9. The above distributions, derived from the CTAn software, represent the measured beam diameters the lattice structure design of Specimen B. For further details on Specimen B refer to Table 4-2.*

### *5.2. MORPHOLOGY CHARACTERIZATION*

The resulting morphology characterization of the lattice structures, manufactured with the parameters detailed in Table 4-4, is presented below. The analysis covers the overall internal porosity, relative density and beam diameter for each of the two lattice structure designs. To complete this analysis, six parts of each design were scanned, and the resulting CT images were analyzed in the same manner as the preliminary LPBF processed parts. The x-ray tomography settings used are for 4 µm voxel size, further details in Section 4.4.

CT images of different planes are presented in Figure 5-10 for Specimen 1 and Figure 5-11 for Specimen 2. Specimen 1 features a designed beam diameter of 150 µm with a 1 mm distance between unit cells, while Specimen 2 has a designed beam diameter of 100 µm with the same unit cells spacing. Markers (a), (b), and (c) denote the three different planes: xy, xz and yz, respectively. All orthogonal slices shown are taken from the middle of the volume. These images illustrate the overall shape and internal porosity of the structures.

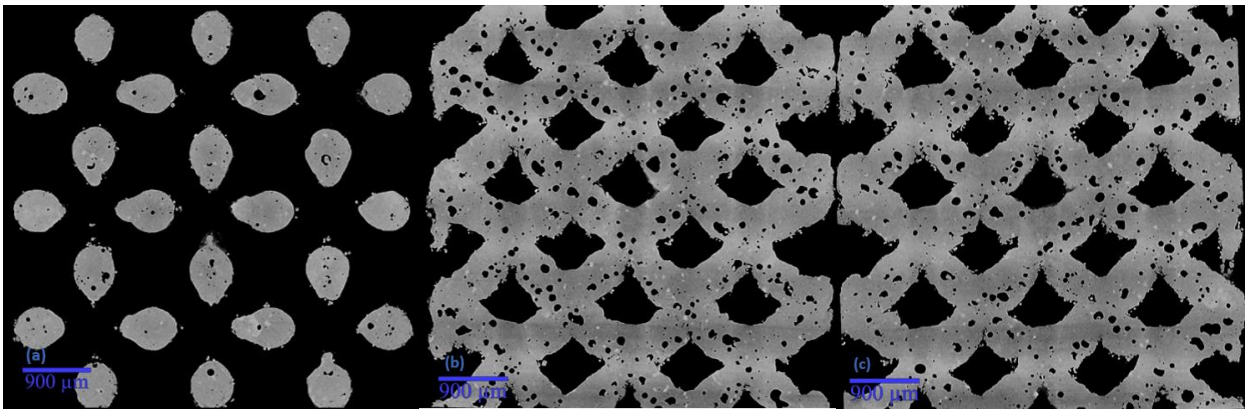


*Figure 5-10. CT images of the lattice structure design for Specimen 1: (a) xy plane, (b) xz plane, (c) yz plane. Specimen 1 has an intended beam diameter of 150 µm and was manufactured with 60% laser power, 400 mm/s and PS. For additional details on Specimen 1, refer to Table 4-2 ,and for LPBF parameters, refer to Table 4-4.*

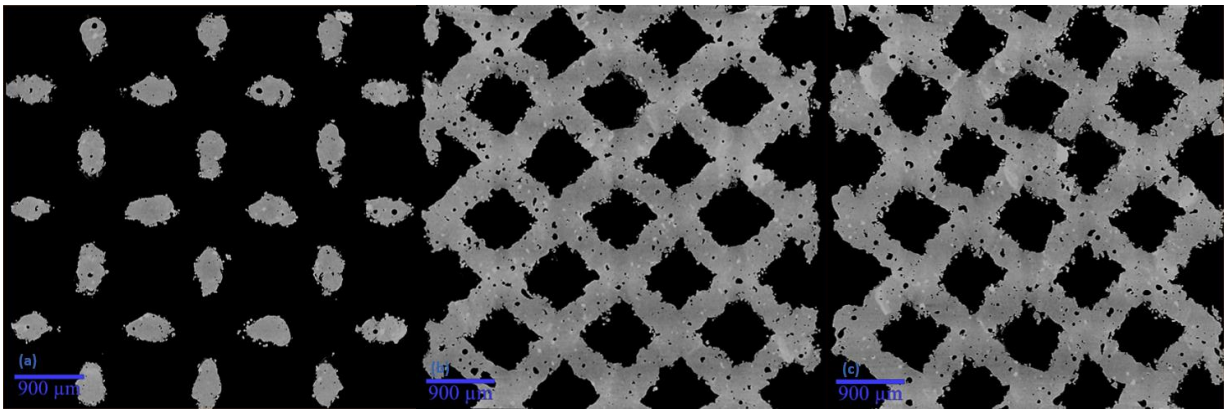


*Figure 5-11. CT images of the lattice structure design for Specimen 2: (a) xy plane, (b) xz plane, (c) yz plane. Specimen 2 has an intended beam diameter of 100 µm and was manufactured with 60% laser power, 400 mm/s and NS. For additional details on Specimen 2, refer to Table 4-2 ,and for LPBF parameters, refer to Table 4-4.*

Based on Figure 5-10 and Figure 5-11, it is evident that Specimen 1 differs from Specimen 2. Specifically, Specimen 1 exhibits larger beam diameters and more pronounced internal porosity. Additionally, Specimen 2 demonstrated the expected performance based on preliminary LPBF results, with its CT images resembling those of the structure with the same design and processing parameters (Figure 5-1, (b)). In contrast, Specimen 1 did not perform as anticipated, showing a clear discrepancy in beam diameter between the two manufactured structures, contrary to the objective. Furthermore, despite the use of density-optimized processing parameters for Specimen 1, it displayed higher internal porosity than Specimen 2, highlighting that while Specimen 2 met expectations, Specimen 1 did not.

The overall morphology of the structures is as expected, with fairly cylindrical beams and minor material pooling at the bottom of beam intersections, attributable to gravity and the building direction within the powder chamber, bottom-to-top for all the CT images shown (excluding xy plane view). However, some nodes (beam intersections) have sharp edges that could cause stress concentrations. This aspect will be further examined through compression testing and subsequent DVC analysis (Section 5.4). Additionally, it is important to note that the surface quality of Specimen 2 is inferior to that of Specimen 1 (see Figure 5-10 and Figure 5-11). This was also observed in the parts manufactured during preliminary processing, where the pre-sintering step visibly improved surface roughness.

Based on the CT images, Specimen 2 appears to outperformance Specimen 1. However, a closer examination of the images in Figure 5-11 (Specimen 2) reveals a crack in one of the beams in the yz slice. Figure 5-12, provides detailed CT images of the observed crack location. Markers (a), (b), and (c) show the views from xy, xz, and yz plane, respectively, while marker (d) presents a three-dimensional (3D) rendering of the structure area containing the defect.

Figure 5-12 (d), confirms that this crack is indeed a void of considerable size. The absence of powder in the region suggests that the issue is not due to lack of fusion but rather an unknown factor. The xy slice (Figure 5-12 (a)) at the same location shows a missing segment with remnants of a different material, a pattern also observed in the xz slice (Figure 5-12 (b)).

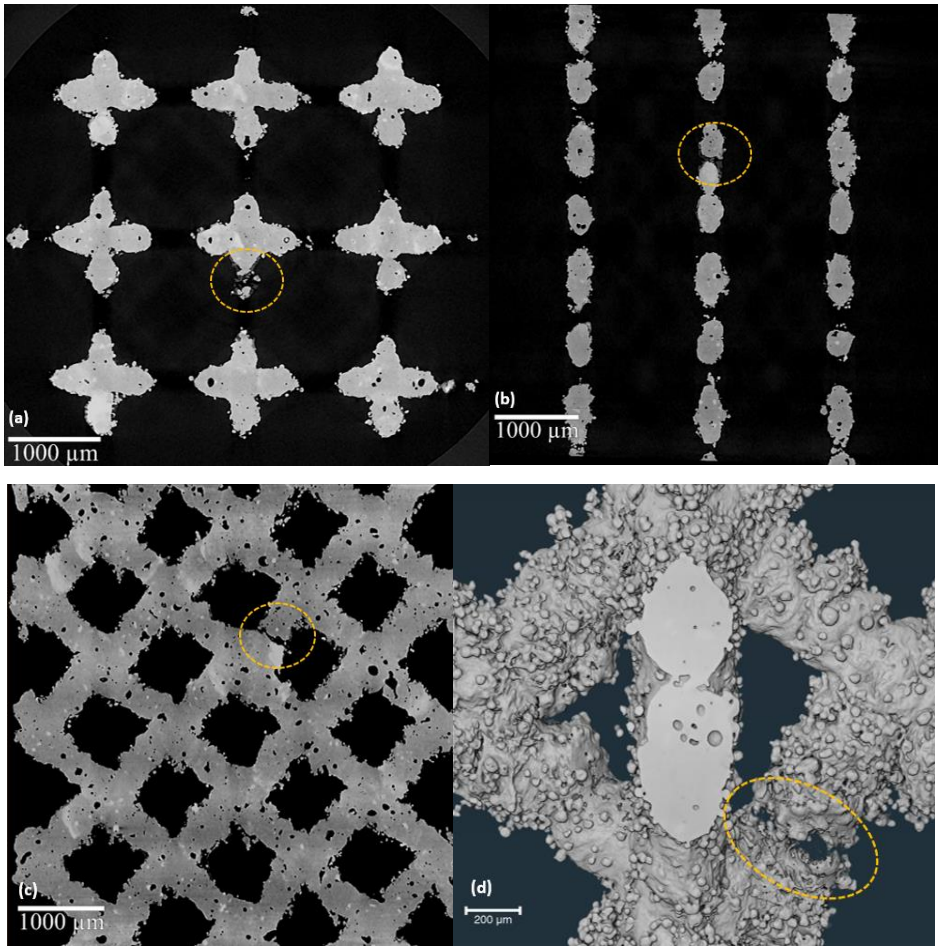


*Figure 5-12. CT images of the lattice structure design for Specimen 2 in the zone of the observed damage: (a) xy plane, (b) xz plane, (c) yz plane, (d) damaged sub volume. Specimen 2 has an intended beam diameter of 100 µm. For additional details on Specimen 2, refer to Table 4-2 ,and for LPBF parameters, refer to Table 4-4.*

Figure 5-13 shows the 3D rendering of another sample of Specimen 2 exhibiting the same defect shown in Figure 5-12. This phenomenon is not observed in Specimen 1, suggesting that it is specific to the parts manufactured with the design and processing parameters of Specimen 2. A more detailed discussion of this behavior will be provided in Section 6.

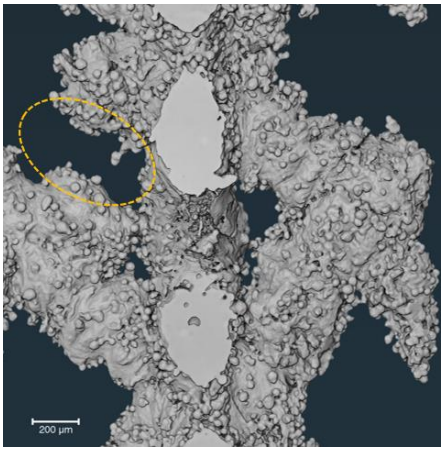


*Figure 5-13. Volume rendering of the damaged sub volume of Specimen 2, sample 2. The visible view is from the yz plane. For additional details on Specimen 2, refer to Table 4-2 ,and for LPBF parameters, refer to Table 4-4.*

Figure 5-14 presents a box plot of the measured internal porosities for each set of processing parameters. A boxplot illustrates the dataset's distribution: the box represents the interquartile range (IQR), which contains the middle 50% of the data, while the whiskers (lines extending from the box) represent data points within 1.5 times the IQR in both directions. Additionally, Figure 5-14 includes a marker indicating the mean value of each dataset.

Specimen 1 corresponds to the processing parameters PS-60%-400mm/s, where PS denotes the pre-sintering step, 60% is the laser power, and 400mm/s the laser scan velocity. Similarly, Specimen 2 corresponds to the processing parameters NS-60%-400mm/s. The figure corroborates observations from the CT images: Specimen 1 has a higher internal porosity than Specimen 2. Additionally, the variation in measurements is lower for Specimen 2. Given that the measurements were performed similarly for both specimens, it is suspected that the variation is indicative of the specimen's performance. The calculated mean values for each data set are as follows:

- PS 60% 400mm/s (Specimen 1) – Mean Internal Porosity 2.25 % of structure volume
- NS 60% 400mm/s (Specimen 2) – Mean Internal Porosity 1.43 % of structure volume

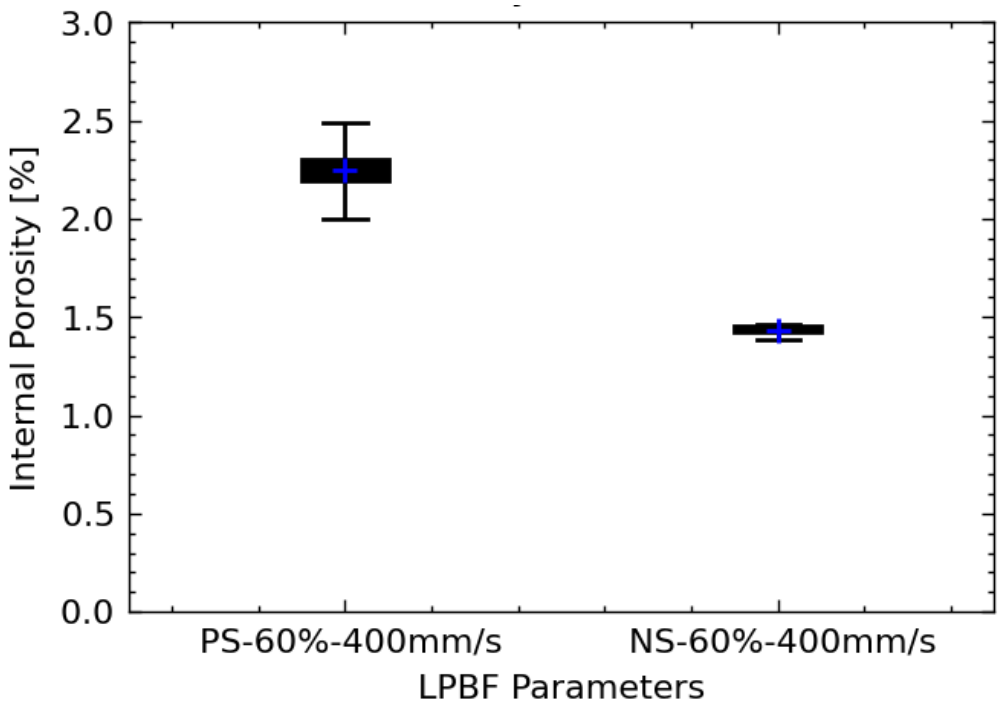


*Figure 5-14. Box plot illustrating the measured internal porosities for the two different lattice structure designs (Specimen 1 and 2) with their respective processing parameters. For additional details on the lattice structure designs, refer to Table 4-2, and for LPBF processing parameters, refer to Table 4-4.*

The mean internal porosity calculated for each parameter set during the preliminary LPBF printing shows that parameter set 1 (PS-60%-400mm/s) exhibited a mean internal porosity of 0.53%, while parameter set 2 (NS-60%-400mm/s) exhibited a mean of 1.25%. This further corroborates that Specimen 1 deviates significantly from the expected behavior by presenting nearly five times (4.24 times exactly) more internal porosity. In contrast, Specimen 2 only deviated by 0.18%, a difference that could be attributed to measurement errors.

To determine the origin of the observed porosity, it is essential to analyze their size and shape. An analysis of the equivalent diameter and sphericity of the internal porosities was conducted. Figure 5-15 and Figure 5-16 plot these values, respectively. The histograms of equivalent diameters are shown in Figure 5-15, with calculations performed by the Avizo software using the formula, $\emptyset_{eq} = \frac{2*Area}{\pi}$. Different colors in the graph represent different samples of the same specimen. As mention at the beginning of this section, six samples from each specimen were characterized to evaluate the performance of each design. The top graph in Figure 5-15 shows the results for Specimen 1, and the bottom graph shows the results for

Specimen 2, as indicated by their titles. Note that the histogram uses a logarithmic scale and the equivalent diameters are presented in micrometers (µm). The porosities were filtered to exclude the three smallest measured volumes (64, 128 and 192µm$^3$) to adhere to the rule of thumb described in Section 2.4.

Based on the histogram of the equivalent diameter measurements, both specimens exhibit a positively skewed distribution. Specimen 1 appears more consistent regarding measurement variability and has an overall higher count of pores. However, both Specimen 1 and Specimen 2 have the majority of their porosities below the equivalent diameter of 20 µm. In Specimen 2, sample number 6 deviates significantly from the other five samples, indicating a particular phenomenon in that sample, although no specific defect was found within the structure after the thorough analysis.

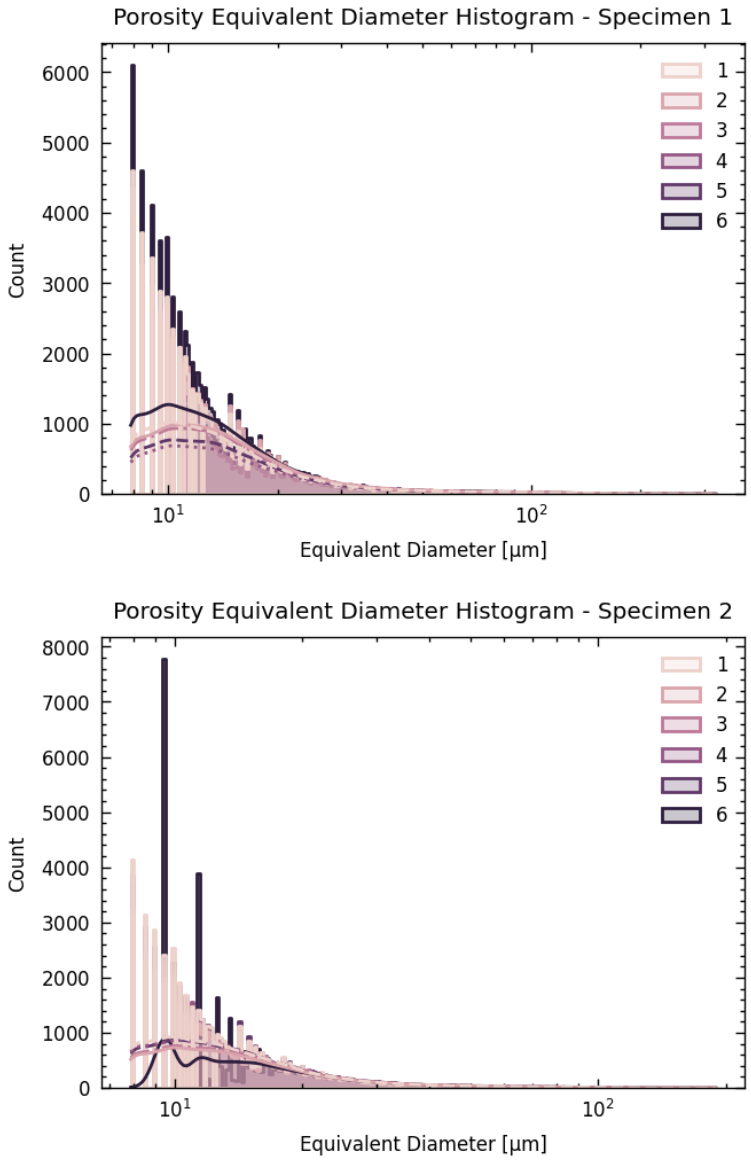


*Figure 5-15. Histograms depicting the measured equivalent diameter of internal porosities for two distinct lattice structure designs: Specimen 1 (top) and Specimen 2 (bottom). Additional details on lattice structure designs can be found in Table 4-2.*

Figure 5-16 displays the histograms of the sphericity values for the porosities of both specimens. Sphericity, a parameter that determines how spherical an object is, was calculated by Avizo software using the formula $Sphericity\ (\psi) = \frac{\sqrt[3]{36*\pi*V^2}}{A}$, where V is the volume of the porosity and A the area. Sphericity values are expected to range between 0 and 1, with values closer to 1 indicating a more spherical shape. The values in Figure 5-16 are from the filtered porosity data, excluding the three smallest volumes as explained above. Similar to Figure 5-15,

different colors represent different samples of the same specimen. The top plot shows the sphericity of Specimen 1 porosities, and the bottom plot for Specimen 2. Sphericity, by definition, is unitless.

Most sphericity values exceed 0.8, indicating a fairly spherical shape. Although sphericity values are expected to range between 0 and 1, Figure 5-16 shows values above 1, likely due resolution and software measurement errors, which have a bigger impact with smaller particles. These values are retained in the graph because the majority of the porosities are small, representing a significant portion of the data. The sphericity value is indicative of the origin of the porosity.

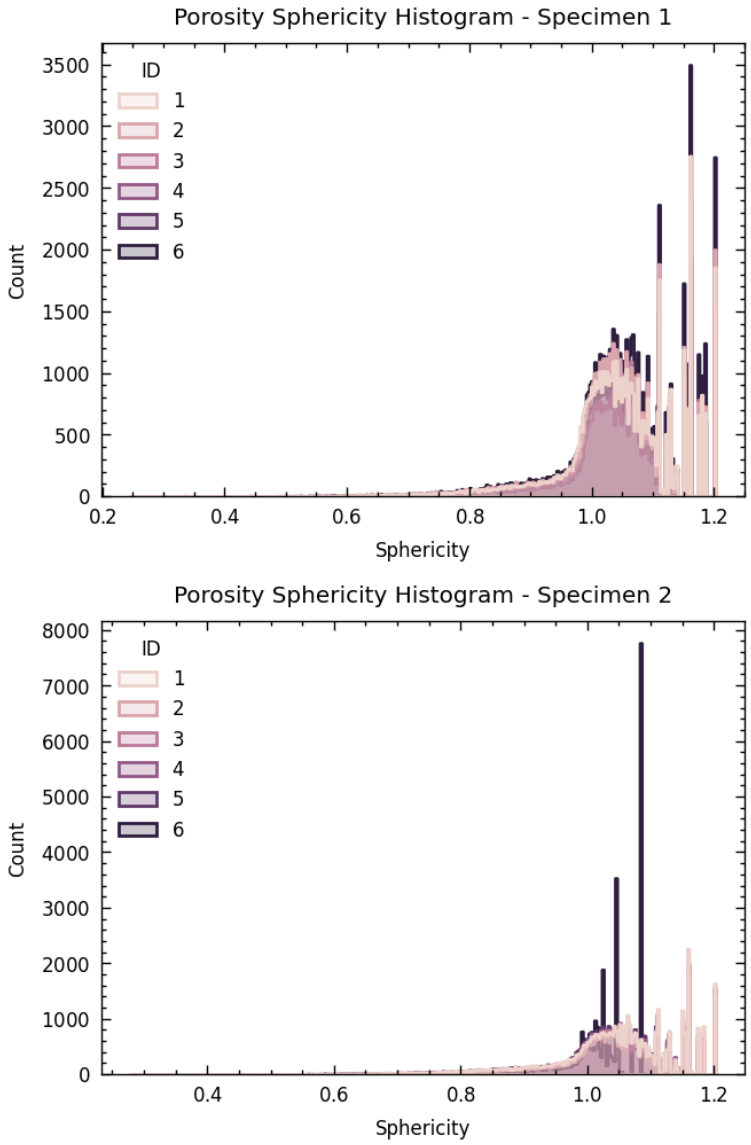


*Figure 5-16. Histograms depicting the measured sphericity of internal porosities for two distinct lattice structure designs: Specimen 1 (left) and Specimen 2 (right). Additional details on lattice structure designs can be found in Table 4-2.*

Figure 5-17 plots sphericity values against roundness values, highlighting the expected form and its impact on the shape of the particles. It is noticeable from this figure that a sphericity value above 0.7 is indicative of a fairly spherical shape.

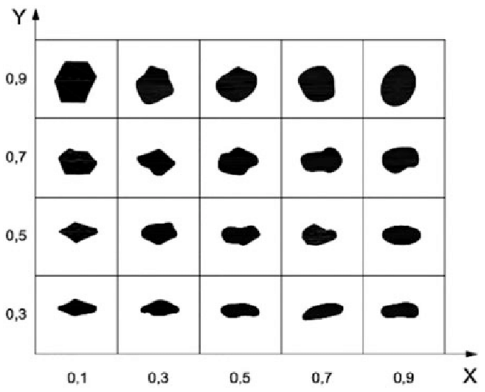


*Figure 5-17. Visual estimation of sphericity in the vertical axis (Y) and roundness on the horizontal axis (X). Image taken from Kamel et. al. research paper [68].*

A boxplot was generated for the calculated relative density values of the final parts, as shown in Figure 5-18. This plot illustrates the relationship between the achieved relative density, the processing parameters used, and the designs. Specimen 1 used parameters PS-60%-400mm/s, while Specimen 2 used parameters NS-60%-400mm/s. The mean value for each processing parameter is indicated by a blue cross in the figure. The values are as follows:

- PS 60% 400mm/s (Specimen 1) – Mean Real Relative Density ($\rho_{rel}$) 27.1 %
- NS 60% 400mm/s (Specimen 2) – Mean Real Relative Density ($\rho_{rel}$) 16.2 %

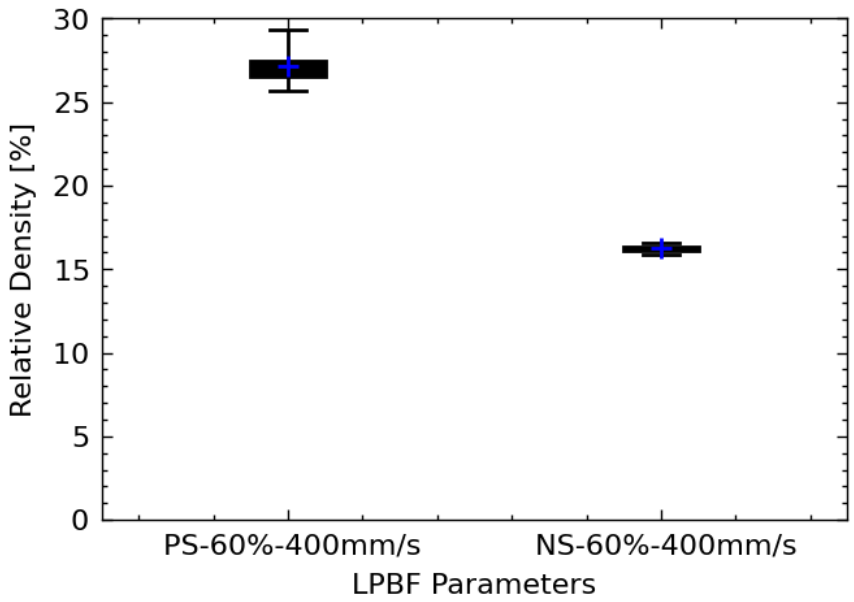


*Figure 5-18. Box plot illustrating the measured relative density for the two different lattice structure designs (Specimen 1 and 2) with their respective processing parameters. For additional details on the lattice structure designs, refer to Table 4-2, and for LPBF processing parameters, refer to Table 4-4.*

The behavior of each specimen in Figure 5-18 mirrors that observed in the internal porosity plot. Specimen 1 exhibits a higher relative density than Specimen 2, and Specimen 2 demonstrates lower variability compared to Specimen 1. Comparing the archived results with the designed values for relative density, Specimen 1 ($\rho_{rel} = 3.3\%$) and Specimen 2 ($\rho_{rel} = 1.6\%$) show an apparent extreme difference with the indicated mean values. However, considering that the expected beam diameter of 300 µm should in a relative density of around 9.2%, and taking into account the geometric changes experienced by the parts, the increment in value is not surprising. Therefore, quantifying the geometric changes undergone by the structure is imperative.

Starting with a boxplot of the evaluated the real beam thickness for each structure design, as shown in Figure 5-19. The plot depicts the achieved beam diameter for each processing parameter used and consequently for each specimen. Specimen 1 utilized parameters PS-60%-400mm/s and Specimen 2 NS-60%-400mm/s. The mean values are indicated within the plot by blue crosses. The mean values are as follows:

- PS 60% 400mm/s (Specimen 1) – Mean Real Beam Diameter (Ø) $452.5\mu m$
- NS 60% 400mm/s (Specimen 2) – Mean Real Beam Diameter (Ø) $294.6\mu m$

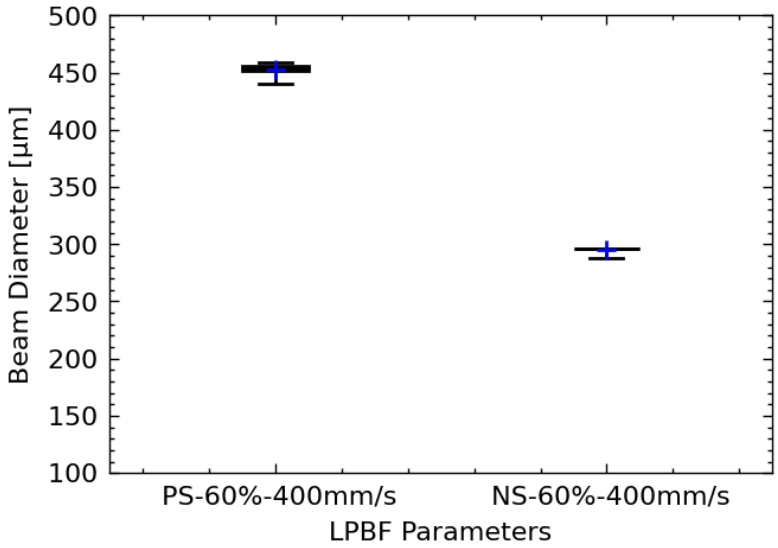


*Figure 5-19. Box plot illustrating the measured real beam diameter for the two different lattice structure designs (Specimen 1 and 2) with their respective processing parameters. For additional details on the lattice structure designs, refer to Table 4-2, and for LPBF processing parameters, refer to Table 4-4.*

Figure 5-19 highlights the deviation from the intended beam diameter and the disparity between the two designs. The design of Specimen 1 (left) exhibits a greater variation within the manufactured parts, as well as from the intended beam diameter value of 300 µm, compared with Specimen 2. Conversely, Specimen 2 demonstrates the expected results based on the preliminary LPBF process results and exhibits a smaller variation within the manufactured parts, which is preferable.

To complete the assessment of the final geometry of the manufactured lattice structures, the separation of the structure was measured using CTAn software. Similar to the measurement of the beam thickness, the software employs a sphere-fitting algorithm to determine the separation of the structure. This method is particularly effective for lattice structures because the calculated structure separation represents the distance between unit cells, illustrated in Figure 4-2. Figure 5-20 demonstrates the algorithm in action for both specimens, with different colors indicating various sphere sizes. The software provides the distribution of the structure separation along with the mean value. This mean value will be considered the real distance between unit cells of the manufactured parts.

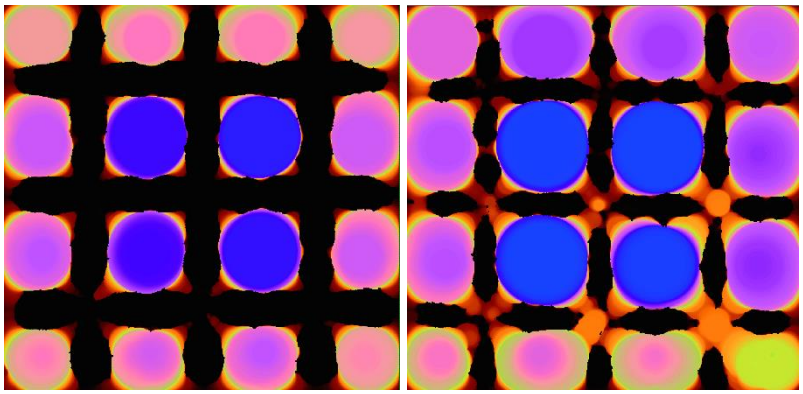

*Figure 5-20. Structure separation of Specimen 1 (left) and Specimen 2 (right).*

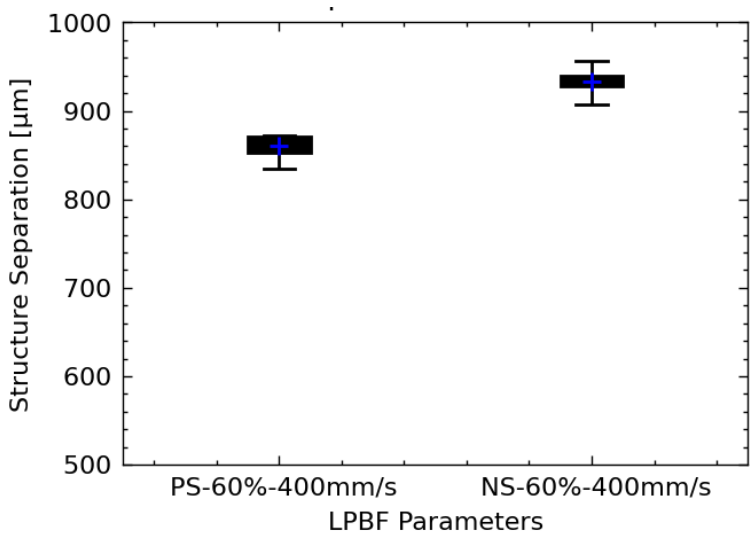


*Figure 5-21. Box plot illustrating the measured structure separation for the two different lattice structure designs (Specimen 1 and 2) with their respective processing parameters.*

Figure 5-21 illustrates the calculated values of the structure separation for Specimen 1 (PS-60%-400mm/s) and Specimen 2 (NS-60%-400mm/s) in relation to the processing parameters. As with the other boxplots shown, the mean of each dataset is indicated by a blue cross. A notable difference between the two specimens is observed; however, both approximate the design value of 1000 µm. The deviation from the design value is anticipated, considering the modification of the beam diameters within the structure (Figure 5-19), which consequently affects the distance between unit cells. Both the beam diameter and cell separation influence the achieved relative density, and their alteration could account for the observed deviation.

The effects of the morphology parameters discussed in this section were evaluated through compression tests on the parts. The results of these compression tests are detailed in the following section.

### *5.3. COMPRESSION TESTS*

Compression tests were conducted using the parameters described in Section 4.5. The mechanical properties of the manufactured lattice structures were compared with the expected properties based on the Gibson-Ashby's model and the solid material properties. Three parts manufactured with the Specimen 1 design and processing parameters, were tested (Figure 5-23). Additionally, one part manufactured with the Specimen 2 design and processing parameters was compressed, the results is shown in Figure 5-24. Only one part from this design was tested because the others were damaged during removal from the building plate. The defects observed in Section 5.2 rendered these parts unsuitable for mechanical testing. However, one sample was modified to remove the section damaged during detachment, reducing its height from 10 mm to 8 mm. This adjustment was accounted for in the strain calculations. All samples were mounted contrary to the building direction in the additive manufacturing process to minimize the risk of toppling over during in-situ testing, as shown in Figure 5-22.

Figure 5-23 shows the stress strain curve of each sample tested of Specimen 1, different color indicates a different sample. The stress plotted in the figure is calculated using the cross-sectional area of the solid parallelepiped rectangle, $25\ \mathrm{mm}^2$. The observed behavior of Specimen 1 (Figure 5-23) reveals an elastic zone and some densification of the structure across all three tests. However, the expected plateau region (Section 4.2.1) is not present in these structures. Densification is particularly notable in Sample 1, while in the other two samples, this effect is minor and less significant than anticipated (Figure 4-4). The calculated elastic modulus ($E$), the yield strength ($\sigma_y$), and ultimate strength ($\sigma_{ult}$) for each test are as follows:

- Test 1: $E = 1.28GPa$, $\sigma_y = 26.03\ MPa$, $\sigma_{ult} = 46.37\ MPa$
- Test 2: $E = 1.29GPa$, $\sigma_y = 27.86\ MPa$, $\sigma_{ult} = 39.80\ MPa$
- Test 3: $E = 1.38GPa$, $\sigma_y = 25.68\ MPa$, $\sigma_{ult} = 37.95\ MPa$

For further details on their calculation, refer to Section 4.5. It is of interest to compare these values with the theoretical values calculated from the Gibson-Ashby's model described in Section 4.2. Using the equations (7) and (8) the theoretical values are: $E_{theo} = 5.14\ GPa$, $\sigma_{y,theo} = 11.68\ MPa$. The disparity between the model's prediction and the experimental results is evident.

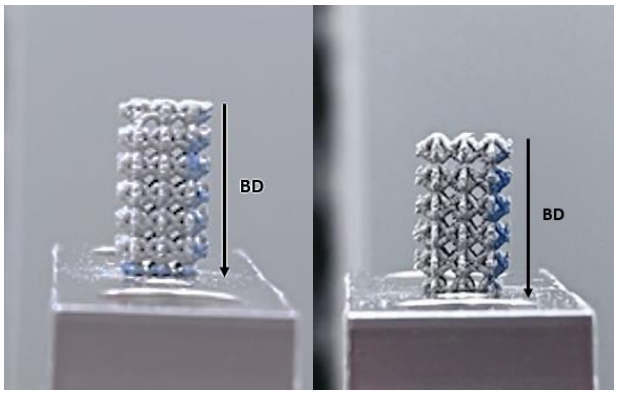


*Figure 5-22. Specimen 1(left) and Specimen 2(right) positioned inside the in-situ testing chamber. The samples were placed contrary to the building direction (BD) of the additive manufacturing process to utilize the more stable surface.*

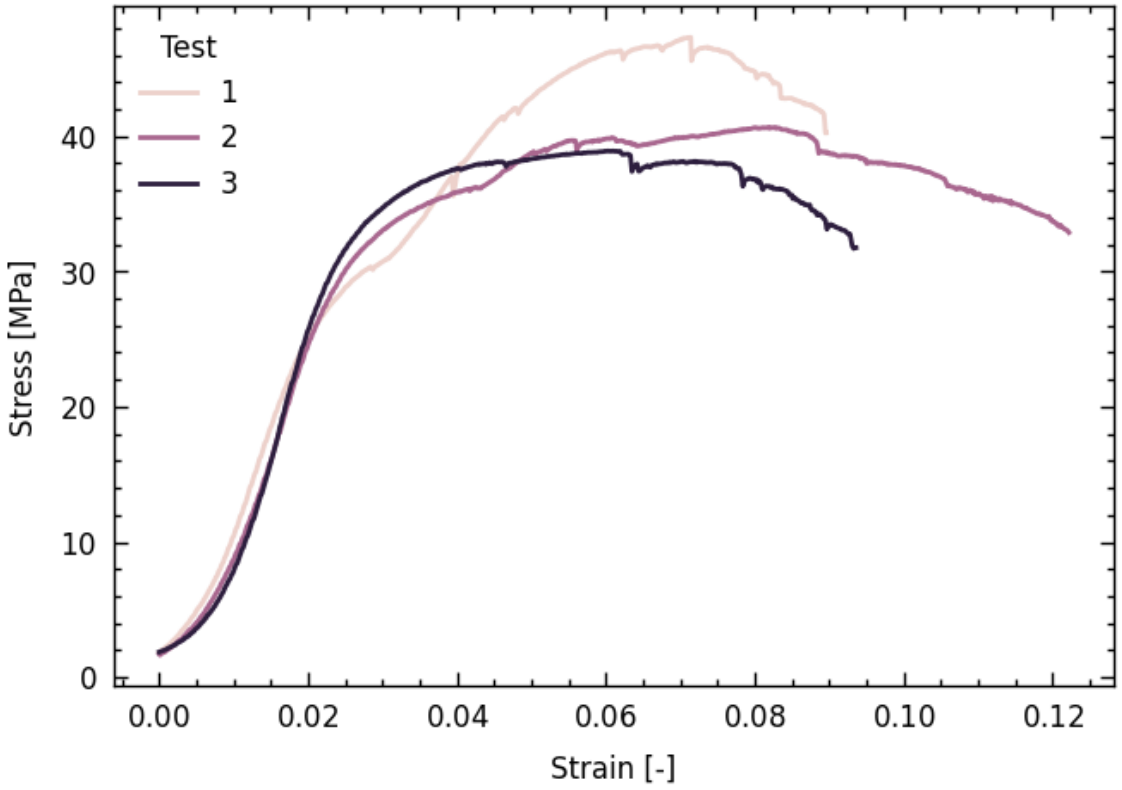


*Figure 5-23. Stress-strain curve for Specimen 1 compression test results. Specimen 1 has a designed beam diameter of 150 µm but a real value of approximately 450 µm. The parts were manufactured using 60% laser power, with 400mm/s laser scan speed and a pre-sintering step. For compression test parameters, consult Section 4.5.*

In Figure 5-24, the stress-strain curve is shown for the Specimen 2 part tested. The stress plotted was calculated in the same manner as the one plotted in Figure 5-23. Regarding the observed behavior, an elastic zone is evident, but densification of the structure is not observed in the tested sample, and the expected plateau region is absent. The behavior exhibited by this specimen is more aptly described as fragile, characterized by the presence of both an elastic zone and a limited plastic zone. The calculated elastic modulus ($E$), the yield strength ($\sigma_y$), and ultimate strength ($\sigma_{ult}$) are provided below.

- Test 1: $E = 0.47GPa$, $\sigma_y = 17.32\ MPa$, $\sigma_{ult} = 18.09MPa$

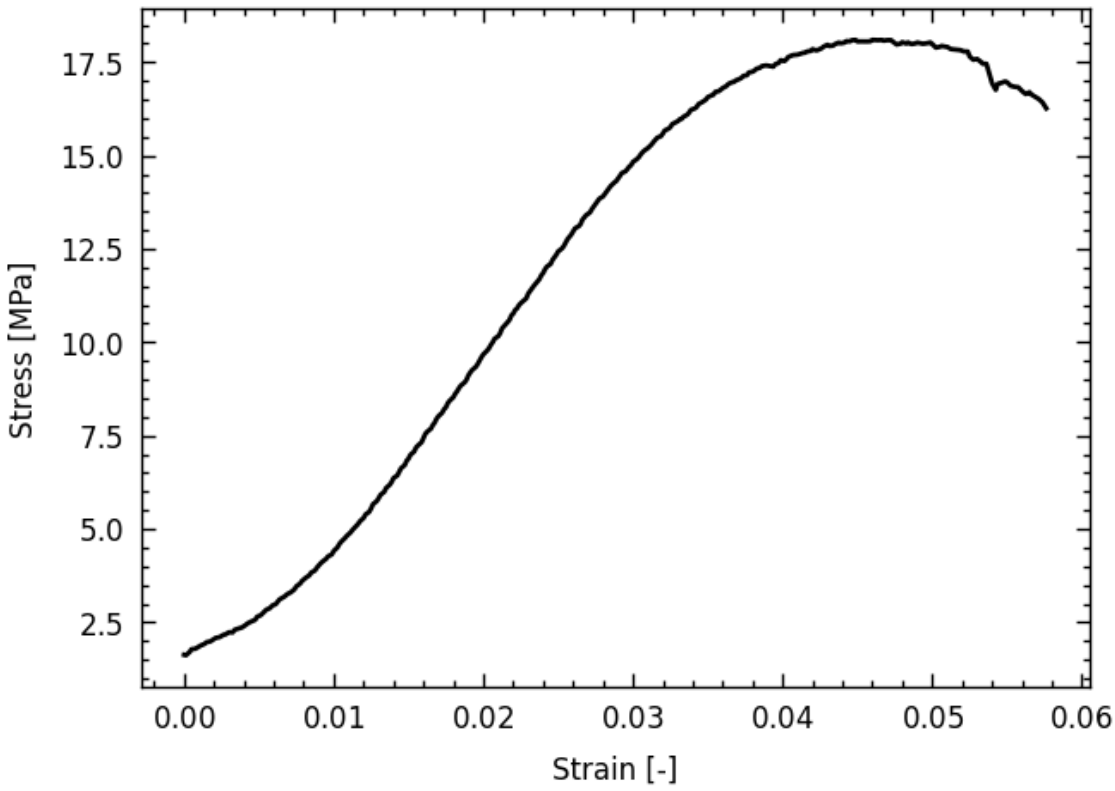


*Figure 5-24. Stress-strain curve depicting the compression test results for Specimen 2. Specimen 2 has a designed beam diameter of 100µm but a real value of approximately 295µm. The part was manufactured using 60% laser power, with 400mm/s laser scan speed and no pre-sintering step. For compression test parameters, consult Section 4.5.*

The behavior observed with Specimen 2 aligns closely with the observed behavior of Specimen 1 but scaled down. This suggests that the model does not accurately predict the elastic modulus or yield stress for the manufactured lattice structures. Furthermore, it can be inferred from the experimentally determined elastic modulus that the manufactured lattices are more compliant than predicted by the model. Additionally, it is noteworthy that the yield stress exceeds the predicted value for both Specimens, implying potential strength surpassing initial expectations. Further investigation is warranted to ascertain whether this phenomenon stems from a combination of material, processing, methods and geometry factors or if other variables are at play.

### *5.4. DVC ANALYSIS*

For the Digital Volume Correlation (DVC) analysis, an in-situ step compression test was conducted. Prior to each step and following the final step, an x-ray scan of the sample was executed. The parameters for the in-situ scans, including an 8.5 µm voxel size, are outlined in Section 4.4. Each step in the in-situ compression test involves a compression of 0.1 mm. The overall anticipated strain, and the number of steps required, were determined based on the findings presented in Figure 5-23. The results of the step compression test conducted on a single sample of Specimen 1 are depicted in Figure 5-25. The DVC analysis is anticipated to illuminate how localized damage affects the behavior of lattice structures under mechanical loading, specifically uniaxial compression.

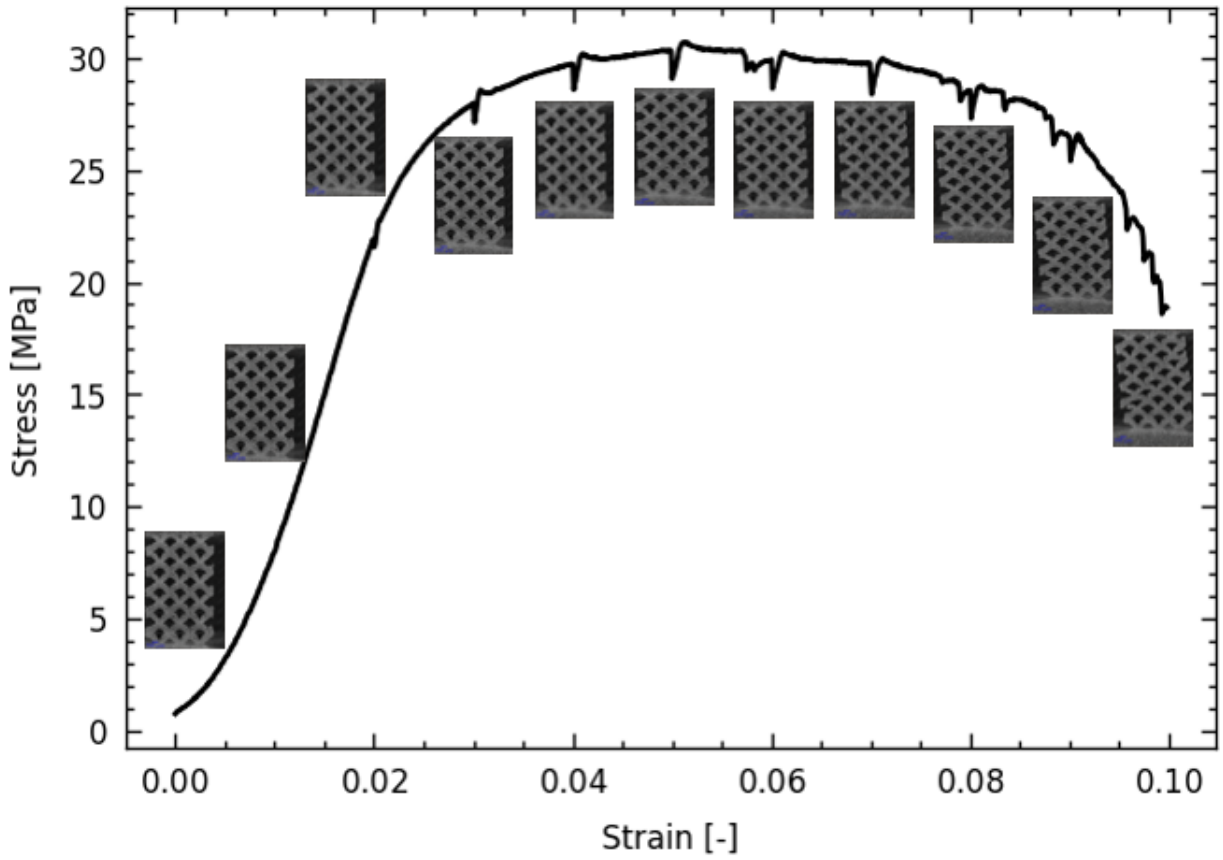


*Figure 5-25. Stress-strain curve depicting the compression test results for Specimen 1, intended for DVC analysis. Stress is calculated using the cross-sectional area of the solid parallelepiped rectangle. Specimen 1 has a designed beam diameter of 150 µm but a real value of approximately 450 µm. The parts were manufactured using 60% laser power, with 400mm/s laser scan speed and a pre-sintering step. For compression test parameters consult Section 4.5.*

Figure 5-25 not only displays the stress-strain curve of the tested Specimen 1 part but also illustrates the structural behavior throughout the test via CT images captured with an 8.5 µm voxel size. Each image corresponds to the equivalent location on the graph when the CT scan was conducted. From the results depicted in the figure, the elastic modulus ($E$), the yield strength ($\sigma_y$), and ultimate strength ($\sigma_{ult}$) can be derived. The calculated values, along with the mean values obtained from Section 5.3, are presented below:

- Specimen 1, step compression test:
  - Elastic modulus (E): $1.18GPa$,
  - Yield strength ($\sigma_y$): $25.09\ MPa$,
  - Ultimate strength ($\sigma_{ult}$): $30.19MPa$
- Mean values from Section 5.3 for Specimen 1:
  - Elastic modulus (E): $1.32GPa$,
  - Yield strength ($\sigma_y$): $26.50\ MPa$,
  - Ultimate strength ($\sigma_{ult}$): $41.22MPa$

A comparison between these values and the mean values obtained from the three tests conducted in Section 5.3 indicates that the mechanical properties determined via the step compression test are lower. This discrepancy could be attributed to the incremental nature of the test, which may cause the lattice structure to repeatedly unload stress, resulting in an alteration of the hardening behavior and influencing the mechanical properties. Alternatively, it is also plausible that this difference is attributable to internal lattice structure defects.

To assess the failure mechanism and determine if it resulted from local defects, such as internal porosity, a local damage analysis was conducted using Digital Volume Correlation (DVC). The Avizo software was utilized for this purpose. Initially, a local DVC approach was employed with a coarse mesh to capture the displacement field of the part. This initial information served as a starting point for the subsequent global DVC analysis with a finer mesh.

To ascertain the optimal mesh sizes, a radial autocorrelation analysis was performed. This analysis provided valuable insights into the typical feature sizes within the image, facilitating the

selection of mesh sizes appropriate for the subsequent analysis. Figure 5-26 illustrates the radial autocorrelation performed on the images, plotting the correlation results against the distance within the image. Ultimately, mesh sizes of 600 µm for the coarse mesh and 300 µm for the finer mesh were utilized. Figure 5-27 presents a 3D representation of the structure with the selected coarse mesh displayed.

Drawing from the stress-strain curve depicted in Figure 5-25, it is discernible that the initial three steps reside within the elastic region, whereas subsequent steps transition into the plastic zone. The computed global displacement fields for steps 0.3-0.4 mm, 0.4-0.5 mm, 0.5-0.6 mm, illustrated in Figure 5-28, reveal a distinct pattern within the displacement vectors immediately following the elastic zone. This suggest a stress concentration emerging in certain areas of the structure.

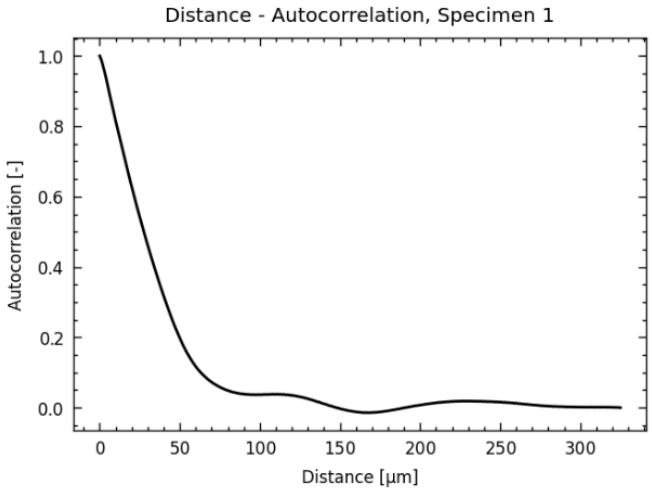


*Figure 5-26. Radial autocorrelation used to determine the optimal mesh size for the DVC analysis of the CT images.*

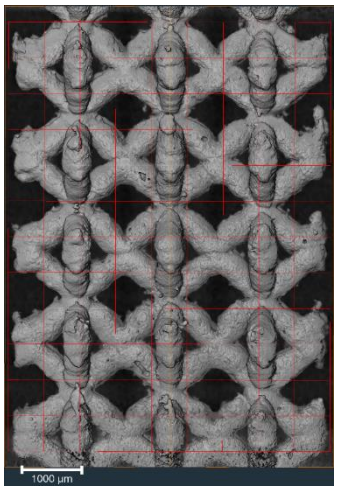


*Figure 5-27. Coarse mesh (red grid) employed for the local approach in DVC analysis of the CT images for Specimen 1.*

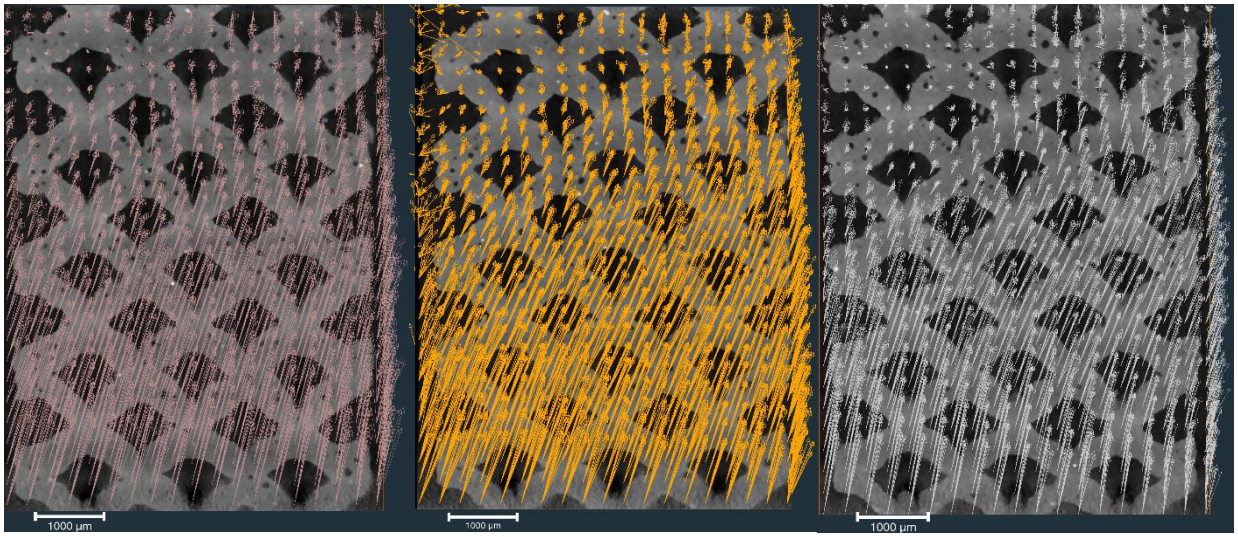


*Figure 5-28. Displacement vector field for Specimen 1, illustrating compression steps from 0.3 to 0.4mm (left), 0.4mm to 0.5mm (middle), and 0.5mm to 0.6mm (right). All views are from the yz plane.*

The discernible trend in the displacement field, as shown in Figure 5-28, reveals a zone exhibiting minimal or no movement, which seems to confirm the stress concentration theory and suggests a potential failure zone nearby. This inference is corroborated by the von Mises strain maps presented in Figure 5-29, Figure 5-30, and Figure 5-31. These 3D representations illustrate the lattice structures viewed from the yz plane. The coloring within each figure depicts the magnitude of strain in the solid, with a colormap legend beneath each representation indicating the specific strain values.

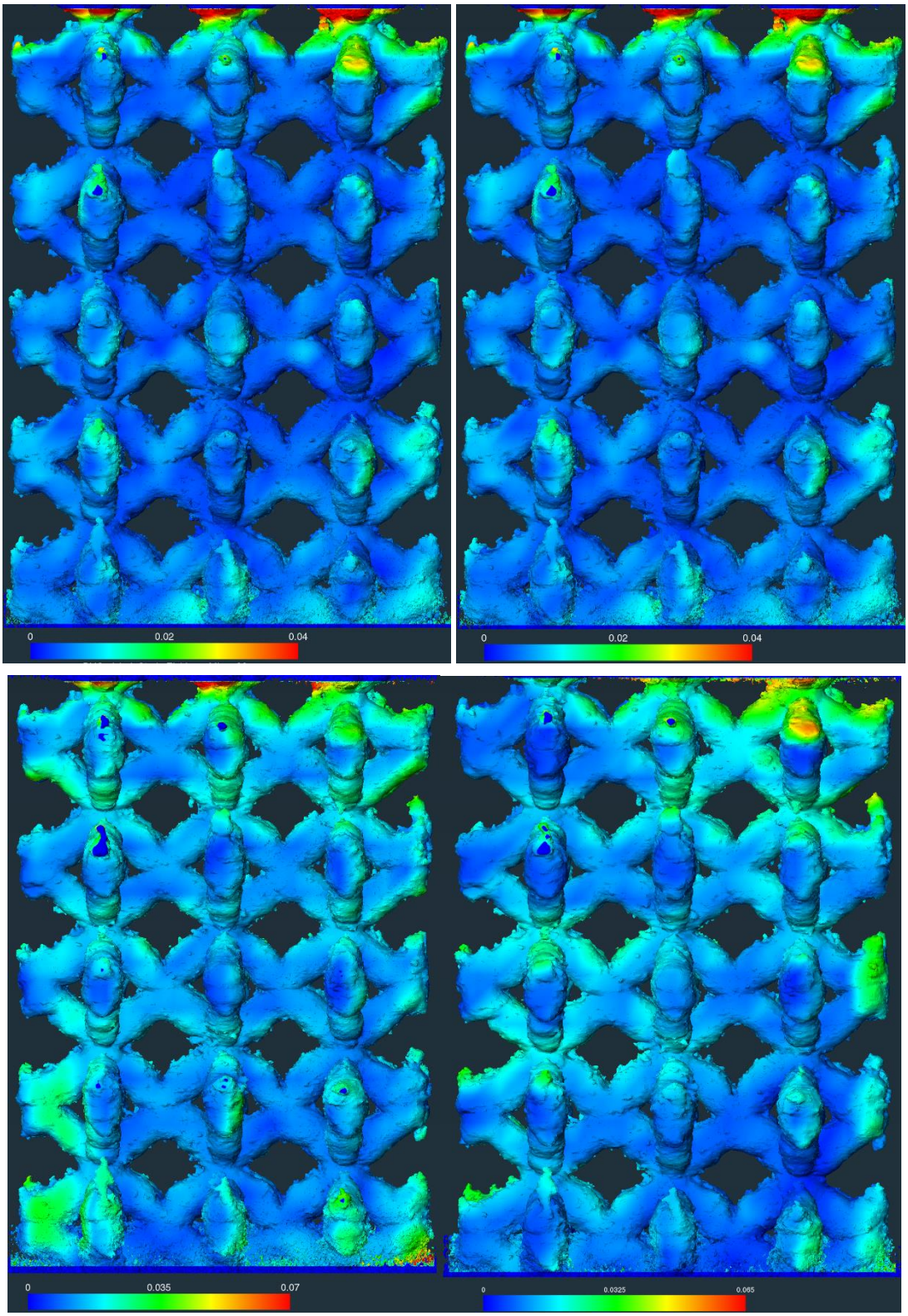


*Figure 5-29. Von mises strain map for compression step: 0.0-0.1 (Top left), 0.1-0.2 (Top right), 0.2-0.3 (Bottom left), and 0.3-0.4 (Bottom right). All views are from the yz plane.*

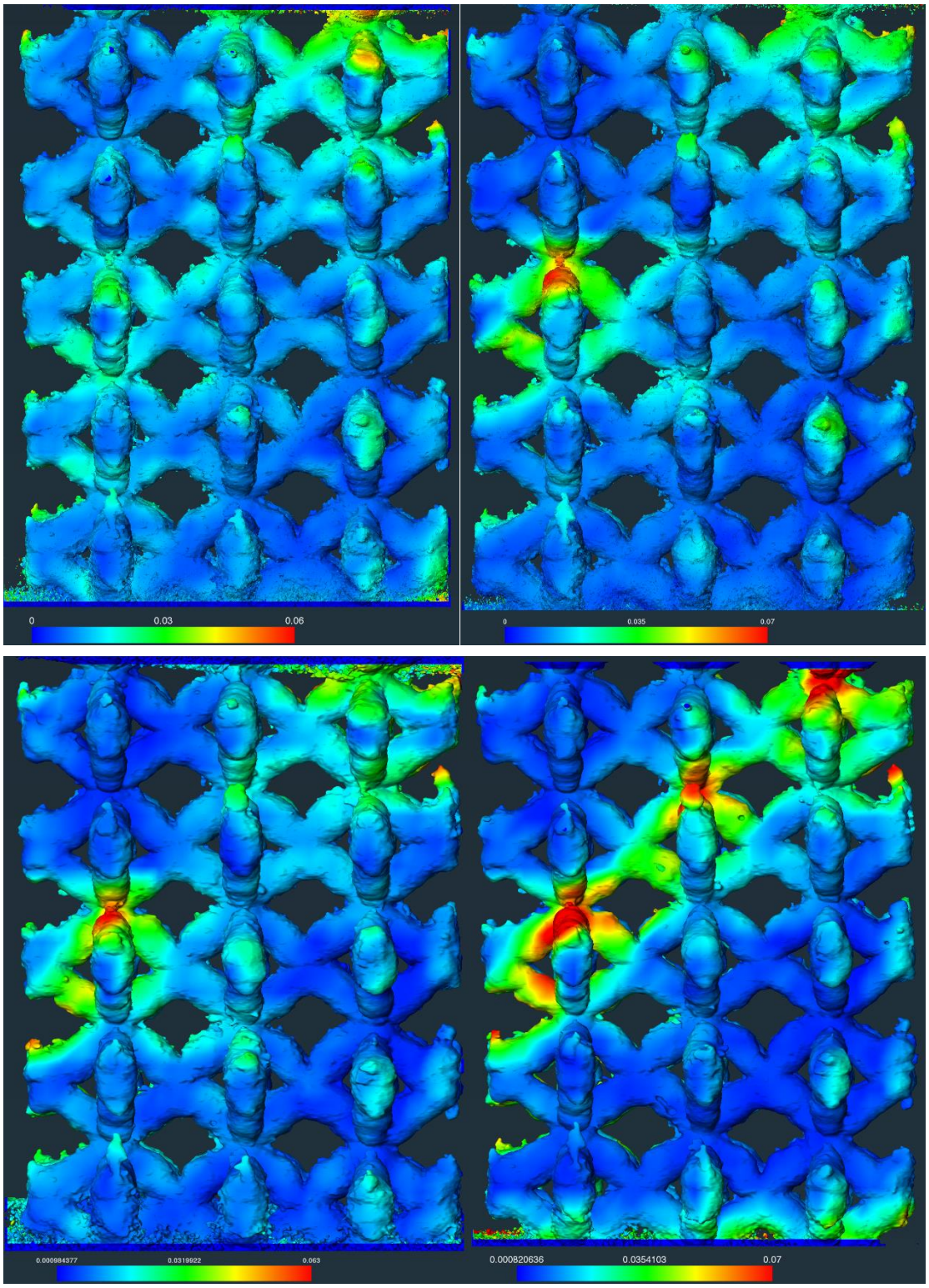


*Figure 5-30. Von mises strain map for compression step: 0.4-0.5 (Top left), 0.5-0.6 (Top right), 0.6-0.7 (Bottom left), and 0.7-0.8 (Bottom right). All views are from the yz plane.*

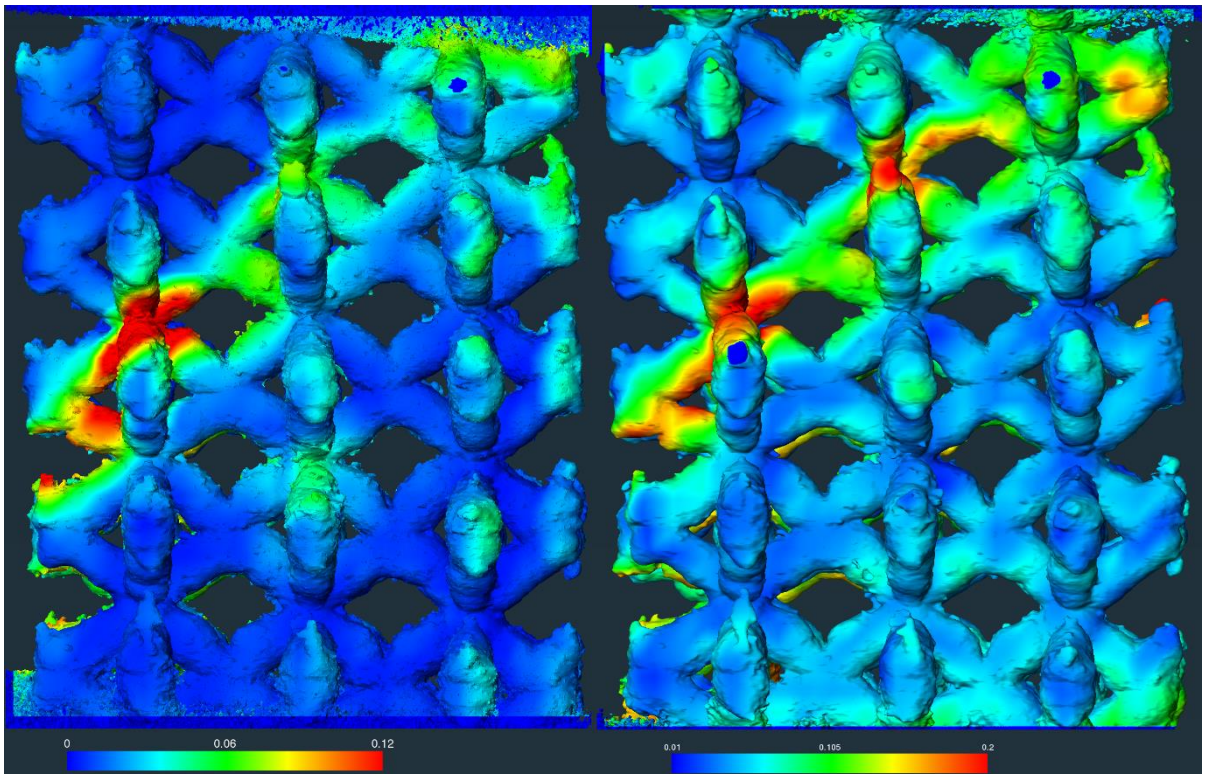


*Figure 5-31. Von mises strain map for compression step: 0.8-0.9 (Left), and 0.9-1.0 (Right). Both views are from the yz plane.*

Figure 5-29 displays the von Mises strain map for steps ranging from no compression to 0.4mm compression, illustrating no visible strain tendency. This is expected since all the steps represented are within the elastic zone or just past the yield strength. In contrast, Figure 5-30, shows the structural tendency towards diagonal plane deformations. Additionally, Figure 5-31 highlights the failure zone with the two last compression steps, from 0.8 to 1.0mm. Coupled with Figure 5-31, the damage propagation within the zone becomes evident, accompanied by an increase in overall strain across a diagonal plane of the structure, resulting in some buckling.

To determine if a pre-existing defect within the structure biased the stress concentration to that specific zone, sectional views of the structure were created and are shown in Figure 5-32, Figure 5-33, and Figure 5-34. Figure 5-32 presents a sectional view of the structure in the step 0.4-0.5mm. The left side of the figure shows the section from the xz plane, and the right side form the yz plane. The yz plane indicates the specific part of the structure visible in the xz view. The xz view reveals an internal defect created by a sharp junction of the beams (nodes), suspected to be the source of the concentration.

Figure 5-33 depicts the following step (0.5-0.6 mm), where the progression from stress concentration to strain localization is noticeable. Figure 5-34 shows the sectional views of the subsequent step (0.6-0.7 mm). Here, the defect near the node begins to create a hinge that drives the buckling of the structure. It can be observed that the defect itself appears to be closing due to ongoing compression.

The behavior of the structure as represented by the results of the DVC analysis of the images will be discussed in further detail within Section 6.

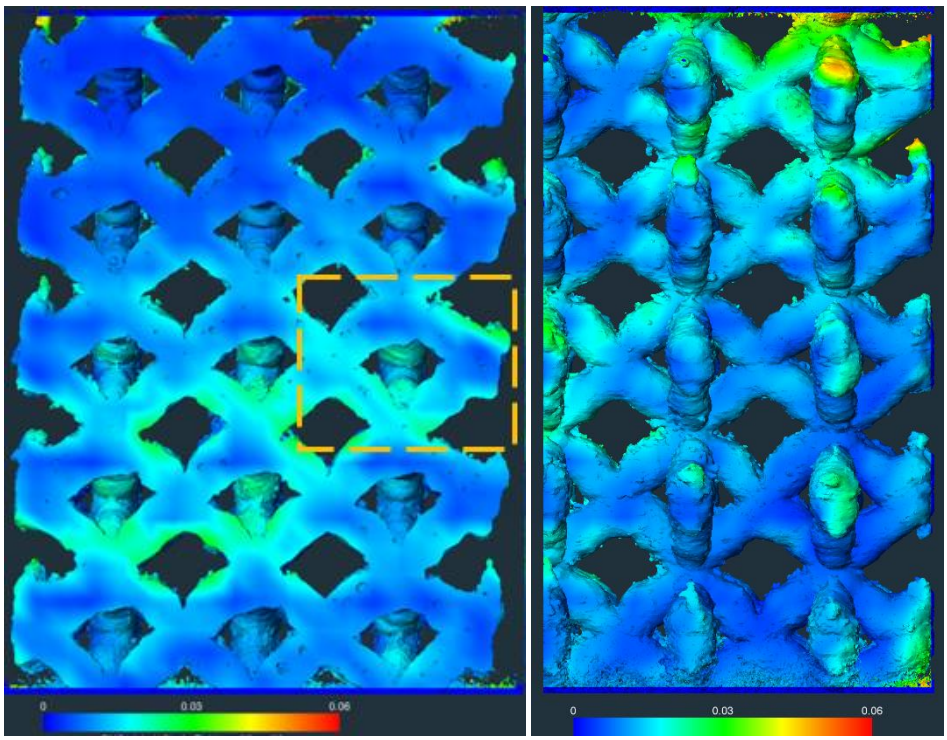


*Figure 5-32. Von mises strain map for compression step 0.4-0.5mm. The left displays the sectional view of the structure from the xz plane, while the right presents the cut structure from the yz plane.*

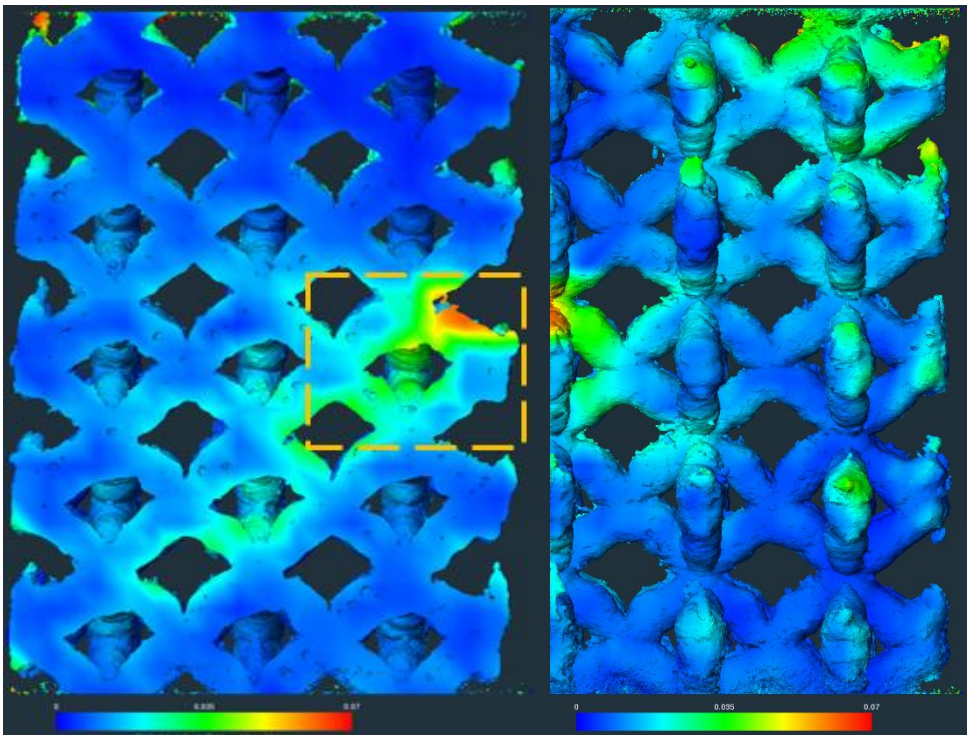

*Figure 5-33. Von mises strain map for compression step 0.5-0.4mm. The left displays the sectional view of the structure from the xz plane, while the right presents the cut structure from the yz plane.*

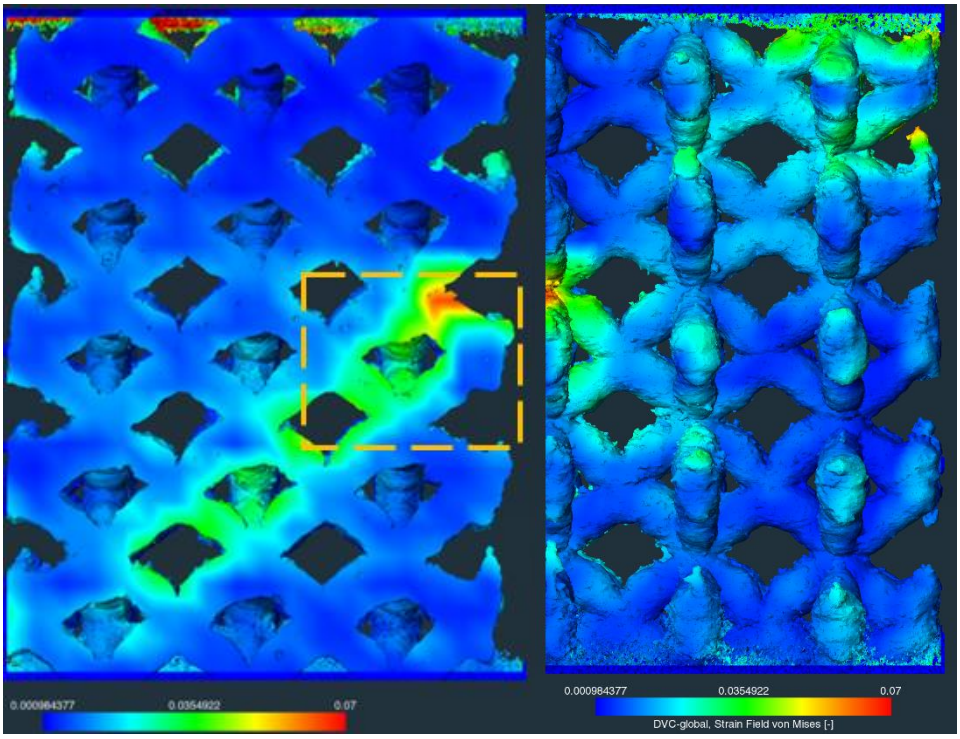


*Figure 5-34. Von mises strain map for compression step 0.6-0.7mm. The left displays the sectional view of the structure from the xz plane, while the right presents the cut structure from the yz plane.*

### *5.5. HEALING HEAT TREATMENT (HHT)*

To assess the healing capabilities of the parts given the particular properties of the material, some preliminary healing heat treatments (HHT) were performed. The HHT protocols applied to the lattice structures were previously defined and utilized by Gheysen et. al. [2]. As noted in Section 4.6, the intended HHT for liquid assisted healing involves heating to 540°C for 30 min, followed by air cooling or water quenching. Various lattice structures were employed for this preliminary assessment, all manufactured under the following parameters: Laser Power at 60% (163.8 W), laser scan velocity 400 $\frac{mm}{s}$ with pre-sintering.

The assessment began with HHT of a lattice structure designed with an intended beam diameter of 200 µm, utilizing a double BCC lattice structure (Figure 5-35). The HHT applied was 540°C for 30 minutes with water quenching, and the results are presented in Figure 5-35 via CT images. It is readily noticeable that the HHT was unsuccessful. The yellow markings in the figure highlight the same zones before and after HHT. All the porosities within these markings increased in size, which reflects the overall trend observed in the sample.

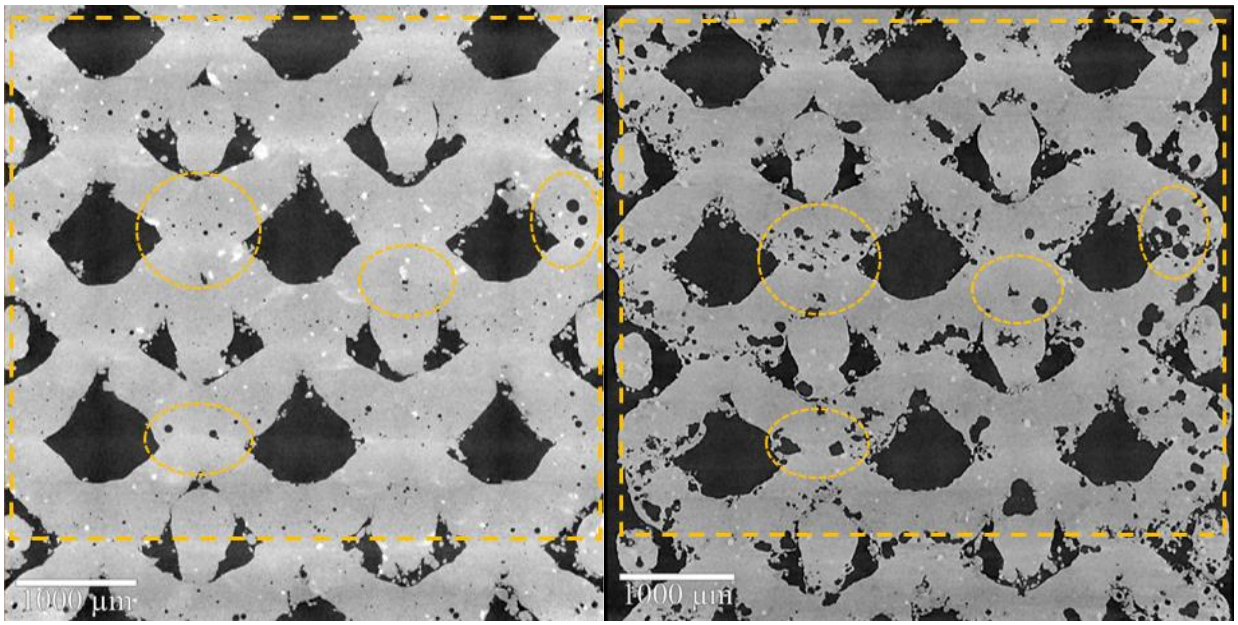


*Figure 5-35. CT images of a lattice structure design with processing parameters set 1. This particular lattice structure design is not included within the designs described in Section 4.2, but it was useful for evaluating the HHT of the material with this type of geometry. The intended beam diameter of the shown part is 200 µm, featuring a reinforced BBC structure. The image on the left shows the structure before HHT, and the image on the right shows it after HHT at 540°C for 30 minutes with water quenching. For details on the LPBF parameters, refer to Table 4-3.*

Following the unsuccessful initial HHT, a second HHT with air cooling was performed. Air cooling was selected because it was hypothesized that the observed structural response might be due to an interaction between the water and the magnesium. However, it is also possible that the response is due to and interaction between the water and the liquid metal. A lattice structure with a 300 µm beam diameter and a double BCC lattice structure was used for this trial; the results of this process are shown in Figure 5-36 via CT images. As in the previous images, the yellow markings indicate approximately the same locations before and after HHT, shown on the left and right respectively. The increase in porosity appears to be greater than that observed with water quenching. Thus, it suggests that the porosity growth is more likely related to the duration at high temperatures rather than an interaction between water and magnesium or water with liquid metal, as initially suspected.

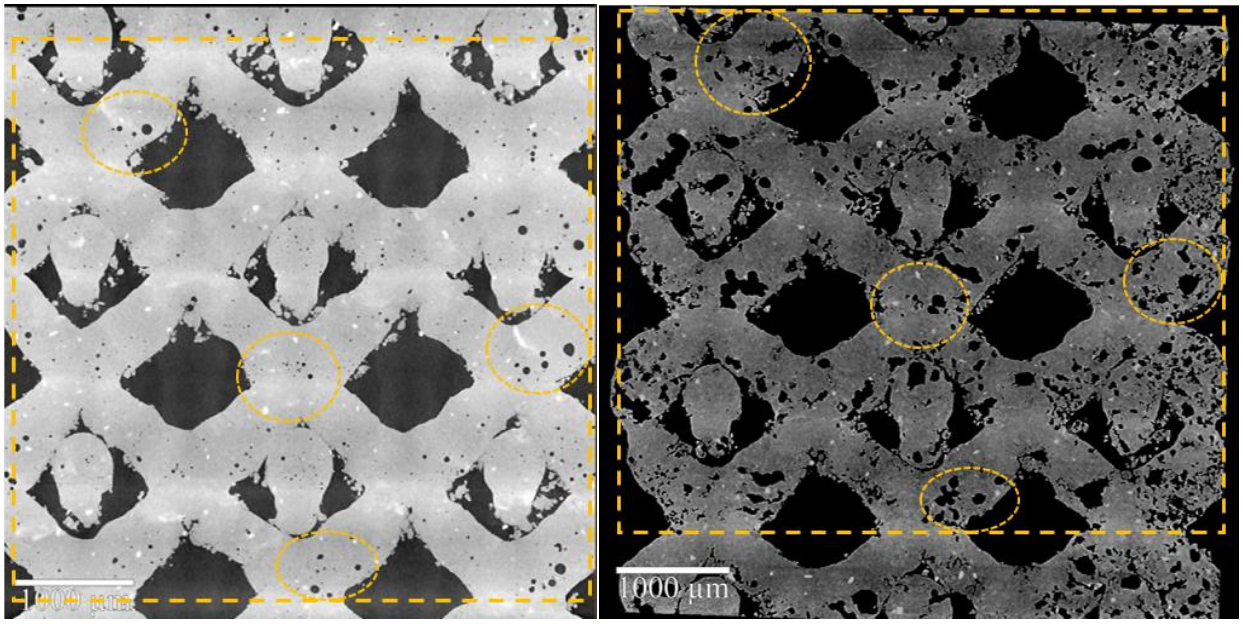


*Figure 5-36. CT images of a lattice structure design with processing parameters set 1. This particular lattice structure design is not included within the designs described in Section 4.2, but it was useful for evaluating the HHT of the material with this type of geometry. The intended beam diameter of the shown part is 300 µm, featuring a reinforced BBC structure. The image on the left shows the structure before HHT, and the image on the right shows it after HHT at 540°C for 30 minutes with air cooling. For details on the LPBF parameters, refer to Table 4-3.*

Subsequently, a diffusion based HHT was conducted to verify the effectiveness of this healing strategy for the lattice structures. Following the protocol outlined in Section 4.6, the treatment was performed at 400°C for 30 minutes with air cooling. The lattice structure used for this HHT was Specimen A design, with LPBF processing parameters set 1, as previously described. Figure

5-37 presents the results for this treatment, which show a distinct difference from the results of the earlier HHTs.

Notably, there was no significant growth in porosity, as experienced with previous HHTs. Some porosities appeared to decrease or disappear, but measurements using Avizo software and the segmentation editor indicated otherwise. The internal porosity was 0.89% before HHT and 1.03% after HHT. This suggests that porosities did, in fact, grow. However, the histogram of the equivalent diameter of the porosities (Figure 5-38) shows a decrease in overall porosity diameter, with an increase in the number of smaller porosities (those below 20 µm).

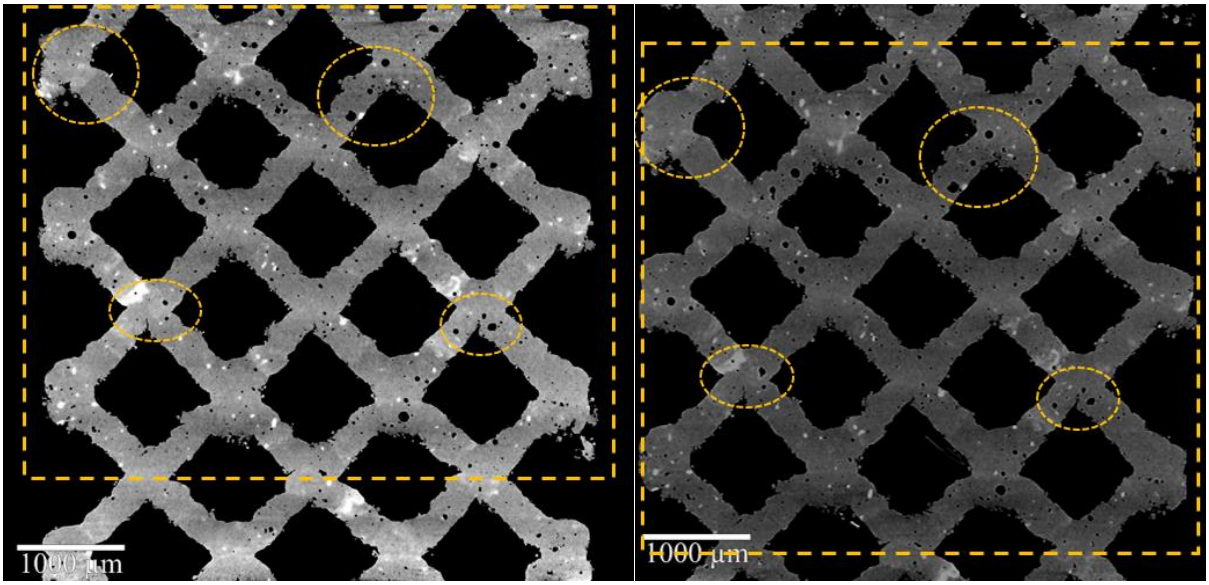


*Figure 5-37. CT images of a lattice structure design Specimen A with processing parameters set 1. The image on the left shows the structure before HHT, and the image on the right shows it after HHT at 400°C for 30 minutes with air cooling. Specimen A has an intended beam thickness diameter of 100 µm. For more details on Specimen A design, refer to Table 4-2, and for details on the LPBF parameters, refer to Table 4-3.*

Continuing the investigation, it was hypothesized that the behavior observed during the HHT was due to an excess of magnesium content within the lattice structure. Gheysen et al. demonstrated that the HHT was effective for a part with a final composition of 8.4 weight % of Mg [2]. Although the parts in the investigation were manufactured with the same magnesium content powder composition (14% wt. Mg) as used in their investigation, there was insufficient vaporization of magnesium to achieve the content they used. It is important to note that the

powder employed in this investigation was pre-mixed, unlike the manually mixed powder used by Gheysen et al. [2].

A composition analysis of several lattice structures manufactured during the preliminary process described in Section 5.1 was conducted, with results presented in Table 5-1. The analysis reveals that regardless of the beam diameter, no significant amount of magnesium is lost during processing, contrary to expectations based on previous research. Furthermore, the results indicate that a substantial percentage of magnesium is lost during the 540°C HHT, which is not observed at the 400°C HHT. The difference between the samples with pre-sintering and those without is not significant enough to suggest that pre-sintering impacts the overall chemical composition of the structure. However, careful consideration needs to be taken when applying the results shown in Table 5-1 because only a small amount of material was available and could have influenced its accuracy.

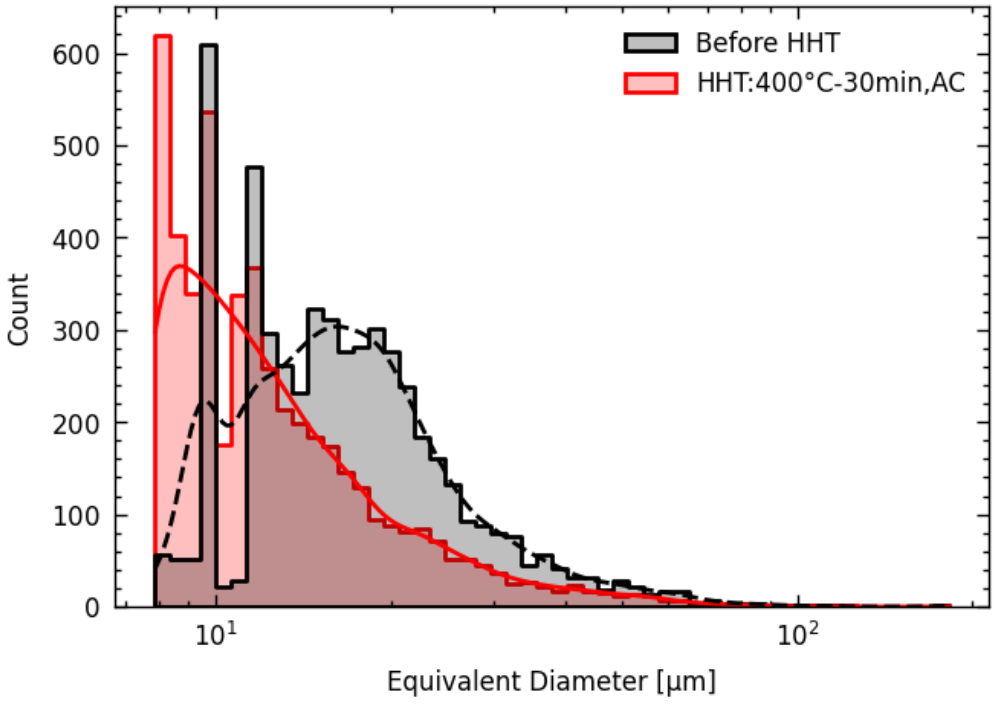


*Figure 5-38. Histogram of the equivalent porosity diameters for Specimen A lattice structure, processed with parameters 1, before HHT and after an HHT at 400°C for 30 minutes with air cooling (AC). For further details on Specimen A, refer to Table 4-2, and for LPBF parameters, refer to Table 4-3.*

*Table 5-1. T*hree-acid attack (HF, HCL, HNO3) and fusion characterization of the composition of selected manufactured lattice structures. Since the parts used for this analysis are destroyed during testing, the structures differ from those described in Section 4.2. Lattice structures with beam diameters of 100 and 400µm were used, featuring BBC and double BBC structures configurations respectively, were analyzed. Some structures were tested post-HHT, with specific processing parameters detailed below the table.

**COMPOSITION [%WT.]**

| | Beam Ø100um, LPBF Parameters - 1 | Beam Ø100um, LPBF Parameters - 2 | Beam Ø100um, LPBF Parameters - 1 HHT - 1 | Beam Ø400um, LPBF Parameters - 1 | Beam Ø400um, LPBF Parameters - 1 HHT- 2 |
|---|---|---|---|---|---|
| **Al** | 86.1 | 84.1 | 84.2 | 85.2 | 87.0 |
| **Cr** | 0.02 | 0.03 | 0.02 | 0.02 | 0.03 |
| **Cu** | 0.04 | 0.06 | 0.05 | 0.03 | 0.04 |
| **Fe** | 0.13 | 0.10 | 0.09 | 0.09 | 0.11 |
| **Mg** | 12.1 | 13.7 | 11.1 | 13.1 | 9.11 |
| **Ni** | 0.01 | 0.02 | 0.01 | 0.01 | 0.02 |
| **Si** | <0,01 | 0.06 | 0.21 | 0.04 | 0.30 |
| **Sn** | 0.07 | 0.09 | 0.08 | 0.08 | 0.07 |
| **Zn** | <0,01 | 0.05 | 0.01 | 0.02 | 0.04 |
| **Zr** | 1.22 | 1.54 | 1.28 | 1.35 | 1.45 |

LPBF Parameters 1: Laser Power at $60\%$, Laser Scan Velocity $400\ \frac{mm}{s}$, with Pre-Sintering
LPBF Parameters 2: Laser Power at $60\%$, Laser Scan Velocity $400\ \frac{mm}{s}$, with No Pre-Sintering
HHT 1: $400°C$ for 30 minutes with air cooling
HHT 2: $540°C$ for 30 minutes with air cooling

Gheysen et al. concluded that a magnesium content of 23.7% wt. is too high to exhibit any healing properties due to the high amount of eutectic phase within the microstructure. As explained in Section 2.1, while the low melting point eutectic phase is essential for activating liquid-assisted healing, and excessive amount can cause structural problems during HHTs. The HHT at 450°C they performed on a sample with this magnesium percentage failed, yielding results similar to those experienced by our samples with an HHT at 540°C. Consequently, it was of interest to evaluate the performance of structures subjected to this specific HHT. Based on the performance of the structures, it can be determined whether the magnesium concentration supports liquid-assisted healing.

The HHT performed was 450°C for 30 minutes with air cooling. According to the Al-Mg phase diagram (Figure 5-39), 450°C is the eutectic melting temperature, indicating the minimum

temperature required to melt the eutectic phase within the structure [69]. The results of this HHT, conducted on three parts of Specimen 1 design and three parts of Specimen 2 design are shown below.

The histograms of the equivalent diameter of the parts before and after the HHT at 450°C are presented in Figure 5-40 and Figure 5-41. Specimen 1 exhibits an intriguing behavior: while the larger sized porosities (approximately above 15 µm) remain constant or show slight fluctuations, the number of porosities smaller than 15 µm increases significantly. This pattern is different to the observed with the previous HHT at 400°C, where the larger sized porosities decreased in number while the smaller sized increased. In contrast, Specimen 2 demonstrates behavior indicative of porosity growth (Figure 5-41).

The increase in the count of all equivalent diameters suggests that the HHT creates new porosities and enlarges existing ones. This is corroborated by Figure 5-42, which compares the boxplot of the internal porosity before and after HHT. It is evident that while Specimen 1 (PS-60%-400mm/s) shows a slight increase in mean internal porosity percentage from 2.25% to 2.5%, Specimen 2 (NS-60%-400mm/s) experiences a more substantial increase from 1.43% to 4.04%. This confirms the observations from Figure 5-40 and Figure 5-41.

The CT images shown in Figure 5-43 and Figure 5-44, illustrate the phenomenon observed on the histograms. Specimen 1 (Figure 5-43) shows the porosity sizes maintained or slightly increased while Specimen 2 clearly shows and increase of the porosity size and the appearance of smaller sized porosities throughout the complete structure. This allows to confirm the behavior for each Specimen as well as the difference between them.

It is important to note that the defect discussed in Section 5.2 is still present after the HHT (Figure 5-44) which is consistent with the no healing effect perceived by the Specimen. As well, the CT images, if compared with the images after the HHT at 540°C, show a better result. Even if Specimen 2 did not show healing after the 450°C treatment the lack of extreme growth gives hope for a possible adjustment that yields better results.

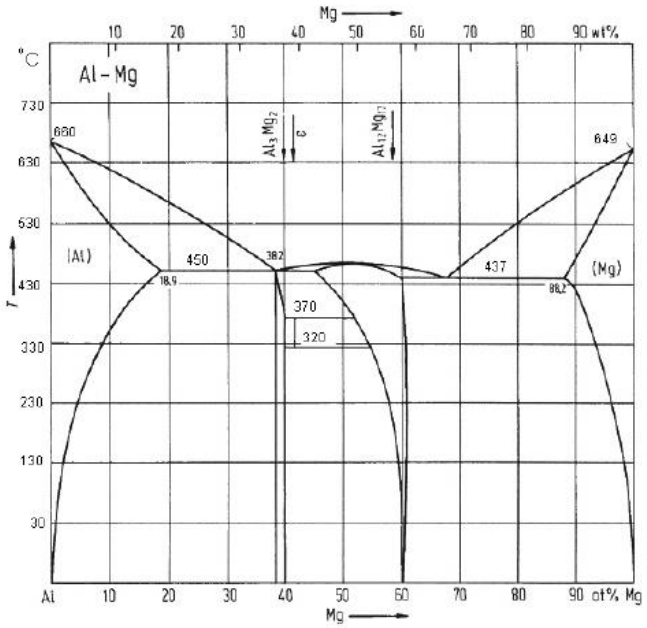


*Figure 5-39. Al-Mg phase diagram. The eutectic phase melting temperature is 450°C. [69].*

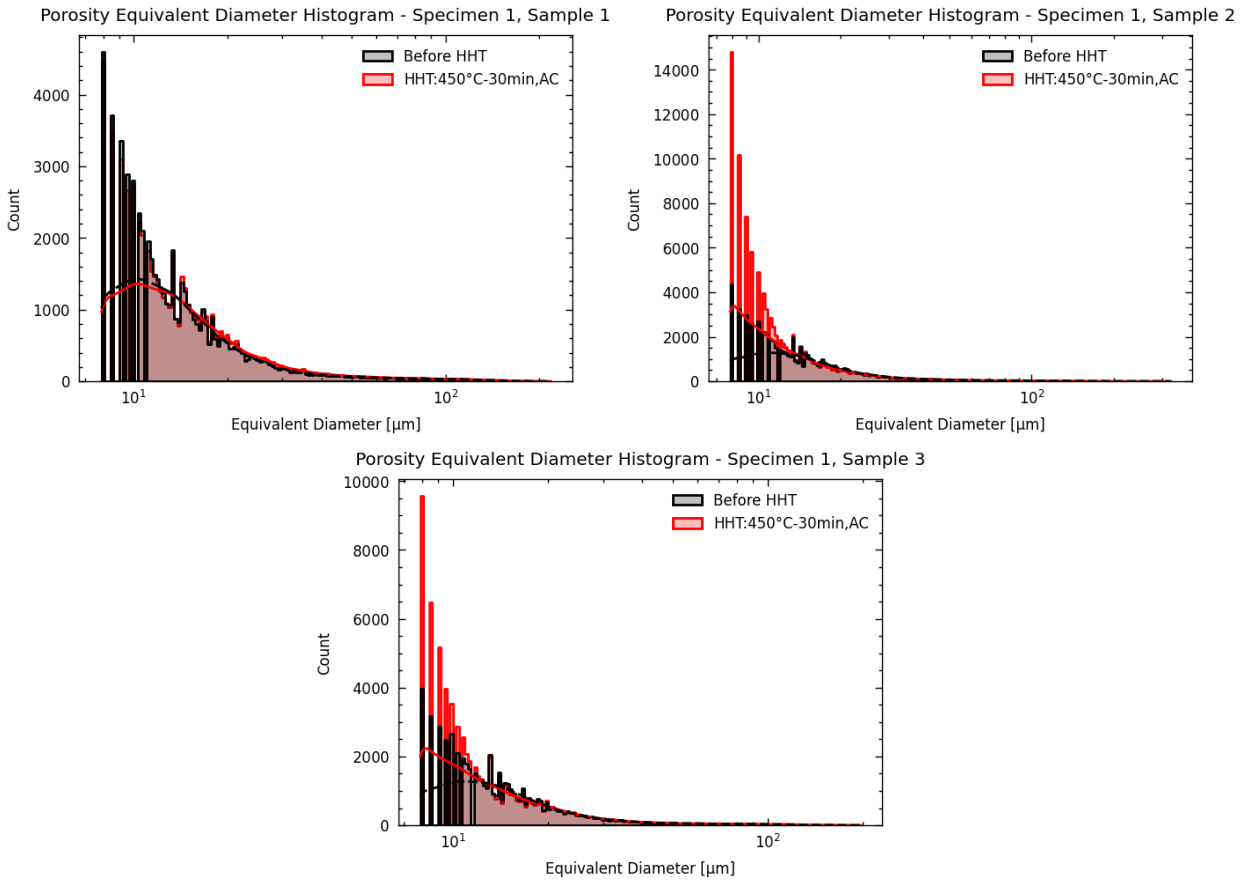


*Figure 5-40. Histograms of the porosities equivalent diameter for lattice structure design Specimen 1 samples, before and after HHT at 450°C for 30 min with air cooling (AC). Refer to Table 4-2 for more specimen 1 details and to Table 4-3 for LPBF parameters details. The measurements were performed with CT images acquired with a 4 µm voxel size.*

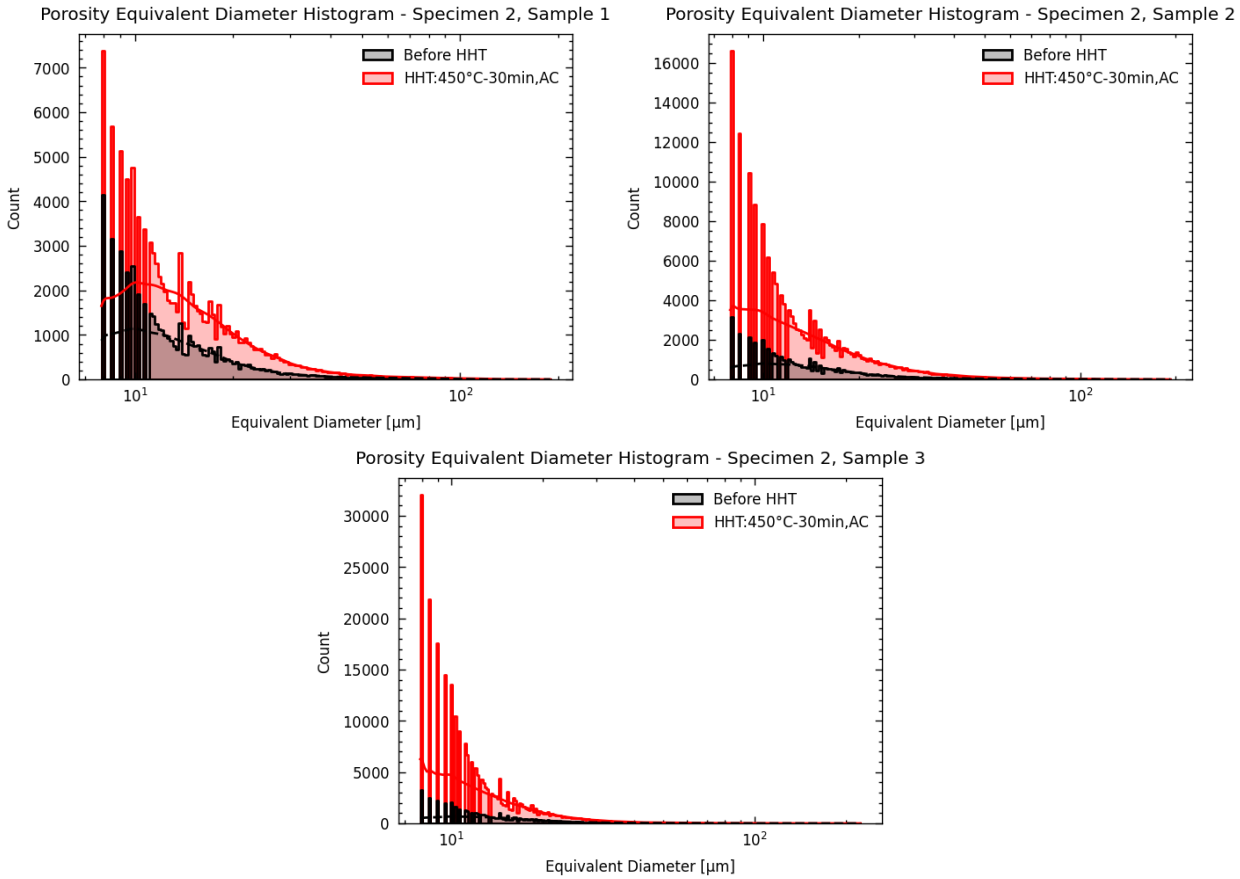


*Figure 5-41. Histogram of the porosities equivalent diameter for lattice structure design Specimen 2, before and after HHT at 450°C for 30 min with air cooling (AC). Refer to Table 4-2 for more Specimen 2 details and to Table 4-3 for LPBF parameters details. The measurements were performed with CT images acquired with a 4 µm voxel size.*

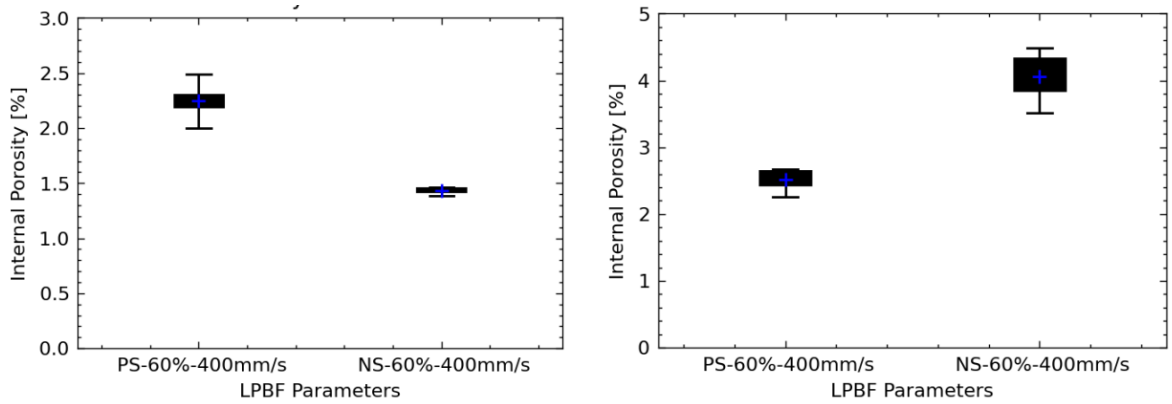


*Figure 5-42. Box plot of the measured internal porosities for the two different lattice structure designs, Specimen 1 – PS-60%-400mm/s, and Specimen 2-NS-60%-400mm/s. Before HHT on the left (Figure 5-14) and after HHT at 450°C for 30 min with air cooling (AC), on the right. Refer to Table 4-2 for more lattice structure designs details. The measurements were performed with CT images acquired with a 4 µm voxel size.*

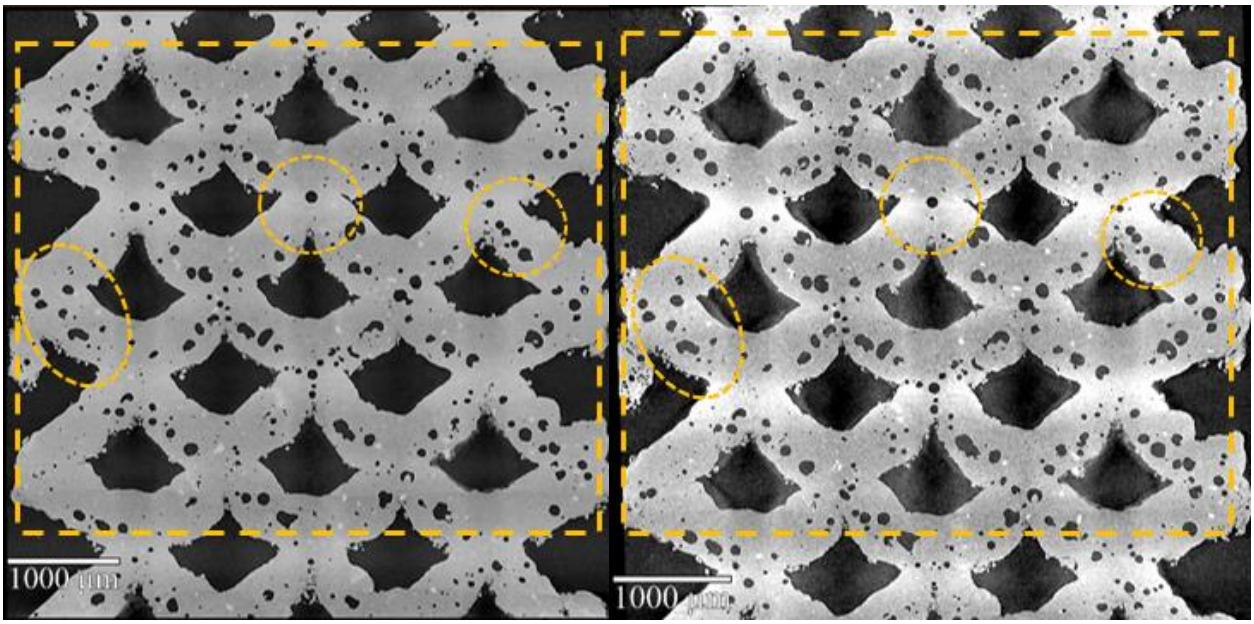


*Figure 5-43. CT images of lattice structure design Specimen 1, sample 3. On the left the structure before HHT and on the right after an HHT at 450°C for 30 min with air cooling. Specimen 1 has an intended beam thickness diameter of* $150\ \mu m$*. Refer to Table 4-2 for more specimen A details and to Table 4-3 for LPBF parameters details.*

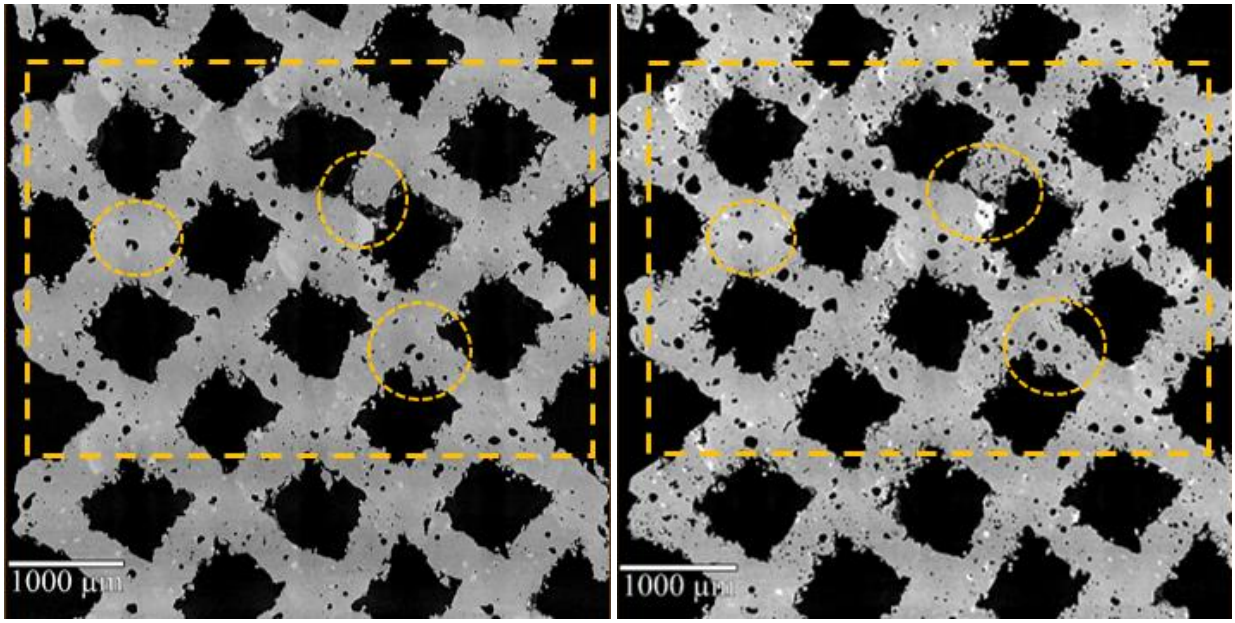


*Figure 5-44. CT images of lattice structure design Specimen 2, sample 1. On the left the structure before HHT and on the right after an HHT at 450°C for 30 min with air cooling. Specimen 2 has an intended beam thickness diameter of* $100\mu m$*. Refer to Table 4-2 for more specimen A details and to Table 4-3 for LPBF parameters details.*

# 6. DISCUSSION

## *6.1. IMPACT OF PROCESSING PARAMETERS IN LATTICE STRUCTURES*

The preliminary results from the LPBF process provided insights into how processing parameters impact the overall quality of the lattice structure. Four different parameter sets were tested, using two different linear energy densities (LED):

- 60% Laser power, 400mm/s Laser scan speed; $LED = 0.409\ \frac{J}{mm}$
- 70% Laser power, 300mm/s Laser scan speed; $LED = 0.637\ \frac{J}{mm}$

These combinations were selected based on the expertise from the institute (iMMC), as they had previously demonstrated good manufacturability of the alloy in question during previous research.

Analysis of internal porosity percentage, real beam diameter, and real relative density, indicated that the parameters yielding more accurate lattice structure, closely matching the intended design, were those with an LED of 0.409 J/mm. The parts manufactured with an LED of 0.637 J/mm exhibited a significantly more pores – 3.5 times more than those with an LED of 0.409 J/mm – and these pores were larger and less spherical in shape. Spherical porosities are typically preferred due to their reduced impact on mechanical properties. Less spherical porosities are associated with lack of fusion defects, but the high LED suggests that the observed porosities are likely due to keyhole mode induced by the high energy input. This indicates that the LED alone is not sufficient for optimizing processing parameters.

Following the recommendation of Oliveira et al.[29], the appropriate LED was selected first, allowing for the selection of hatching space and layer thickness. A useful parameter that incorporates hatching space and the layer thickness into the analysis is the volumetric energy density (VED), calculated as,

$$VED = \frac{Laser\ Power}{Laser\ Scan\ Speed * Hatching\ Space * Layer\ thickness} \quad (9)$$

With a constant layer thickness used of 30 µm, the values of VED used for the preliminary lattice structures were calculated and summarized in Table 6-1. Four different VED values were tested, and results from Section 5.1 indicate good manufacturability observed in the CT images is primarily related to the LED. Specimen A and Specimen B, which used the same LED but different VED values, showed both good dimensional accuracy in their lattice structure. The cracks observed in Specimen B (Figure 5-2, (a)) CT images are suspected to be related to its VED value. Consequently, given the defects observed at a VED of 136.5 J/mm$^3$, the optimal VED for subsequent manufactured parts was determined to be 455 J/mm$^3$. This VED influenced the decision to maintain a beam diameter design of 100 µm, as seen in Specimen A, for Specimen 2.

*Table 6-1. Summary of the processing parameters used for the preliminary printing of the lattice structures. The VED parameter is calculated with equation (9).*

| Lattice Design | Laser Power [%] | Laser Speed [mm/s] | Hatching Space [µm] | Layer Thickness [µm] | VED [J/mm^3] |
|---|---|---|---|---|---|
| *SPECIMEN A* | 60 | 400 | 30 | 30 | 455.00 |
| *SPECIMEN A* | 60 | 400 | 30 | 30 | 455.00 |
| *SPECIMEN A* | 70 | 300 | 30 | 30 | 707.78 |
| *SPECIMEN A* | 70 | 300 | 30 | 30 | 707.78 |
| *SPECIMEN B* | 60 | 400 | 100 | 30 | 136.50 |
| *SPECIMEN B* | 60 | 400 | 100 | 30 | 136.50 |
| *SPECIMEN B* | 70 | 300 | 100 | 30 | 212.33 |
| *SPECIMEN B* | 70 | 300 | 100 | 30 | 212.33 |

Additionally, the manufacturing results of Specimen 1 and Specimen 2 intended for compression tests (Section 5.2) revealed that more factors influence the quality of lattice structures. The intended post-manufacturing beam diameter for both designs was 300 µm. While Specimen 2 met this target, Specimen 1 had a resulting diameter of approximately 450 µm. This discrepancy suggests potential issues in the manufacturing process, particularly with the scanning strategy. The deviation of 150 µm from the expected value, along with an estimated melt pool size of approximately 200 µm, supports this hypothesis.

Figure 4-5 (a) shows the laser scan pattern followed for Specimen A, which was expected to be followed during the manufacturing of Specimen 1 and 2. However, Figure 6-1 shows the scan

patterns actually followed for Specimen 1 (left) and Specimen 2 (right). Due to the use of the same processing parameters, the pattern was not verified. Given the beam diameter adjustment of Specimen 1 (to 150 µm), a concentric scanning path within the structure was added to complete the form (Figure 6-1, left), which was not desired.

This extra scanning path is believed to have caused the unexpected behavior, including beam diameter deviation and increased internal porosity. It is suspected that the laser path's proximity to the previous path resulted in excess energy within the sintering region, causing the observed porosity. This would also explain why the porosity is spherical but larger than what is typically expected for keyhole mode porosities.

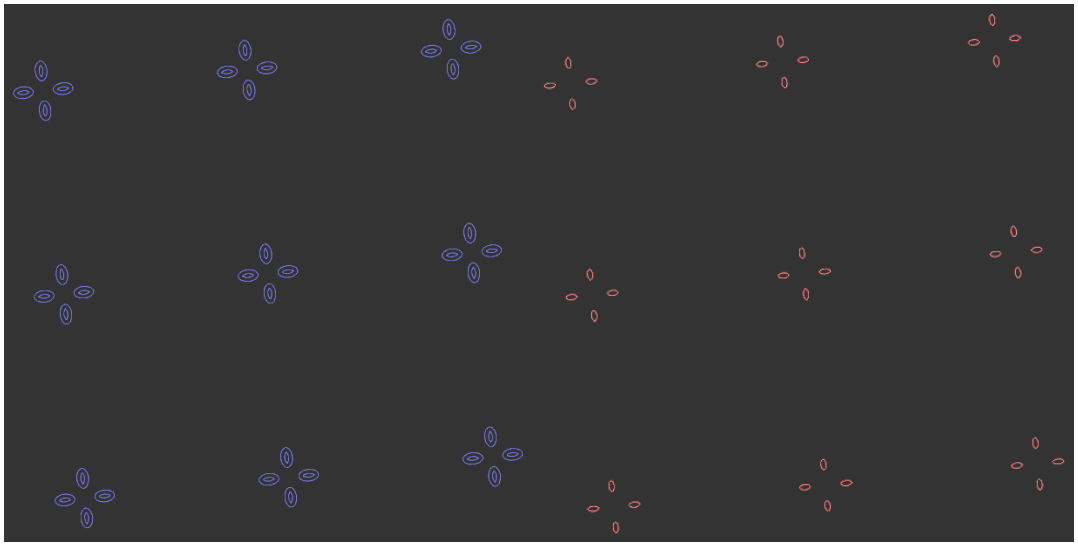

*Figure 6-1. Laser scan patterns for: Specimen 1 (left) and Specimen 2 (right), lattice structures designs.*

Figure 6-1 demonstrates that controlling the scanning strategy is crucial for achieving geometrically accurate lattice structures, particularly for beam diameter around 300 µm. While a concentric scanning path might be required for structures with larger beam diameters, its addition may not be necessary for diameters up to 500 µm, as indicated by the results from Specimen B. It is important to note that this recommendation is valid only for parameters that maintain the same approximate weld pool size and should be review if it changes. Consequently, tailoring the scanning strategy and using the appropriate offset value are as essential as selecting an optimal VED value.

### *6.2. LATTICE STRUCTURE THEORETICAL MODEL*

Based on the results presented in Section 5.3, there is a notable discrepancy between the experimental values of elastic modulus (Young's modulus, $E$) and yield strength ($\sigma_y$) and the theoretical values predicted by the Gibson-Ashby model.

Several factors may contribute to this discrepancy. Firstly, despite calculating the actual relative density using Avizo software and CT images, there is inherent error. Although this error might influence the results, it is unlikely to account for the magnitude of the observed difference. Additionally, the calculation of the actual relative density did not consider internal beam porosity, which could also affect the prediction, though not to the extent observed. When internal porosity is considered, the expected elastic modulus is 4.91GPa compared to 5.14GPa. This difference is minor and still the value is significantly higher than the experimental mean value of 1.32 GPa.

It would be beneficial to calculate the real relative density using the real beam diameter and the actual distance between unit cells. Ensuring the accuracy of the relative density is crucial, as it is the foundational parameter for the model. Although the expected distance between cells is 1 mm, the observed increase in beam diameter (approximately by 150µm) impacted this value as shown in Figure 5-21. The relative density derived from the CT images should account for these variations. Nonetheless, the veracity of the relative density calculated from CT images can be assessed using the equation for BCC structures provided by Zhong et al. [48], which accurately predicts the relative density based on the geometry of the lattice with the only requirement of $\frac{l}{d} > 5$. The used equation is shown below,

$$\rho_{rel} = \frac{3\sqrt{3}\pi}{4}\left(\frac{d}{l}\right)^2 \quad (10)$$

Here, $d$ represents the beam diameter and $l$ signifies the length of the beams, which in this scenario is twice the distance between unit cells. The resulting relative densities are shown in Table 6-2, allowing for a comparison with the relative density calculated with the CT images.

*Table 6-2. Summary of the mean values of the structure's geometry (Section 5.2) and calculated relative densities. The analytical relative density is calculated based on equation (10) and the adjusted values consider the internal porosity of the beam.*

| | **Specimen 1** | **Specimen 2** |
|---|---|---|
| *Real Beam Diameter [μm]* | 452.50 | 294.60 |
| *Real Distance between cells [μm]* | 860.08 | 932.51 |
| *Internal Porosity [%]* | 2.25 | 1.43 |
| *CT image-Relative density [%]* | 27.10 | 16.20 |
| *Adjusted CT image-Relative density [%]* | 26.49 | 15.97 |
| *Analytical-Relative density [%]* | 28.24 | 10.18 |
| *Adjusted Analytical-Relative density [%]* | 27.61 | 10.04 |

Based on the results shown in the table above, it is clear that there is a difference between the analytical values of the relative density and those obtained from the CT images. The difference is particularly significant in Specimen 2, where it is approximately 6% higher. The discrepancy can significantly affect the predicted mechanical properties of the structures, though it does not entirely account for the observed deviations. Additionally, while equation (10) has been shown to accurately calculate relative density, it relies on two different measurements, making it more susceptible to measurement error. Also, even if the designed lattice structures comply with the $\frac{l}{d} > 5$ requirement, the final dimensions of Specimen 1 do not. This implies that equation (10) is not applicable for Specimen 1. Therefore, the adjusted CT image relative density will be used forward as the true value.

Moreover, it is plausible that an error originates from the model itself. Significant discrepancies have been observed in bending-dominated titanium alloy lattice structures in prior research [48], [64]. Based on the relationship of Gibson-Ashby model, the scaling pre-factor for the elastic modulus (Equation (7)) includes all of the geometric constraints of proportionality and its value may vary depending on the cell shape [70]. It was shown that for a ceramic foam with a porous strut the most fitted value for $C_1$ was 0.3 [70]. Given that there exists internal porosity within the specimen's struts, it is interesting to compare the accuracy of the model when this scaling pre-factor is used. Also, for the yield stress equation an adjusted version exists that takes into account a density correction made to subtract the cell corners from the length of the beam which is necessary for higher densities [70]. The adjusted equation is shown below,

$$\frac{\sigma_{y,latt}}{\sigma_{y,s}} = C_2(\rho_{rel})^m \left(1 + (\rho_{rel})^{1/2}\right)$$

*(11)*

Therefore, it is of interest to observe the Gibson-Ashby model behavior for the recommended values of the scaling pre-factors as well as for the adjusted values, meaning using a value of 0.3 for $C_1$ to predict the elastic modulus and to use Equation (11) for the yield stress. Figure 6-2 and Figure 6-3 compare the Gibson-Ashby model with the adjusted version and the experimental data for the elastic modulus and the yield strength respectively. Specimen 1 data is related to the bigger relative density while Specimen 2 is related to the lower relative density.

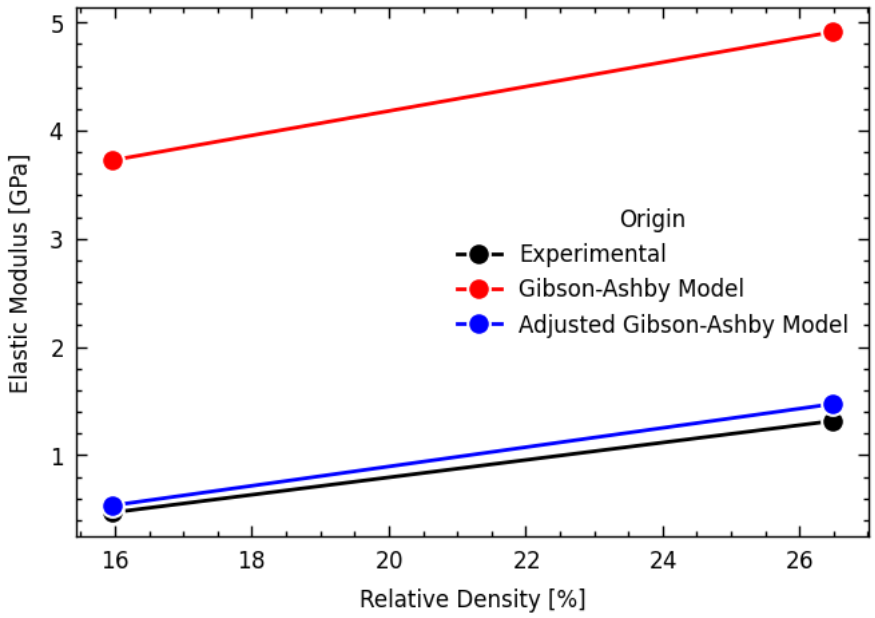


*Figure 6-2. Analytical predictions of the elastic modulus of the lattice structure with the Gibson-Ashby model and the experimental results from the compression test performed. The adjusted Gibson-Ashby model has a $C_1$ value of 0.3.*

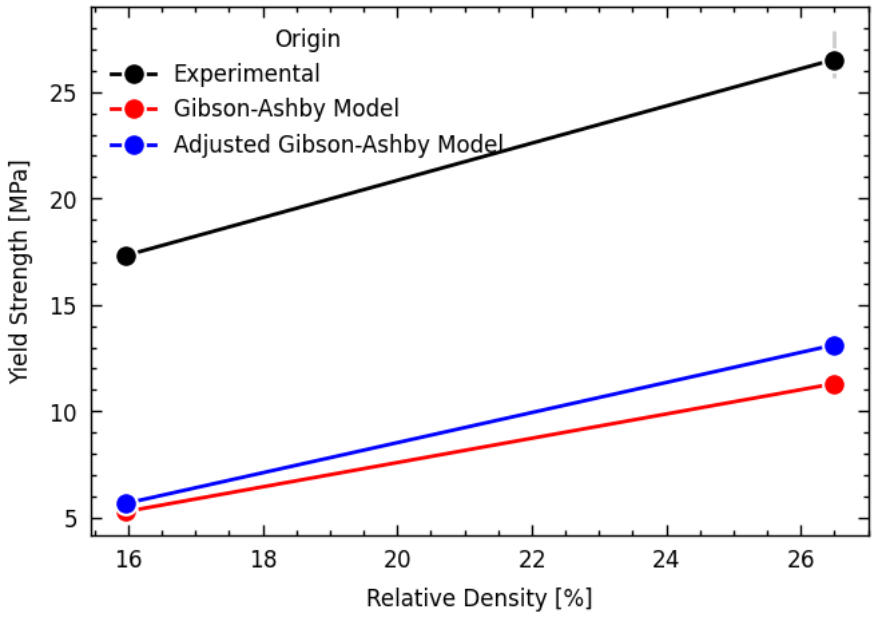


*Figure 6-3. Analytical predictions of the yield strength of the lattice structure with the Gibson-Ashby model and the experimental results from the compression test performed. The adjusted Gibson-Ashby uses Equation (11).*

Figure 6-2 and Figure 6-3 suggest that the recommended values for $C_1$ and $C_2$ are not suitable for the additive manufactured lattice structures. However, adjusting these values yielded a better fit, as illustrated in Figure 6-2. Additionally, the Gibson-Ashby model's prediction for yield stress shows a visible improvement when using Equation (11) but it is still far from the experimental values. To achieve a more accurate prediction of yield strength, further adjustment of $C_2$ is necessary.

To accurately determine the values of $C_1$ and $C_2$ for predicting the behavior of the additively manufactured BCC lattice structures using the specified aluminum alloy, more data is required for various relative densities. It is important to note, however, that the accuracy of the Gibson-Ashby model decreases for relative densities above 0.3 [67].

### *6.3. COMPRESSION TEST PERFORMANCE*

The compression tests yielded experimentally determined values for key material properties of the lattice structure. The mean values of these parameters are:

- Elastic modulus (Young's Modulus, $E$): $1.38 GPa$,
- Yield strength ($\sigma_y$): $25.68$ MPa,
- Ultimate Strength ($\sigma_{ult}$): $37.95$ MPa

There is a noticeable deviation in these parameters when a step compression test, similar to the one conducted for DVC analysis, is performed. The mechanical properties determined via the step compression test are lower. This discrepancy may be attributed to the incremental nature of the test, which could cause the lattice structure to repeatedly unload stress, altering its hardening behavior and affecting the mechanical properties. Alternatively, internal lattice structure defects could account for this difference. However, given the consistent porosity results for Specimen 1 in Section 5.2, this is unlikely.

The DVC analysis revealed that the failure in the structure is initiated by stress concentration due to a local defect, leading to the formation of a diagonal shear band. This band and the localized strain result in bending of the structure, as observed in the volume renderings in Section 5.4. This failure mode has also been observed in titanium alloy BCC lattice structures [64], indicating a similar failure mode for Specimen 2 to be expected.

Moreover, the DVC analysis was instrumental in identifying the local defect that originated the structure's failure. In this case, a defect near the intersection of the beams (node) triggered the failure. Given the high porosity throughout Specimen 1, the failure zone could have originated from any defect. However, because this defect was closer to the beam's surface and near the already critical zone of the beam intersection, it became the failure point. This highlights two main characteristics to control in the lattice structure: surface quality and defects around the nodes.

### *6.4. HEALING PROPERTIES WITH LATTICE STRUCTURES*

The preliminary HHT based on Gheysen et al. [2] protocols were initially unsuccessful. The results led to the hypothesis of an increased eutectic phase within the structure, which was confirmed through composition analysis of the manufactured parts. The higher concentration of magnesium causes a higher concentration of eutectic phase within the microstructure. A high concentration of eutectic phase has been known to cause structural problems, specifically at high temperature HHT (above 450°C) like the ones used for liquid-assisted healing. Therefore, this was confirmed to be the reason of the failed HHT at 540°C. Nevertheless, the ability of the lattice structures to be submitted to a liquid-assisted healing treatment wanted to be explored. Based on the work performed by Gheysen et al. [2] on a part with a concentration of 23.7% wt of Mg, a HHT was performed at 450°C for 30 minutes with air cooling that yielded similar results as those observed with the lattice structures and the HHT at 540°C (Figure 5-36). If 450°C yielded the same results as with 540°C, it would become apparent that this mechanism is not possible for the manufactured lattice structures due to their magnesium concentration, approximate 13% wt.

However, the results of the lattice structures submitted to the 450°C for 30 minutes with air cooling HHT show potential for possible tailoring of the HHT to get better healing results. Although the results do not show healing, they do present better behavior than with the 540°C HHT. Concluding that liquid-assisted healing might be possible but additional tailoring of the HHT is needed.

Future tailoring efforts should consider the overall size of the structure. Given the small diameter of the beams (approximately 300 µm) and the specific geometry of lattice structures that allow for air to envelop the struts entirely, careful consideration is necessary when calculating the appropriate treatment time for both diffusion-based and liquid-assisted healing. The goal is to avoid exceeding the optimal amount of time and cause porosity growth due to evaporation of alloying materials. Gheysen et al. temperature and diffusion healing time relationships that may prove useful [2]. Although the radius of the eutectic cells within the microstructure of the lattice structures must be measured prior to accurately estimate diffusion time towards the cell center.

Regarding the growth observed on the HHT samples, hydrogen blistering could be occurring within the structure, as this phenomenon has been observed during heat treatments of aluminum alloys manufactured by LPBF [2]. This phenomenon could explain the increase in smaller-sized porosities. However, it was expected that the presence of Mg in solid solution would enhance hydrogen solubility in the aluminum matrix. If hydrogen blistering is confirmed, the assumption would be invalid for the manufactured geometries.

Additionally, based on the composition analysis results in Table 4-1, Sn contamination may be causing porosities during the HHT. Given Sn low melting temperature, it is plausible that it evaporates during a 450°C HHT. Although, results in Table 5-1 for the structure heat treated at 540°C indicate no significant Sn evaporation, which warrants further investigation.

In contrast, diffusion-based healing was demonstrated to be feasible, as shown in Figure 5-38, where porosity tends to reduce its equivalent diameter. More tests are needed to confirm this trend across multiple samples. Nevertheless, addressing hydrogen blistering is a priority to ensure it does not pose a problem at diffusion-based temperatures.

Moreover, an interesting observation is the lack of significant magnesium evaporation during LPBF. This is the phenomenon that caused the previously defined HHT not to work for the manufactured lattice structures. Two hypotheses were proposed: the geometry of the lattice structures and the use of pre-alloyed powder. Due to the lattice structure geometry, the laser scan during printing is extremely fast, which was hypothesized to limit magnesium evaporation. This was partially confirmed, as the reduction in magnesium evaporation was less pronounced in solid parts compared to lattice structures. However, the use of pre-alloyed powder also appears to influence the amount of evaporated magnesium during manufacturing, which must be considered in future work.

## 7. CONCLUSIONS.

Lattice structures have small features that make them sensitive to the processing parameters. Throughout the research, it was essential to select parameters that guaranteed both geometric accuracy and the part density, a task that often requires balancing competing factors. Nevertheless, the tested parameters proved effective for processing aluminum alloy lattice structures. Specifically, using a linear energy density (LED) of 0.409 J/mm, along with pre-sintering and a contour-only scan path, yielded the best results for a lattice structure with a 300 µm beam diameter. The pre-sintering step, in particular, showed promising outcomes in terms of both geometric accuracy and surface roughness. Additionally, the selection of the correct scanning pattern was found to be crucial for manufacturing lattice structures. The scanning pattern significantly influenced dimensional accuracy and part density (internal porosity), highlighting its importance not only in heat management during printing but also for overall part quality.

Furthermore, the limitations of the Gibson-Ashby model in accurately predicting the behavior of additively manufactured lattice structures were observed. It was concluded that the recommended scaling pre-factors for bending-dominated structures do not yield accurate predictions. However, modifying these factors may improve accuracy for both elastic modulus and yield strength. Tailoring these values to specific material and lattice structure combinations may be necessary, although further research with a broader range of relative densities is needed to validate this approach.

Moreover, the effectiveness of Digital Volume Correlation (DVC) analysis in identifying critical defects in the structures was demonstrated. The DVC analysis revealed how a defect near a node caused stress concentration and localized strain, leading to the formation of a diagonal shear band. These results can be valuable for predicting critical characteristics of manufactured lattice structures and improving their mechanical behavior. However, additional analyses on more parts are required to confirm these critical defects.

Finally, the healing properties of the material when applied to lattice structures were tested. It was concluded that while the diffusion healing mechanism was successful for one lattice

structure with a magnesium composition of 12.1% of wt. using a healing heat treatment (HHT) of 400°C for 30 min followed by air cooling, the liquid-assisted mechanism requires further investigation. Preliminary tests with an HHT at 450°C for 30 min followed by air cooling showed promising results. Although these results did not demonstrate healing, further investigation into the appearance of smaller sized porosities may lead to modification in the HHT that achieves the desire performance.

## 8. REFERENCES.

[1] N. Van Dijk and S. Van Der Zwaag, "Self-Healing Phenomena in Metals," *Adv. Mater. Interfaces*, vol. 5, no. 17, p. 1800226, Sep. 2018, doi: 10.1002/admi.201800226.

[2] J. Gheysen *et al.*, "Design, development and characterisation of new healable aluminium alloys for laser powder bed fusion. Thèse présentée le 12/10/2022 en vue de l'obtention du grade de Docteur en Sciences de l'Ingénieur."

[3] A. Schmets, G. Zaken, and S. Zwaag, *Self Healing Materials: An Alternative Approach to 20 Centuries of Materials Science*. 2007.

[4] B. Grabowski and C. C. Tasan, "Self-Healing Metals," in *Self-healing Materials*, M. D. Hager, S. van der Zwaag, and U. S. Schubert, Eds., Cham: Springer International Publishing, 2016, pp. 387–407. doi: 10.1007/12_2015_337.

[5] M. D. Hager, P. Greil, C. Leyens, S. van der Zwaag, and U. S. Schubert, "Self-healing materials.," *Adv. Mater. Deerfield Beach Fla*, vol. 22, no. 47, pp. 5424–5430, Dec. 2010, doi: 10.1002/adma.201003036.

[6] S. Ghosh, "Self-Healing Materials: Fundamentals, Design Strategies, and Applications," in *Self-Healing Materials: Fundamentals, Design Strategies, and Applications*, 2009, pp. 1–28. doi: 10.1002/9783527625376.ch1.

[7] J. Martinez Lucci, R. S. Amano, P. Rohatgi, and B. Schultz, "Experiment and Computational Analysis of Self-Healing in an Aluminum Alloy," in *IMECE2008*, Volume 10: Heat Transfer, Fluid Flows, and Thermal Systems, Parts A, B, and C, Oct. 2008, pp. 1759–1768. doi: 10.1115/IMECE2008-68304.

[8] J. Lucci, R. Amano, and P. Rohatgi, "Heat transfer and fluid flow analysis of self-healing in metallic materials," *Heat Mass Transf.*, vol. 53, Mar. 2017, doi: 10.1007/s00231-016-1837-y.

[9] V. Kilicli, X. Yan, N. Salowitz, and P. Rohatgi, "Recent Advancements in Self-Healing Metallic Materials and Self-Healing Metal Matrix Composites," *JOM*, vol. 70, pp. 1–9, Apr. 2018, doi: 10.1007/s11837-018-2835-y.

[10] M. Nosonovsky and P. K. Rohatgi, "Development of Metallic and Metal Matrix Composite Self-Healing Materials," in *Biomimetics in Materials Science: Self-Healing, Self-Lubricating, and Self-Cleaning Materials*, M. Nosonovsky and P. K. Rohatgi, Eds., New York, NY: Springer, 2012, pp. 87–122. doi: 10.1007/978-1-4614-0926-7_5.

[11] S. Zhang, N. van Dijk, and S. Zwaag, "A Review of Self-healing Metals: Fundamentals, Design Principles and Performance," *Acta Metall. Sin. Engl. Lett.*, vol. 33, Jul. 2020, doi: 10.1007/s40195-020-01102-3.

[12] X. G. Zheng, Y.-N. Shi, and K. Lu, "Electro-healing cracks in nickel," *Mater. Sci. Eng. A*, vol. 561, pp. 52–59, Jan. 2013, doi: 10.1016/j.msea.2012.10.080.

[13] A. Kumar and S. K. Paul, "Healing of fatigue crack in steel with the application of pulsed electric current," *Materialia*, vol. 14, p. 100906, Dec. 2020, doi: 10.1016/j.mtla.2020.100906.

[14] H. Song, Z.-J. Wang, X.-D. He, and J. Duan, "Self-healing of damage inside metals triggered by electropulsing stimuli," *Sci. Rep.*, vol. 7, no. 1, p. 7097, Aug. 2017, doi: 10.1038/s41598-017-06635-9.

[15] M. Song, K. Du, S. P. Wen, Z. R. Nie, and H. Q. Ye, "In situ electron microscopy investigation of void healing in an Al–Mg–Er alloy at a low temperature," *Acta Mater.*, vol. 69, pp. 236–245, May 2014, doi: 10.1016/j.actamat.2014.02.004.

[16] H. Wang, P. Huang, and Z. Li, "Crack and Void Healing in Metals," in *Self Healing Materials: An Alternative Approach to 20 Centuries of Materials Science*, vol. 100, 2007, pp. 255–277. doi: 10.1007/978-1-4020-6250-6_12.

[17] H. L. Zhang and J. Sun, “Diffusive healing of intergranular fatigue microcracks in iron during annealing,” *Mater. Sci. Eng. A*, vol. 382, no. 1, pp. 171–180, Sep. 2004, doi: 10.1016/j.msea.2004.04.069.
[18] R. Lumley and I. Polmear, “ADVANCES IN SELF HEALING OF METALS,” 2007. Accessed: Apr. 29, 2024. [Online]. Available: https://www.semanticscholar.org/paper/ADVANCES-IN-SELF-HEALING-OF-METALS-Lumley-Polmear/83258e0705bb40761e5f44ada653a5f54bfc8a77
[19] D. Wei, J. Han, Z. Y. Jiang, C. Lu, and A. K. Tieu, “A study on crack healing in 1045 steel,” *J. Mater. Process. Technol.*, vol. 177, no. 1, pp. 233–237, Jul. 2006, doi: 10.1016/j.jmatprotec.2006.04.067.
[20] M. Arseenko *et al.*, “A new healing strategy for metals: Programmed damage and repair,” *Acta Mater.*, vol. 238, p. 118241, Oct. 2022, doi: 10.1016/j.actamat.2022.118241.
[21] ISO and ASTM, “ISO/ASTM 52900 Additive manufacturing — General principles — Terminology.” Accessed: Apr. 11, 2024. [Online]. Available: https://www.iso.org/obp/ui/#iso:std:iso-astm:52900:dis:ed-2:v1:en
[22] T. DebRoy *et al.*, “Additive manufacturing of metallic components – Process, structure and properties,” *Prog. Mater. Sci.*, vol. 92, pp. 112–224, Mar. 2018, doi: 10.1016/j.pmatsci.2017.10.001.
[23] ASTM, “ASTM F2792-12, Standard Terminology for Additive Manufacturing Technologies.” Accessed: Apr. 11, 2024. [Online]. Available: https://www.astm.org/f2792-12.html
[24] R. Singh *et al.*, “Powder bed fusion process in additive manufacturing: An overview,” *Mater. Today Proc.*, vol. 26, pp. 3058–3070, 2020, doi: 10.1016/j.matpr.2020.02.635.
[25] Jordan Weaver, Alec Schlenoff, David Deisenroth, and Shawn P. Moylan, “Inert Gas Flow Speed Measurements in Laser Powder Bed Fusion Additive Manufacturing,” Oct. 2021, doi: 10.6028/NIST.AMS.100-43.
[26] M. Qian, “Metal Powder for Additive Manufacturing,” *JOM*, vol. 67, no. 3, pp. 536–537, Mar. 2015, doi: 10.1007/s11837-015-1321-z.
[27] A. T. Sutton, C. S. Kriewall, M.-C. Leu, and J. W. Newkirk, “Powders for Additive Manufacturing Processes: Characterization Techniques and Effects on Part Properties”.
[28] K. Abd-Elghany and D. L. Bourell, “Property evaluation of 304L stainless steel fabricated by selective laser melting,” *Rapid Prototyp. J.*, vol. 18, no. 5, pp. 420–428, Jul. 2012, doi: 10.1108/13552541211250418.
[29] J. P. Oliveira, A. D. LaLonde, and J. Ma, “Processing parameters in laser powder bed fusion metal additive manufacturing,” *Mater. Des.*, vol. 193, p. 108762, Aug. 2020, doi: 10.1016/j.matdes.2020.108762.
[30] R. Snell *et al.*, “Methods for Rapid Pore Classification in Metal Additive Manufacturing,” *JOM*, vol. 72, no. 1, pp. 101–109, Jan. 2020, doi: 10.1007/s11837-019-03761-9.
[31] H. E. Sabzi, S. Maeng, X. Liang, M. Simonelli, N. T. Aboulkhair, and P. E. J. Rivera-Díaz-del-Castillo, “Controlling crack formation and porosity in laser powder bed fusion: Alloy design and process optimisation,” *Addit. Manuf.*, vol. 34, p. 101360, Aug. 2020, doi: 10.1016/j.addma.2020.101360.
[32] W. E. King *et al.*, “Observation of keyhole-mode laser melting in laser powder-bed fusion additive manufacturing,” *J. Mater. Process. Technol.*, vol. 214, no. 12, pp. 2915–2925, Dec. 2014, doi: 10.1016/j.jmatprotec.2014.06.005.
[33] D. Bhate, “Four Questions in Cellular Material Design,” *Materials*, vol. 12, p. 1060, Mar. 2019, doi: 10.3390/ma12071060.
[34] W. Tao and M. C. Leu, “Design of lattice structure for additive manufacturing,” in *2016 International Symposium on Flexible Automation (ISFA)*, Aug. 2016, pp. 325–332. doi: 10.1109/ISFA.2016.7790182.

[35] L. J. Gibson and M. F. Ashby, *Cellular Solids: Structure and Properties*, 2nd ed. in Cambridge Solid State Science Series. Cambridge: Cambridge University Press, 1997. doi: 10.1017/CBO9781139878326.

[36] C. Pan, Y. Han, and J. Lu, "Design and Optimization of Lattice Structures: A Review," *Appl. Sci.*, vol. 10, p. 6374, Sep. 2020, doi: 10.3390/app10186374.

[37] G. Dong, Y. Tang, and Y. F. Zhao, "A Survey of Modeling of Lattice Structures Fabricated by Additive Manufacturing," *J. Mech. Des.*, vol. 139, no. 100906, Aug. 2017, doi: 10.1115/1.4037305.

[38] R. Mahshid, H. N. Hansen, and K. L. Højbjerre, "Strength analysis and modeling of cellular lattice structures manufactured using selective laser melting for tooling applications," *Mater. Des.*, vol. 104, pp. 276–283, Aug. 2016, doi: 10.1016/j.matdes.2016.05.020.

[39] D. S. J. Al-Saedi, S. H. Masood, M. Faizan-Ur-Rab, A. Alomarah, and P. Ponnusamy, "Mechanical properties and energy absorption capability of functionally graded F2BCC lattice fabricated by SLM," *Mater. Des.*, vol. 144, pp. 32–44, Apr. 2018, doi: 10.1016/j.matdes.2018.01.059.

[40] S. Yin, L. Wu, J.-S. Yang, L. Ma, and S. Nutt, "Damping and low-velocity impact behavior of filled composite pyramidal lattice structures," *J. Compos. Mater.*, vol. 48, Jun. 2013, doi: 10.1177/0021998313490582.

[41] H. N. G. Wadley and D. Queheillalt, "Thermal Applications of Cellular Lattice Structures," *Mater. Sci. Forum - MATER SCI FORUM*, vol. 539–543, pp. 242–247, Mar. 2007, doi: 10.4028/www.scientific.net/MSF.539-543.242.

[42] L.-Y. Chen, S.-X. Liang, Y. Liu, and L.-C. Zhang, "Additive manufacturing of metallic lattice structures: Unconstrained design, accurate fabrication, fascinated performances, and challenges," *Mater. Sci. Eng. R Rep.*, vol. 146, p. 100648, Oct. 2021, doi: 10.1016/j.mser.2021.100648.

[43] X. Z. Zhang, M. Leary, H. P. Tang, T. Song, and M. Qian, "Selective electron beam manufactured Ti-6Al-4V lattice structures for orthopedic implant applications: Current status and outstanding challenges," *Curr. Opin. Solid State Mater. Sci.*, vol. 22, no. 3, pp. 75–99, Jun. 2018, doi: 10.1016/j.cossms.2018.05.002.

[44] W. P. Syam, W. Jianwei, B. Zhao, I. Maskery, W. Elmadih, and R. Leach, "Design and analysis of strut-based lattice structures for vibration isolation," *Precis. Eng.*, vol. 52, pp. 494–506, Apr. 2018, doi: 10.1016/j.precisioneng.2017.09.010.

[45] V. S. Deshpande, N. A. Fleck, and M. F. Ashby, "Effective properties of the octet-truss lattice material," *J. Mech. Phys. Solids*, vol. 49, no. 8, pp. 1747–1769, Aug. 2001, doi: 10.1016/S0022-5096(01)00010-2.

[46] D. J. Yoo, "Porous scaffold design using the distance field and triply periodic minimal surface models," *Biomaterials*, vol. 32, no. 31, pp. 7741–7754, Nov. 2011, doi: 10.1016/j.biomaterials.2011.07.019.

[47] S. C. Han, J. W. Lee, and K. Kang, "A New Type of Low Density Material: Shellular," *Adv. Mater.*, vol. 27, no. 37, pp. 5506–5511, 2015, doi: 10.1002/adma.201501546.

[48] H. Zhong, T. Song, C. Li, R. Das, J. Gu, and M. Qian, "The Gibson-Ashby model for additively manufactured metal lattice materials: Its theoretical basis, limitations and new insights from remedies," *Curr. Opin. Solid State Mater. Sci.*, vol. 27, no. 3, p. 101081, Jun. 2023, doi: 10.1016/j.cossms.2023.101081.

[49] P. Jacobs, E. Sevens, and M. Kunnen, "Principles of computerised X-ray tomography and applications to building materials," *Sci. Total Environ.*, vol. 167, no. 1–3, pp. 161–170, May 1995, doi: 10.1016/0048-9697(95)04577-N.

[50] Inc. Werth, "COMPUTER TOMOGRAPHY – PRINCIPLE OF X-RAY TOMOGRAPHY," Werth Knowing. Accessed: Apr. 10, 2024. [Online]. Available: https://werthinc.com/computer-tomography-principle-x-ray-tomography/

[51] J. J. Lifton *et al.*, "The application of voxel size correction in X-ray computed tomography for dimensional metrology".
[52] WenjuanSun, S. Brown, and R. Leach, *An overview of industrial X-ray computed tomography*. 2011.
[53] Seamark Zm, "X-ray Detection Equipment: Should You Choose Open Tubes or Closed Tubes?," Seamark Zm Technology Co. Accessed: Apr. 11, 2024. [Online]. Available: https://www.seamarkzm.com/xray-detection-equipment-should-you-choose-open-tubes-or-closed-tubes
[54] Wellman, "What is the difference between closed and open microfocus X-ray tubes?," Wellman X-Ray solutions. Accessed: Apr. 11, 2024. [Online]. Available: https://wmxray.com/what-is-the-difference-between-closed-and-open-microfocus-x-ray-tubes/
[55] L. A. Feldkamp, L. C. Davis, and J. W. Kress, "Practical cone-beam algorithm," *J. Opt. Soc. Am. A*, vol. 1, no. 6, p. 612, Jun. 1984, doi: 10.1364/JOSAA.1.000612.
[56] ThermoFisher, "Materials characterization and quality control software for imaging data analysis and quality assurance," ThermoFisher Scientific. [Online]. Available: https://www.thermofisher.com/be/en/home/electron-microscopy/products/software-em-3d-vis/avizo-software.html
[57] M. L. Hoag and R. L. Krahmer, "Polychromatic X-Ray Attenuation Characteristics and Wood Densitometry Applications." Jun. 28, 2007.
[58] B. Bay, "Methods and applications of digital volume correlation," *J. Strain Anal. Eng. Des. - J STRAIN ANAL ENG Des.*, vol. 43, pp. 745–760, Aug. 2008, doi: 10.1243/03093247JSA436.
[59] A. Buljac *et al.*, "Digital Volume Correlation: Review of Progress and Challenges," *Exp. Mech.*, vol. 58, no. 5, pp. 661–708, Jun. 2018, doi: 10.1007/s11340-018-0390-7.
[60] A. Guvenilir, T. M. Breunig, J. H. Kinney, and S. R. Stock, "Direct observation of crack opening as a function of applied load in the interior of a notched tensile sample of Al-Li 2090," *Acta Mater.*, vol. 45, no. 5, pp. 1977–1987, May 1997, doi: 10.1016/S1359-6454(96)00311-4.
[61] B. K. Bay, T. S. Smith, D. P. Fyhrie, and M. Saad, "Digital volume correlation: Three-dimensional strain mapping using X-ray tomography," *Exp. Mech.*, vol. 39, no. 3, pp. 217–226, Sep. 1999, doi: 10.1007/BF02323555.
[62] M.-L. Zhu, Q.-H. Zhang, C. Lupton, and J. Tong, "Spatial resolution and measurement uncertainty of strains in bone and bone–cement interface using digital volume correlation," *J. Mech. Behav. Biomed. Mater.*, vol. 57, pp. 269–279, Apr. 2016, doi: 10.1016/j.jmbbm.2015.12.017.
[63] F. Xu, "Quantitative characterization of deformation and damage process by digital volume correlation: A review," *Theor. Appl. Mech. Lett.*, vol. 8, no. 2, pp. 83–96, Mar. 2018, doi: 10.1016/j.taml.2018.02.004.
[64] M. Salingros, "Mechanical and MicroCT-based morphological characterization of 3D printed TI6AL4V lattice structures," Université Catholique de Louvain, 2019.
[65] M. F. Ashby, T. Evans, N. A. Fleck, J. W. Hutchinson, H. N. G. Wadley, and L. J. Gibson, *Metal Foams: A Design Guide*. Elsevier, 2000.
[66] I. Maskery *et al.*, "A mechanical property evaluation of graded density Al-Si10-Mg lattice structures manufactured by selective laser melting," *Mater. Sci. Eng. A*, vol. 670, pp. 264–274, Jul. 2016, doi: 10.1016/j.msea.2016.06.013.
[67] M. F. Ashby, "Chapter 11 - Designing Hybrid Materials," in *Materials Selection in Mechanical Design (Fourth Edition)*, M. F. Ashby, Ed., Oxford: Butterworth-Heinemann, 2011, pp. 299–340. doi: 10.1016/B978-1-85617-663-7.00011-4.
[68] A. Kamel, Z. Salem, R. Chemini, M. Khodja, and K. Allia, "Characterization of natural sand proppant used in hydraulic fracturing fluids," *Part. Sci. Technol.*, vol. 6, pp. 716–724, Apr. 2018, doi: 10.1080/02726351.2018.1438542.

[69] R. Mola and A. Dziadoń, “A R C H I V E S 24/4 Formation of magnesium-eutectic mixture layered composite,” *Arch. Foundry Eng.*, vol. 8, Dec. 2008.

[70] L. J. Gibson and M. F. Ashby, Eds., “The mechanics of foams: basic results,” in *Cellular Solids: Structure and Properties*, 2nd ed., in Cambridge Solid State Science Series. , Cambridge: Cambridge University Press, 1997, pp. 175–234. doi: 10.1017/CBO9781139878326.007.

**UNIVERSITÉ CATHOLIQUE DE LOUVAIN**
**École polytechnique de Louvain**
Rue Archimède, 1 bte L6.11.01, 1348 Louvain-la-Neuve, Belgique | **www.uclouvain.be/epl**